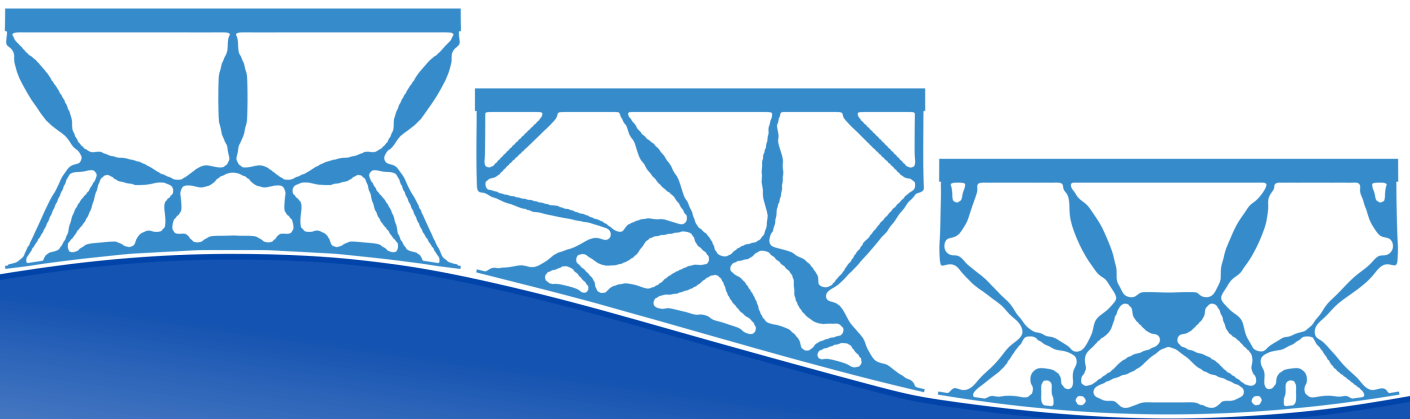


Department of Precision and Microsystems Engineering

Development of Deformable Hydrostatic Bearings with Topology Optimization

H.A. Schaab

Report no : 2023.088
Coach : Ir. D.D. Sonneveld
Professor : Dr. Ir. R.A.J. van Ostayen
Specialisation : Mechatronic System Design
Type of report : Master of Science Thesis
Date : November 14, 2023



ABSTRACT

Conventional hydrostatic bearings are not suited to use on surfaces with changing curvature which limits their applicability. To improve on this, deformable hydrostatic bearings are currently being researched. The goal of this work is to develop hydrostatic bearings with a single fluid supply that work for sinusoidal counter surfaces.

The bearing pad of a deformable hydrostatic bearing must be able to conform to the shape of the sinusoidal counter surface at any position while being able to carry high loads. Previous research has also pointed out that a deformable hydrostatic bearing should have a triangular contact pressure profile for compression against a flat surface. This way a bearing without preference towards either the concave or convex part on a sinusoidal counter surface should be obtained.

The design problem is translated into a problem formulation for the synthesis of compliant mechanisms with topology optimization. In this formulation strain energies of the design domain under different load cases are utilized to achieve selective stiffness. In an extension of the formulation, the reaction forces under uniform vertical compression of the structure are required to attain a triangular shaped profile. This requirement is relaxed in the second extension where the reaction forces are only required to monotonically decrease from the middle to the sides.

Optimizations without requirement on the reaction profile yield interesting structures with clear-cut boundaries. When implementing the requirement on the reaction profile, there appears to be a trade-off between achieving the prescribed shape and the presence of grey area and artifacts in the designs. The optimizer tends to employ distributed compliance to meet the requirement, which can compromise the load-bearing capabilities of the structures.

Evaluation of selected results with a contact model predicts that numerous obtained designs could function as a hydrostatic bearing on a sinusoidal counter surface with an amplitude of 11.3 mm. Additional effort with a more realistic evaluation model is required to draw a definite conclusion on the performance.

ACKNOWLEDGMENTS

I want to use the opportunity to thank my daily supervisor Dave for the big contribution he had in guiding me through the final part of my master. Dave, it has been a pleasure to work with you and I liked the discussions with you about my (and sometimes your) research topic. Thanks also for often taking a bit more time than planned for the meetings and always providing valuable feedback.

I also want to thank Stijn who introduced me to the topic of topology optimization and was always there when I needed help or advice on how to proceed further. Thanks should also be given to Ron for his valuable inputs during the full-film meetings as well as in the evaluation sessions. It encouraged me to get as much as possible out of my project.

Finally, I want to thank my parents who have always been a big help, supportive, and enabled me to finish my studies.

CONTENTS

1	Introduction	1
1.1	Hydrostatic Bearings	2
1.2	Developments in hydrostatic bearing design for sinusoidal counter surfaces	3
1.2.1	Whiffletree support structure	3
1.2.2	Pressure profile matching support	3
1.3	Scope of the thesis	4
1.3.1	Compliant Mechanisms	4
1.4	Research Objective	5
2	Background	6
2.1	Finite Element Method	6
2.2	Topology Optimization of Compliant Mechanisms	7
2.2.1	Density Method and SIMP	7
2.2.2	Problem Formulation	8
2.2.3	Checkerboarding	9
2.2.4	de facto hinges	9
2.2.5	Filtering	9
2.2.6	Solvers	10
3	Problem Analysis	11
3.1	Adaption to counter surface	11
3.2	Load Characteristics	11
3.3	Pad Length	12
3.4	Reaction force considerations	12
3.5	List of requirements	14
4	Topology Optimization Method	15
4.1	Strain energies as stiffness measure	16
4.2	General problem formulation	16
4.2.1	Simplifications of the problem	17
4.2.2	Load cases for objective	17

4.2.3	Load cases for constraints	18
4.3	Reaction force penalty/constraint	19
4.3.1	Pressure profile matching	20
4.3.2	Soft reaction constraint	20
4.4	Filtering and SIMP	21
4.5	Robust Formulation	22
4.6	Sensitivities	23
4.6.1	Sensitivities of strain energy terms	24
4.6.2	Sensitivities of performance measures for reaction force profile	24
4.7	Implementation	25
5	Topology Optimization Results	26
5.1	General parameters for optimizations	26
5.2	Investigation offset parameter	28
5.3	Choice of objective load case	29
5.4	Results without reaction profile requirement	30
5.4.1	Working principle of category 3 designs	32
5.5	Results with inclusion of reaction profile requirements	32
5.5.1	Pressure profile matching penalty	32
5.5.2	Modified approaches to improve satisfaction of the triangular reaction profile requirement	38
5.5.3	Soft reaction force constraint	41
5.6	Results with additional x-stiffness requirement	42
6	Evaluation of Designs	45
6.1	Development of the evaluation model	45
6.1.1	Post-processing of TO results	45
6.1.2	Material selection for evaluations	46
6.1.3	Contact model in COMSOL	46
6.1.4	Choice of parameters for evaluation model	47
6.2	Results of contact studies	50
6.2.1	Determining the maximum load	52
6.2.2	Determining the effective contact area	52
6.2.3	Usable load range for the evaluated designs	53
6.2.4	Reaction force plots	54

6.2.5	Contact area plots	55
6.2.6	Max gap plots	56
6.2.7	Discussion	56
6.3	Validation of reaction profiles used in the optimizations	59
6.3.1	Discussion	60
7	Conclusions and Recommendations	62
7.1	Conclusions	62
7.2	Recommendations	63
	Bibliography	64
A	Sensitivity analyses	66
A.1	Sensitivities of strain energy terms	66
A.1.1	pure applied forces	66
A.1.2	pure prescribed displacements	67
A.2	sensitivities of reaction forces	67
B	Additional info on optimizations	69
B.1	Typical iteration times	69
B.2	Convergence history	70
C	Additional information on the COMSOL models	71
C.1	Converting image files into a geometry	71
C.2	Creating separate boundaries for the boundary conditions	71
C.3	Mesh sizes in the evaluation models	72
D	Additional data from evaluations	73
D.1	Max α study	73
D.2	Deformed configurations from contact studies	74
D.3	Stiffness plots	81
D.4	Load at yield + load at 90 % contact	82

1 INTRODUCTION

Offshore wind farms play a significant role in the current transition towards renewable energies. Cost effectiveness increases with the use of larger wind turbines due to the fact that less turbines need to be manufactured and installed for the same amount of energy output [1]. Due to erosion by water droplets, there is a constraint on the maximum tip speed of the blades [2]. As a consequence, the rotational speed for larger turbines gets lower while there is an increase in torque that gets transferred to the generator. This is the exact opposite of the needs of conventional efficient generators (which need high rpm at low torque). Therefore, usually either a gearbox or direct-drive generator is implemented. Both solutions however have their own disadvantages:

1. gearboxes: consist of large amount of components, life-time under 20 years (for 37% it is even under 7 years) [3]
2. direct-drive generators: higher cost, are heavier and larger, higher need of permanent magnets (rare earth metals) [3]

The company Delft Offshore Turbine (further denoted by DOT) is developing a novel type of offshore wind turbine with the aim of providing energy conversion that requires less maintenance, thereby being more cost-effective. The idea is to use the rotary motion of the blades to drive a hydraulic pump sitting in the nacelle. In turn the high-pressure fluid streams (preferably seawater), coming from the pumps of several wind turbines are used to drive a Pelton wheel generator located at a central location (see Figure 1.1). DOT is currently developing the hydraulic pump.

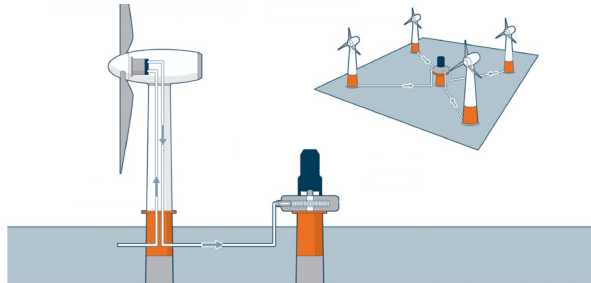


Figure 1.1: Illustration of the novel type of wind farm developed by DOT [4]

The radial piston pump design by DOT consists of multiple pistons mounted in circular fashion around the core of the pump (see Figure 1.2). At the end of each piston there is a cam roller which is pushed down onto the camring by the inlet pressure of the fluid that is being pumped. The shape of the camring with its repetitive pattern makes the pistons move into the center of the pump and back outwards again. For larger wind turbines, the need to compensate for lower rotational speeds leads to higher pressures. This in turn increases the load on the pistons and consequently on the cam rollers. To handle this extra load, we need larger cam rollers which increase the contact area. With size however, also the inertia of the rollers will go up and the constantly varying speed of the roller can lead to slip [5] which induces wear and results in a decreased lifetime of the pump. Replacing the roller with a hydrostatic bearing is one of the proposed solutions to the problem and would enable spread of the high loads over a larger area without mechanical contact. However, conventional hydrostatic bearings are rigid and therefore limited in their applicability on surfaces with changing curvature like the camring of the piston pump developed by DOT. Development of a hydrostatic bearing for this application could pave the way to much broader use of this technology.

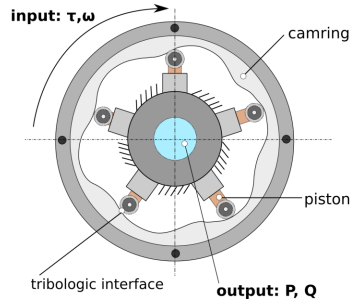


Figure 1.2: Illustration of the current design of the radial piston pump [6]

What follows is a short introduction to the working principle of hydrostatic bearings followed by recent developments in the area of hydrostatic bearings for sinusoidal counter surfaces. Thereafter the scope of the thesis and research objective are presented.

1.1. HYDROSTATIC BEARINGS

The cross section of a hydrostatic bearing is shown in Figure 1.3. High pressure fluid coming from the inlet in the middle lifts bearing pad up from the counter surface at the bottom. This enables motion of the bearing pad with low friction and minimal wear [7]. In conventional hydrostatic bearings the pad and counter surface are flat and stiff. As the fluid film height is typically in the order of $100\text{ }\mu\text{m}$, the flow can be assumed one-dimensional (meaning no pressure variation within the film height) and laminar [7]. The fluid pressure is equal to the ambient pressure at the sides of the bearing pad where it leaves the fluid film. For two perfectly flat surfaces with a symmetric load, the film height will be uniform and the bottom surface of the bearing pad thus parallel to the counter surface. This also means that the pressure drops linearly from the fluid inlet to the outlets as illustrated in Figure 1.3 since the resistance of fluid flow is constant for a uniform film. In case the supply pressure of the pump is fixed, the pressure distribution is independent of the film height. This means that for different film heights the load capacity will stay the same. In this case the bearing has no stiffness counteract changes in load at the top. To obtain stiffness, usually a restrictor between fluid pump and inlet is implemented. It induces a pressure drop from pump to fluid inlet. With the use of a restrictor an increase in load acting on the bearing will cause the pressure to increase at the fluid inlet. The bearing pad will now have stiffness up to the point where the pressure at the fluid inlet is equal to the supply pressure of the pump (where it will lose its stiffness).

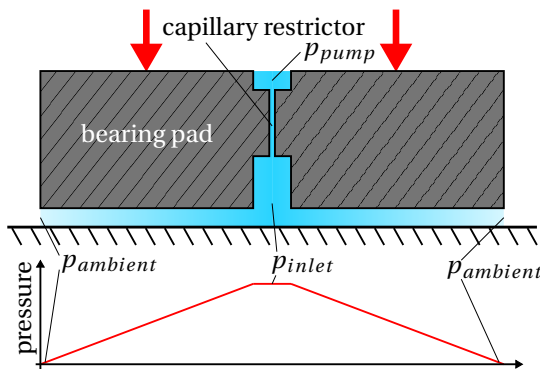


Figure 1.3: Illustration of a hydrostatic bearing

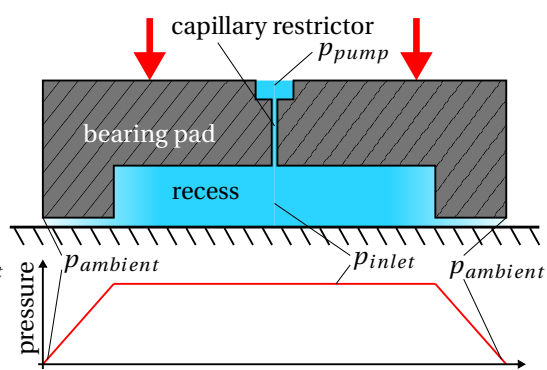


Figure 1.4: Illustration of a conventional hydrostatic bearing with recess

The integral of the fluid film pressure is equal to the load received by the bearing pad. To increase the load capacity for the same surface area conventional hydrostatic bearings have a recess in the bearing surface. For a large enough recess, the pressure drop within can be neglected meaning that the pressure in the recess can

be assumed to be equal to the inlet pressure [7]. As a consequence, the pressure drop over the outlet regions on the sides is steeper and the film thickness lower.

1.2. DEVELOPMENTS IN HYDROSTATIC BEARING DESIGN FOR SINUSOIDAL COUNTER SURFACES

As opposed to conventional hydrostatic bearings, the desired use case in the radial piston pump has a sinusoidal counter surface. The amplitude of this counter surface will be much larger than the film height which means that a rigid bearing can not be implemented conveniently. There are two ways to get to a hydrostatic bearing design with sufficient surface area while being able to follow the camring surface:

1. discretization of the bearing pad into multiple smaller ones with each one having their respective fluid supply
2. using a single deformable bearing pad which can conform to the counter surface for each position

In each of the presented cases an interface is needed to transfer the high load/(s) from the bearing pad/(s) to the piston while enabling the pad/(s) to follow the shape of the counter surface. For the first case the interface that has been explored is a whiffletree mechanism further described [subsection 1.2.1](#). In case of the single compliant bearing pad another type of interface with distributed compliance has been investigated as described in [subsection 1.2.2](#).

1.2.1. WHIFFLETREE SUPPORT STRUCTURE

First efforts to come up with a suitable mechanism are made in [8] where a whiffletree support structure, in form of a rigid body model, is proposed. The structure is shown in [Figure 1.5](#).

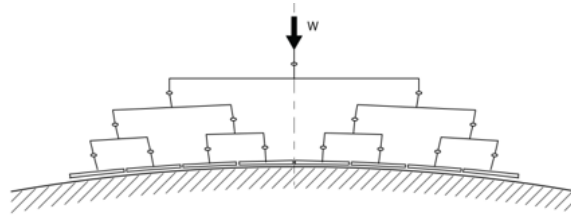


Figure 1.5: Whiffletree support structure [8]

The main idea behind the whiffletree design is that the rotations, which individual pads would have to perform in order to follow the camring surface, are spread out over the different levels of the structure. Another thing worth mentioning is that the required elevation of the individual pads with respect to each other is enabled by rotations of the higher levels in the support structure. Additionally, the balancing nature of the structure enables even spread of the load over different pads at the bottom.

One of the drawbacks of the current whiffletree design is that the top joint has to make the largest rotations in order to follow the overall shape of the camring [8]. This doesn't improve significantly with the use of more layers [8]. Additionally, the loads on the joints get larger the further we go up in terms of layers and the top joint has to support all of it.

1.2.2. PRESSURE PROFILE MATCHING SUPPORT

In [9] a single compliant bearing pad is made of elastic material. The strategy is to use a distributed material for the support which is designed such that its reaction pressure profile for a nominal compression has the same shape as the pressure profile generated by the fluid film. This results in a design of a bearing surface

where the Young's modulus (denoted with $E(x)$ in the figure) decreases linearly from the middle to the sides as shown in Figure 1.6. This kind of support has a uniform film height for a flat counter surface. However, the approach is only validated up to a surface waviness in the order of 1/100th the height of the support structure. Another issue with distributed material is that it is difficult to manufacture.

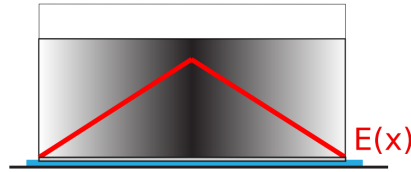


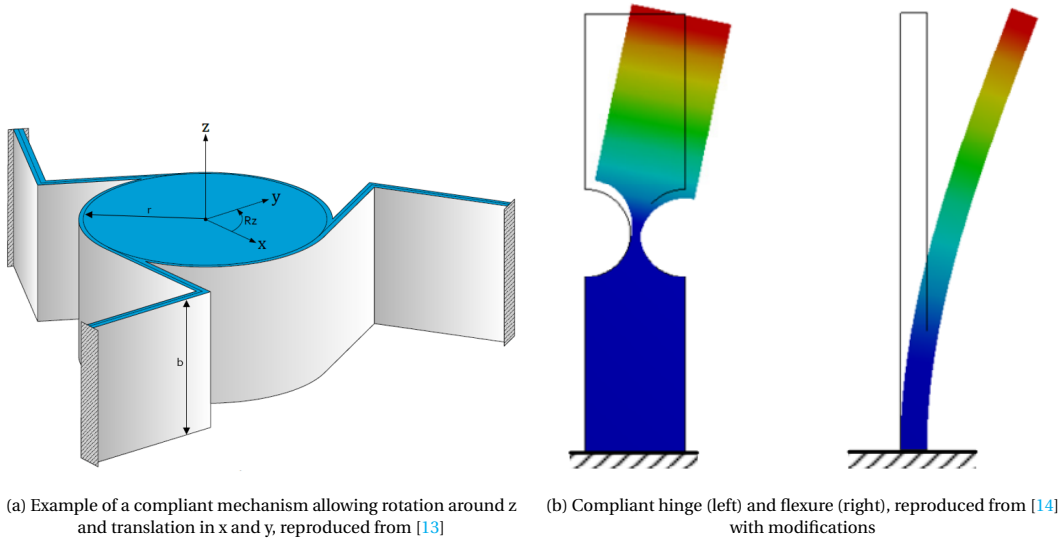
Figure 1.6: Compliant hydrostatic bearing developed in [8] (figure retrieved from the same source)

1.3. SCOPE OF THE THESIS

The current work focuses on the development of hydrostatic bearings with a single compliant bearing pad and one fluid supply. This is preferable over a multi-pad system in terms of manufacturability. The goal is to develop a bearing that can be used for larger amplitudes of the sinusoidal counter surface than previously done in subsection 1.2.2. It is sought to investigate the applicability of compliant mechanisms for this purpose. This subject has been touched upon previously by simulating a whiffletree mechanism with compliant joints [8] but we would like to explore if there are better alternatives. Before getting into more details on how this will be approached a brief introduction on the subject of compliant mechanisms is provided in the following section.

1.3.1. COMPLIANT MECHANISMS

In a compliant mechanism a set of input forces and movement is transformed into a desired set of output forces and displacements by elastic deformation of at least some of its members [10, 11]. Compliant mechanisms are typically implemented in high precision applications where backlash, present in conventional mechanisms, is an issue. Ideal conventional mechanisms consist of rigid-body linkages and zero-friction hinges. Those mechanisms can be quantified by their degrees of freedom, being the minimum number of independent variables describing the motion of the mechanism. Conventional mechanisms can be converted into compliant mechanisms by replacing the hinges with their compliant counterparts. A significant distinction between the original mechanism and its compliant version is the fact that a force is needed not only to transition the mechanism into a different configuration, but also in order to keep it there. If all applied forces are removed the compliant mechanism will return into the configuration with the lowest strain energy just like a spring. Compliance can be introduced locally, using compliant hinges, or in a distributed manner, such as with flexures (see Figure 1.7b). A great advantage of compliant mechanisms is that they require virtually no maintenance. This comes at the cost of limited range of motion, and load bearing capability. Another thing to look out for is the fact that compliant mechanisms can quickly lose stiffness in their intended stiff directions upon deformation [12].



1.4. RESEARCH OBJECTIVE

In this thesis it is sought to develop compliant mechanisms specifically for the purpose of a hydrostatic bearing with a single deformable pad which travels over a sinusoidal counter surface. A method that can be used to generate compliant mechanisms based on a mathematical description of the problem is topology optimization (further denoted as TO). This method has not yet been applied to similar problems and is well suited for design problems with contradicting requirements. Once set up correctly, it is expected to facilitate the generation of a broad range of solutions. Those will provide valuable insight into the design possibilities of deformable hydrostatic bearings. Thus, the research objective of the thesis is formulated as:

Use topology optimization to come up with novel compliant mechanism structures for use in a hydrostatic bearing traveling over a sinusoidal camring.

The approach for this work is not to develop a new methodology but to build on well-established TO methods. The research objective is further subdivided into the following sub-goals:

1. find a suitable TO method and formulation to be implemented for the purpose of the research goal
2. utilize the TO method to come up with structures which can be conveniently interpreted as compliant mechanisms
3. investigate how the parameters of the optimizations influence the performance of the designs

In [chapter 2](#) theoretical background for the subject of topology optimization of compliant mechanisms is given. [chapter 3](#) provides an analysis of the problem based of which the methodology to solve the problem with the selected TO routine is further developed in [chapter 4](#). Thereafter, the results of the optimizations with different parameter sweeps are presented and discussed in [chapter 5](#). A selection of designs obtained with the optimizations is evaluated in [chapter 5](#) by means of a model which more accurately represents the actual use case. In the same chapter part of the methodology is validated and discussed. The thesis is concluded in [chapter 7](#) where also recommendations for future research are given.

2 BACKGROUND

The current chapter starts with [section 2.1](#) where some background on the finite element method utilized in the optimization routine is provided. Out of the possible approaches for topology optimization of compliant mechanisms, the density method has been selected based on the literature study preceding the current report. This methodology is introduced in [section 2.2](#) and its aspects are discussed.

2.1. FINITE ELEMENT METHOD

Before getting into TO the underlying finite element method (finite element further denoted as FE) is briefly explained in this section. The method enables analysis of the deformation of structures under defined boundary conditions such as prescribed displacements and input forces like shown in [Figure 2.1](#). In the FE method, the structure to be analyzed is discretized into smaller elements (see [Figure 2.2](#)). A single element in 2D consists of three nodes at minimum, which are connected by line segments. In 2D each node has two degrees of freedom, usually being x- and y-displacement. To obtain the total number of degrees of freedom (denoted by n) the number of nodes has to be multiplied by the degrees of freedom per node (being two for the 2D case). The deformation field is only calculated for the nodes and can be interpolated to obtain deformations between the nodes. This enables description of the problem into the discrete system of equations:

$$\mathbf{f} = \mathbf{K}\mathbf{u} \quad (2.1)$$

where \mathbf{f} is the force vector of size n by 1, \mathbf{K} the stiffness matrix of size n by n , and \mathbf{u} is the displacement vector of size n by 1.

By solving this system an approximation of the displacement field of the structure under the applied boundary conditions is obtained. Note that in this work the linear FE method is used for the optimizations which means that the structures behave as if they were in linear elastic regime for small displacements.

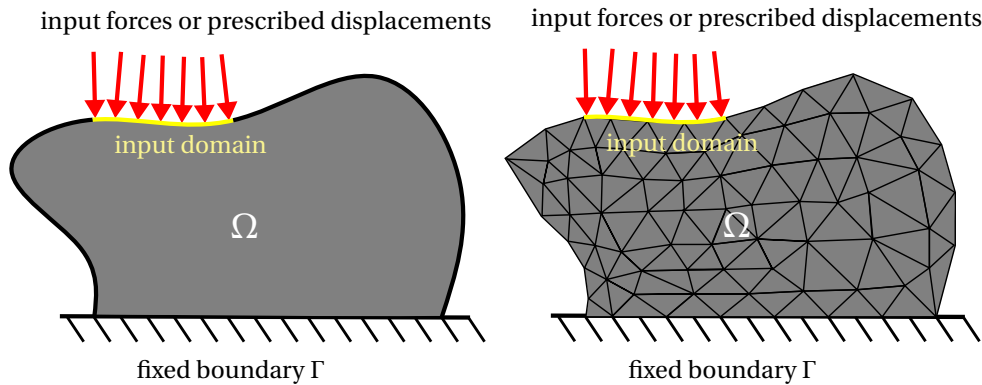


Figure 2.1: Illustration of a boundary value problem with 2D-structure Ω , an input domain where either forces or displacements are applied, and the boundary Γ where the displacements are prescribed to be zero

Figure 2.2: Illustration of the same problem with a design domain discretization using triangular elements

2.2. TOPOLOGY OPTIMIZATION OF COMPLIANT MECHANISMS

In topology optimization structures with an optimal number of holes as well as optimal shape are sought. In general, the optimization problem is mathematically formulated as follows:

$$\begin{aligned} \min_{\mathbf{x}} \quad & J(\mathbf{x}) \\ \text{s.t.} \quad & g(\mathbf{x}) \leq 0 \\ & h(\mathbf{x}) = 0 \end{aligned} \quad (2.2)$$

Here \mathbf{x} represents the design variables, $J(\mathbf{x})$ the objective function, $g(\mathbf{x})$ the inequality constraints and $h(\mathbf{x})$ the equality constraints. The area (in case of two-dimensional TO) or the volume (in case of three-dimensional TO) where material can be placed during the TO is called the design domain. This design domain is discretized into numerous smaller elements. A finer discretization of the design domain enables a more detailed representation of the optimal topology. Note that the design domain discretization does not necessarily have to correspond with the finite element discretization for the analysis (see [section 2.1](#)). It can however be convenient to do so regarding computational efficiency.

An illustration for the process of TO with the density method is provided in [Figure 2.3](#). To setup a TO problem the design domain, boundary conditions, input displacements, input forces, and the initial design variables have to be provided. The FE method is used to simulate the behavior of the current design under the given boundary and loading conditions. Based on the results the defined objective and constraint values can be calculated which form the base for the sensitivity analysis. The obtained sensitivities are used in the optimization algorithm which produces new values for the design variables which are supposed to be more optimal. This results in a new topology which is evaluated with a new finite element analysis from where the process repeats itself. The optimization is stopped if the solution has converged, or termination criteria are met. When implemented correctly the optimization results in a structure representing, at least, a local optimum for the topology of the defined problem.

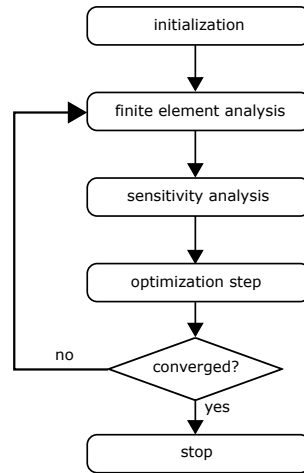


Figure 2.3: Flowchart reproduced from [15] with slight changes

2.2.1. DENSITY METHOD AND SIMP

In the density method, the densities of the individual elements are chosen as design variables. A density of zero represents void and a density of one represents material. As elements with zero density (and thus also a Young's modulus of zero) cause ill-conditioning for the system of equations to be solved in the FE analyses, usually a lower bound for the Young's modulus (denoted with E_{min}) is implemented. This means that void regions will have small but negligible stiffness when considering linear FE analyses. Due to the large amount of design variables needed to get results with sufficient resolution, TO problems are computationally expensive. In order to make it easier to solve these problems, the density of each element is allowed to attain continuous values between E_{min} and one. This enables the use of gradient-based algorithms which is the

only efficient way to solve TO problems according to [16]. In gradient-based methods the sensitivity of the objective function with respect to a small change in design variable is calculated for every element. Based on this information the optimizer can produce improved values for the design variables as stated before in the previous section.

The downside of continuous design variables is that results of the TO contain large areas with intermediate densities and thus no clear topology can be derived. In practice, we use penalization schemes to penalize the use of intermediate densities in the resulting design. The most popular of these schemes is called SIMP (simplified isotropic material with penalization) [17, 18]. Without the application of SIMP, the Young's modulus of each element is proportional to the density:

$$E_i = x_i E_{mat} \quad (2.3)$$

E_{mat} is the Young's modulus of the material. The modified SIMP approach, typically used nowadays, [19] works as follows:

$$E_i = E_{min} + x_i^p (E_{mat} - E_{min}) \quad (2.4)$$

The Young's modulus of the material (E_{mat}) minus the lower bound of the Young's modulus E_{min} is multiplied by the normalized density of the i -th element (x_i) to the power p . Adding E_{min} to the result leaves us with a material strength of E_{min} for void elements (where density equals zero) and the nominal Young's modulus E_{mat} for solid elements (where density equals one). For intermediate densities however, the strength to density ratio is lower as also illustrated in Figure 2.4. This makes it inefficient for the optimizer to use intermediate density elements. It is important to note that most often a volume constraint in some way (direct or indirect) is needed in order for the penalization to work because only then the strength to density ratio matters during optimization.

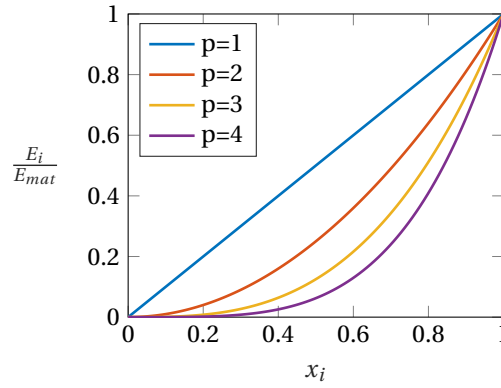


Figure 2.4: Relative Young's modulus of element i for all its attainable densities x_i

2.2.2. PROBLEM FORMULATION

TO is most widely used for the objective of stiffness maximization under a volume constraint to get the best performance of a structure in terms of stiffness/weight ratio. A volume constraint is needed because the addition of material will always increase the stiffness of the design. Without the volume constraint the design domain would get filled up with material completely. For compliant mechanisms however, defining an objective and constraints is not as straight forward anymore. A compliant mechanism needs high stiffness in one direction or load case as well as low stiffness for another load case. Formulation of an objective function for compliant mechanism synthesis is tightly related to the FE method which is used to evaluate the performance of the design during the optimization. There is no single go-to formulation for compliant mechanism design with TO. Usually the domain is subjected to an input displacement or force at the input domain and we optimize for the desired behavior (displacement or force) at the output domain (see Figure 2.5).

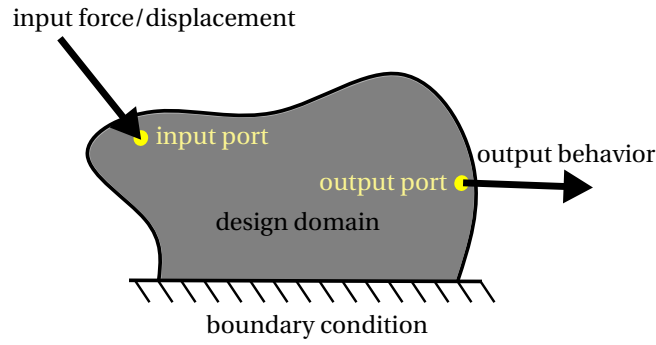


Figure 2.5: Problem setup

The reason for the existing variety in problem formulations comes from the fact that it is a challenge to get connected structures in the results. Another problem is to get accurate control over the stiffness of the compliant mechanism for its intended degrees of freedom. Zhu et al. in [20] and Cao et al. in [21] provide convenient overviews of previously proposed formulations.

2.2.3. CHECKERBOARDING

The tendency of optimized designs having regions with patterns as shown in Figure 2.6 is called checkerboarding. This is in fact not an artifact coming from the TO method but rather the finite element analysis overestimating the stiffness of diagonally connected elements [22]. The problem can be solved by using higher order elements (at cost of CPU time [23]) and under certain conditions for penalizing power p (see subsection 2.2.1). Other solutions are filtering or using a finite element mesh that is decoupled from the design mesh. Doing this a finite element mesh with several elements per ground element (the elements making up the design) can be used which circumvents the problem.

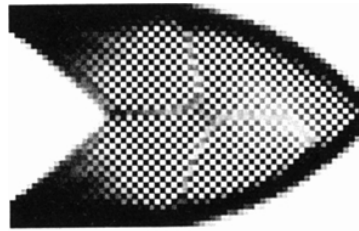


Figure 2.6: Checkerboarding in a result of TO, adapted from [23]

2.2.4. DE FACTO HINGES

Another issue in topology optimization of compliant mechanisms is called 'de facto hinges'. It refers to the optimizer placing only very little or no material at all in the regions of the compliant hinges. To make up 'de facto hinges' the optimizer is prone to diagonally connect two elements which makes a very effective hinge in the FE analysis but is not manufacturable in practice. This creates difficulties in the interpretation of the results.

2.2.5. FILTERING

In order to get rid of intermediate densities, checkerboarding, and to enable length scale control in the results of a TO using SIMP, filters have proven to be a viable solution. Length scale control is important because in TO we usually encounter mesh dependence. This means that finer features occur in the results of the TO for finer meshes that are being used. Usually, there is a constraint on minimum feature size when considering that the design has to be manufactured. To get enough detail in the solutions however, it can be required to

refine the mesh. In that case it is convenient to be able to set a limit on the feature size independently of the mesh size that is being used. There are three main types of filters which work on three different variables (fields) within the optimization procedure:

1. The first type are sensitivity filters which average out the sensitivity per element over the elements around it within a specified filter radius. It works on the sensitivity field as visualized in Figure 2.7.
2. Another option is to filter the densities by introducing a new field with the averaged density over the elements within a specified radius. There thus exists a design variable field containing the densities and the so-called physical field containing the filtered densities. The finite-element analysis is performed using the filtered field and gradient information obtained by using the chain rule.

Above mentioned filters still suffer from intermediate density elements at the boundaries of the design but are effective in obtaining length scale control.

3. In order to get rid of intermediate densities in boundary regions, the filtered field can be projected on a new field through a smoothed Heaviside projection which gets steeper throughout the optimization [16]. It works on the filtered density field \bar{x} as visualized in Figure 2.8. Another way to obtain clear boundaries are filtering schemes based on image morphology as in [19] instead of the Heaviside projection.

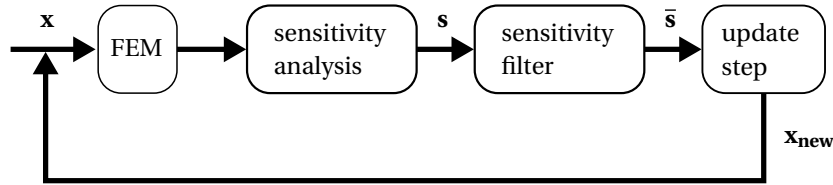


Figure 2.7: Diagram of sensitivity filtering, x are the design variables, s the sensitivities, \bar{s} the filtered sensitivities, and x_{new} the updated design variables at the end of the iteration

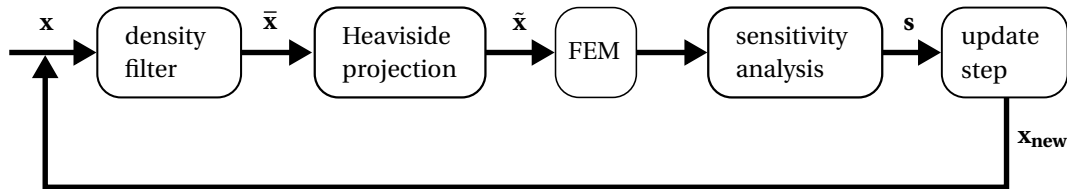


Figure 2.8: Diagram of density filtering (second and third type in list above), x are the design variables, s the sensitivities, \bar{x} the filtered design variables for the second type of filtering, \bar{x} the filtered sensitivities after Heaviside projection or alternatively image morphology filters (third type of filtering), and x_{new} the updated design variables at the end of the iteration

2.2.6. SOLVERS

The most widely used solvers for TO are the optimality criteria method (used in e.g. [24]), the method of moving asymptotes (denoted as MMA introduced by [25]) and sequential linear programming (denoted as SLP used in e.g. [15] and available in the MATLAB® function 'fmincon'), due to the fact that they are easy to implement and don't require Hessian information [26]. Another solver that has been used for TO problems but does make use of Hessian information, which is usually expensive to obtain, is sequential quadratic programming (typically designated as SQP).

3 PROBLEM ANALYSIS

In this section different aspects of the design problem are discussed in detail in order to come up with a list of requirements which can be used as a basis for the TO methodology.

To start simple, the 2D case of an 'in-plane infinite' hydrostatic bearing will be considered. In [Figure 3.1](#) the movement of the piston rod together with the compliant bearing pad is illustrated. The hydrostatic bearing consists of a deformable bearing pad at the bottom (indicated in orange) and the yet to be determined structure between the piston rod and the bearing pad. In the middle of the bearing pad sits the fluid supply.

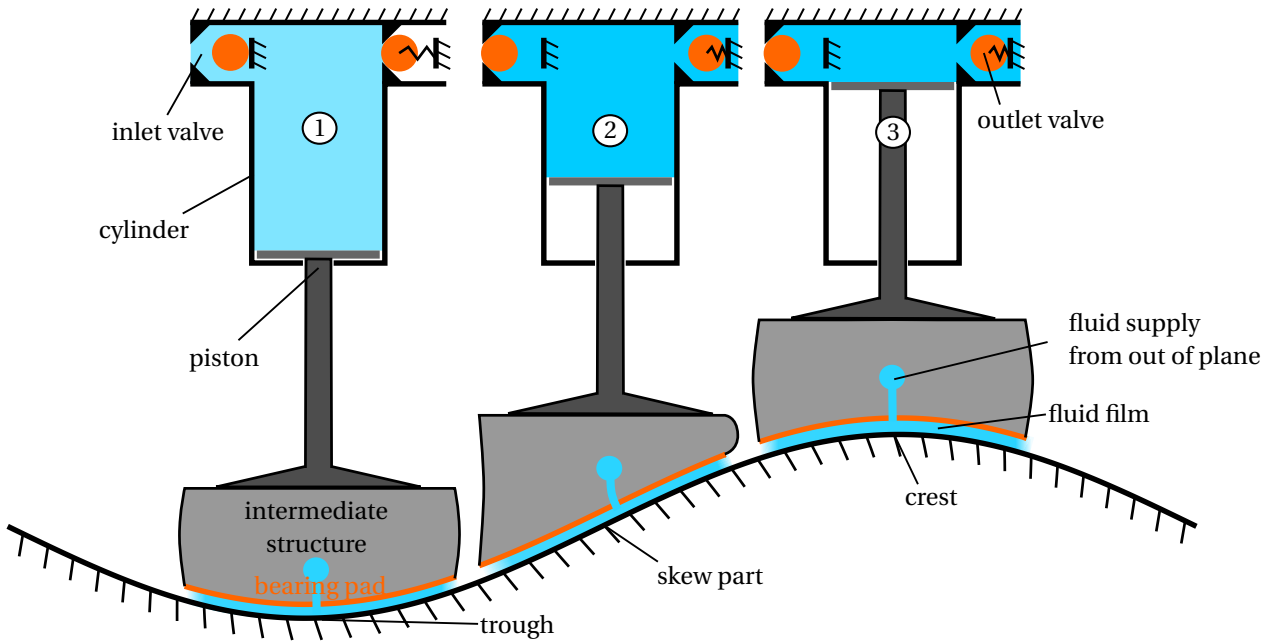


Figure 3.1: Visualization of the movement of the piston rod together with the yet to be determined structure for the hydrostatic bearing over the camring

3.1. ADAPTION TO COUNTER SURFACE

The amplitude of the sinusoidal counter surface for the desired bearing is assumed to be orders of magnitude greater than the variations in film height. Thus, the largest part of deformations on the bearing pad will come from following the shape of the camring. The intermediate structure should enable deformation of the compliant pad such that its shape matches the counter surface in all possible positions. A challenge here is that the stiffness between the top domain fixed to the rod and the bearing pad in vertical direction has to be high as well after full contact is made. This way the structure can transfer as much of the vertical motion of the camring as possible to the piston rod under the high pressure that is building up within the fluid.

3.2. LOAD CHARACTERISTICS

In order to gain some insight into the application [Figure 3.2](#) provides the expected load profile on the bearing for the wavelength of the camring. To give an order of magnitude [27] mentions the inlet pressure for a 600 kW prototype radial piston pump, being 30 Bar. After reaching its lowest position the piston will move back

up while the pressure of the fluid being pumped increases up to 160 Bar (in case of the prototype pump [27]). Note that the maximum pressure will be significantly higher for the further developed pumps in the DOT project. Although we could account for the fact that the loads are significantly reduced for the 'downward' movement, this is deemed outside the scope of this work and it's chosen to develop a symmetric bearing with similar load bearing capability in all positions.

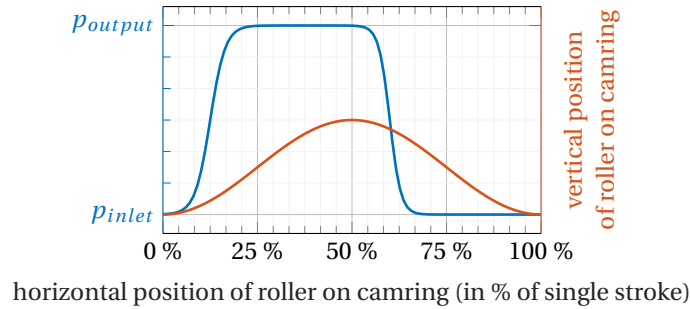


Figure 3.2: Expected total pressure inside cylinder

3.3. PAD LENGTH

The length of the compliant pad relative to the wavelength of the counter surface is an important parameter in the design of the bearing. A short pad will have a small surface area which leads to large fluid film pressures and small fluid film heights. The lower the fluid film, the higher the chance of making contact with the counter surface during movement over the sinusoidal camring. This is something that should be avoided as contact is expected to decrease performance and lifetime of the pump. The bearing pad should thus not be too short.

On the other hand, there are also some upper limits for the length of the compliant pad. For a large pad the compliant structure above it has deal with larger deformations. To investigate this the vertical deformations of the pad when sitting perfectly against the crest and the skew part of the camring have been determined for pad lengths between 1 % and 100 % of the wavelength λ . The deformations were averaged around zero for both cases. The ratio of the resulting maximum vertical deformations between the crest $y_{crest,max}$ and the skew part $y_{skew,max}$ for each pad length between 1 % and 100 % is plotted in Figure 3.4. What can be observed is that the maximum deformations received by the structure on the skew part are at minimum double the magnitude of the deformations at the crest for pad lengths between 0.01λ and 0.5λ .

Another thing to consider is the relation between the net motion of the compliant pad and the pad length. As one can imagine when the pad length equals λ it will no longer experience vertical motion and only adapt its shape to all possible configurations during movement over the camring. It is possible to find compliant structures which can generate vertical motion of the top domain for those kind of pad lengths. In this work however we focus on the development of structures with a pad length $\leq 0.5\lambda$, which means that the structure as a whole will be subject to net vertical motion during movement over the camring.

3.4. REACTION FORCE CONSIDERATIONS

In section 1.1 it has been stated that for a standard hydrostatic bearing with rigid bearing surface and symmetric loading condition the film height will be uniform. For the deformable hydrostatic bearing however, the fluid film pressure will lead to deformation of the bearing surface which in turn influences the fluid film height and pressure. In [9] it is stated by Nijssen that if compliance is introduced in the bearing surface, a recess will be formed for use above a flat counter surface (illustrated in Figure 3.5). Nijssen states that in this case the bearing is preloaded and has a predisposition towards a certain deformed state. To get a 'neutral' bearing without predisposition, Nijssen defines a stiffness distribution for the material of the bearing such that a uniform film height is achieved for a flat counter surface. The stiffness distribution is obtained by matching the reaction pressure profile of the compliant bearing, for compression against a flat plate, with the

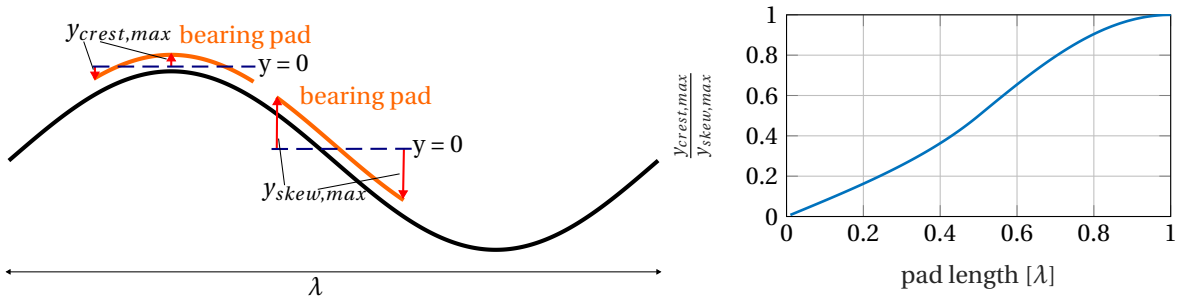


Figure 3.3: visualization of $y_{crest,max}$, $y_{skew,max}$ and λ for a pad length of 0.2λ

Figure 3.4: Ratio between maximum vertical displacement of the pad at the crest and the skew part, when averaged around zero, for pad lengths between 0.01λ and λ

pressure distribution in the fluid film of a bearing with uniform film height. This is shown in Figure 1.3. By measuring the reaction pressure of the bearing to be designed, we can thus determine if the bearing has a uniform film height for a flat counter surface.

A bearing with triangular stiffness profile has been confirmed to show minimal variations in film height during travel over a camring with surface waviness of 1/100th times the height of the bearing [9]. This strategy has not been applied for larger amplitudes of the counter surface, which is the aim in this work.

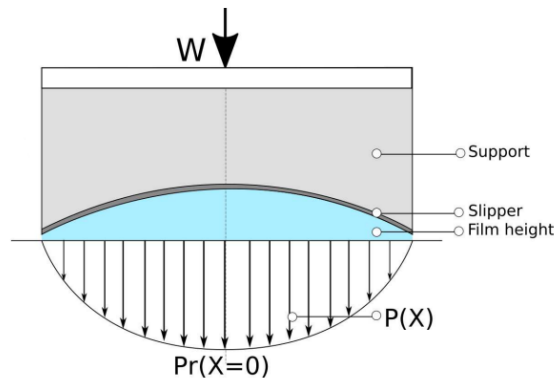


Figure 3.5: Expected deformation of a compliant hydrostatic bearing (retrieved from [8])

3.5. LIST OF REQUIREMENTS

Based on the discussion in the previous sections, a list of requirements is setup. Most importantly, the intermediate structure must enable adaption of the bearing pad to the counter surface while transferring as much of the net motion as possible, as explained in [section 3.1](#). The structure is also sought to minimize preference towards any of the positions on the camring which is why the approach introduced in [section 3.4](#) will be followed. The requirements are listed below:

1. enable deformation of the compliant pad into the shape of the counter surface for any position on the counter surface
2. provide large stiffness between top domain and compliant pad for any position on the counter surface
3. reaction pressure profile for compression against a flat surface should follow a triangular profile to get a 'neutral' bearing

4 TOPOLOGY OPTIMIZATION METHOD

The current chapter introduces the basic performance measures used in the optimizations which are strain energies (section 4.1). This is followed by the general problem formulation for the optimization problems in section 4.2. In the same section it is explained how the design problem is simplified (subsection 4.2.1) and which load cases are used for the strain energy calculations (subsection 4.2.2 and page 18). Explanation of how the additional requirement on the reaction profile of the structures is implemented in two different ways is provided in section 4.3. What follows are details about the utilized SIMP interpolation in section 4.4, and on the robust formulation page 22. The sensitivities for the utilized performance measures with respect to the design variables are provided in section 4.6 and the chapter is concluded with information about the implementation in section 4.7.

In order to obtain a structure which satisfies the requirements listed in section 3.1 first a suitable existing approach for compliant mechanism design with TO had to be found. As mentioned in subsection 2.2.2 there is not a single go-to method for compliant mechanism synthesis using TO. This work attempts to efficiently solve the design problem which is why a method had to be chosen which is convenient to implement, work with, and suitable for the problem. This has been found in the work of Koppen et al. in [28], where a methodology to generate compliant flexures with arbitrary degrees of freedom is developed. Extensions of the method in [29] show how even multiple-input-multiple-output mechanisms can be generated based with the same methodology. In the formulation, the strain energy is used as a measure of the stiffness of the designs in differing loading conditions.

There are two types of load cases which can be utilized in the considered TO formulation. In the first type (of which an example is shown in Figure 4.1a) the design domain is only subjected to applied forces under correctly implemented boundary conditions. As for the boundary conditions: the design domain has to be constrained such that rigid body motion is impossible in order to avoid singularities in the finite element calculation. This is done by prescribing the displacements to be zero for at least 1 degree of freedom for each dimension. The second type of load case (example shown in Figure 4.1b) is one where the design domain is purely subjected to prescribed displacements. In order to get a load case, the domain has to be subjected to nonzero prescribed displacements in addition to the displacements prescribed to be zero for the boundary conditions.

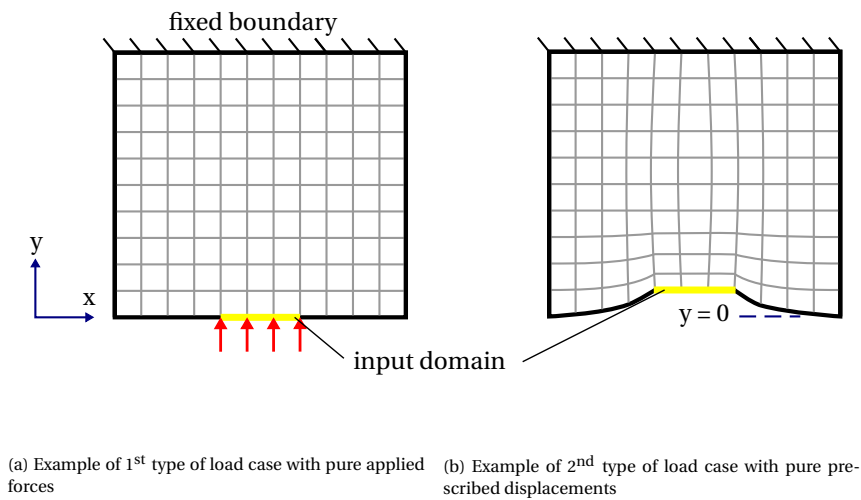


Figure 4.1: Illustration of the two types of load cases possible with the chosen TO method

4.1. STRAIN ENERGIES AS STIFFNESS MEASURE

We investigate the consequences of considering each type of those load cases. For this purpose, the finite element equation (previously given in Equation 2.1) is partitioned as follows:

$$\begin{bmatrix} \mathbf{f}_f \\ \mathbf{f}_p \end{bmatrix} = \begin{bmatrix} \mathbf{K}_{ff}(\mathbf{x}) & \mathbf{K}_{fp}(\mathbf{x}) \\ \mathbf{K}_{pf}(\mathbf{x}) & \mathbf{K}_{pp}(\mathbf{x}) \end{bmatrix} \begin{bmatrix} \mathbf{u}_f \\ \mathbf{u}_p \end{bmatrix} \quad (4.1)$$

where: \mathbf{f}_f = applied forces, \mathbf{f}_p = reaction forces, \mathbf{u}_f = displacements of free nodes, and \mathbf{u}_p = prescribed displacements. \mathbf{K}_{ff} , \mathbf{K}_{fp} , \mathbf{K}_{pf} and \mathbf{K}_{pp} are sub matrices of the partitioned stiffness matrix and depend on the design variables \mathbf{x} . They have the following properties:

$$\mathbf{K}_{ff} = \mathbf{K}_{ff}^T \quad (4.2)$$

$$\mathbf{K}_{pp} = \mathbf{K}_{pp}^T \quad (4.3)$$

$$\mathbf{K}_{fp} = \mathbf{K}_{pf}^T \quad (4.4)$$

By solving the governing equations (Equation 4.1) the deformations of the structure under all considered load cases are obtained. Based on that the strain energy for a specific load case can be calculated as follows:

$$SE = \frac{1}{2} \mathbf{u}^T \mathbf{K} \mathbf{u} = \frac{1}{2} \mathbf{u}^T \mathbf{f} \quad (4.5)$$

where SE is the strain energy of the considered load case, \mathbf{K} is the finite element stiffness matrix, \mathbf{u} is the vector containing the nodal displacements and \mathbf{F} is the vector containing the nodal reaction and applied forces. Combining Equation 4.1 and Equation 4.5 gives:

$$SE = \frac{1}{2} \begin{bmatrix} \mathbf{u}_f^T & \mathbf{u}_p^T \end{bmatrix} \begin{bmatrix} \mathbf{f}_f \\ \mathbf{f}_p \end{bmatrix} = \frac{1}{2} (\mathbf{u}_f^T \mathbf{f}_f + \mathbf{u}_p^T \mathbf{f}_p) \quad (4.6)$$

When considering the partitioned system under the loading case of pure applied loads (where $\mathbf{u}_p = \mathbf{0}$ and $\mathbf{f}_f \neq \mathbf{0}$) rewriting Equation 4.6 results in:

$$SE^f(\mathbf{x}) = \frac{1}{2} \mathbf{u}_f^T(\mathbf{x}) \mathbf{f}_f \quad (4.7)$$

The implicit dependence on the design variables \mathbf{x} is indicated here for clarification. It can be seen that in this case the strain energy is proportional to the displacements of the free nodes due to the fact that \mathbf{f}_f stays constant throughout the optimization. Larger displacements of the structure under the same applied forces means that the structure is less stiff for that particular load case. Therefore, **the strain energy is inversely proportional to the stiffness in a load case with pure applied forces**. Doing the same exercise for the load case of pure prescribed displacements (where $\mathbf{u}_p \neq \mathbf{0}$ and $\mathbf{f}_f = \mathbf{0}$) we obtain:

$$SE^p(\mathbf{x}) = \frac{1}{2} \mathbf{u}_p^T \mathbf{f}_p(\mathbf{x}) \quad (4.8)$$

In this case the strain energy is proportional to the reaction forces because \mathbf{u}_p is constant. Higher reaction forces for the same prescribed displacements means that the structure is stiffer. It can thus be concluded that **the strain energy is proportional to the stiffness for the load case of pure prescribed displacements**.

4.2. GENERAL PROBLEM FORMULATION

To set up a TO problem the load cases for which the structure is intended to have large stiffness, and the load cases for which the structure is intended to have low stiffness have to be defined. The strain energies of load cases for which large stiffness is desired are used in objective function to be minimized. A minus sign corrects for the differing proportionality between strain energy and stiffness for the two types of load cases such that stiffness maximization is achieved by minimization of the objective. Strain energies of the load cases under which the structure is intended to have low stiffness are implemented in the constraints. This works by setting an upper bound for the strain energies of the prescribed displacement cases, thereby limiting the stiffness. The general TO formulation for the optimization problems in this work can be given as:

$$\begin{aligned} \min_{\mathbf{x}} \quad & \sum \gamma_j SE_j^f(\mathbf{x}) - \sum \delta_k SE_k^p(\mathbf{x}) \quad j \in K_{\text{high}}^f, k \in K_{\text{high}}^p \\ \text{s.t.} \quad & SE_l^p(\mathbf{x}) \leq SE_{l,\text{max}}^p \quad l \in K_{\text{low}}^p \\ & \sum_{m=1}^{n_{el}} x_m \leq n_{el} V_{\text{max}} \quad 0 \leq x_m \leq 1 \end{aligned} \quad (4.9)$$

The design variables x are the densities of the individual elements in the finite element discretization and contained in the vector \mathbf{x} . In this work the finite element discretization corresponds with the discretization of the design domain. $K_{\text{high}}^f, K_{\text{high}}^p$ and K_{low}^p are subsets of the set containing the strain energies for all considered load cases in the optimization.

- K_{high}^f contains all strain energies of load cases with pure applied forces for which the structure should have high stiffness
- K_{high}^p contains all strain energies of load cases with pure prescribed displacements for which the structure should have high stiffness
- K_{low}^p contains all strain energies of load cases with pure prescribed displacements for which the structure should have low stiffness

The variables γ_j and δ_k are optional scaling factors for each individual strain energy term in the objective which can be used to tune the relative importance of individual load cases. SE_{max}^p is the upper bound for the strain energy of the respective load case and therefore limits the stiffness. V_{max} is the allowed volume fraction for the design and n_{el} is the number of elements in the discretization which is equal to the number of design variables.

4.2.1. SIMPLIFICATIONS OF THE PROBLEM

In order to solve the design problem with the formulation presented in [section 4.2](#) some simplifications of the problem have to be made. If one would follow the requirements listed in [section 3.1](#) exactly, an infinite amount of load cases would have to be considered for both the objective as well as the constraints:

1. objective: high stiffness in vertical direction at every position on the sinusoidal counter surface
2. constraint: enable deflection of the bearing pad such that it attains shape of the counter surface at each position

The number of load cases considered in the objective and constraints is desired to be kept as low as possible. Especially a large number of constraints results in significant computational expense. The simplification is made to seek stiffness in vertical direction for a flat counter surface as further described in [subsection 4.2.2](#). Also the deformations of the bearing pad to match the positions on the counter surface, have to be described efficiently. If the bearing pad would be combined with a rotational joint, the needed deformations of the pad can be simplified as positive and negative curvature (and everything in between). Therefore the load cases considered in the constraints are the deformation of the bearing pad in the skew part of the counter surface (resembling the deformations of a rotational joint), and at the crest or trough (resembling positive and negative curvature). This is further described in [subsection 4.2.3](#).

4.2.2. LOAD CASES FOR OBJECTIVE

To achieve high stiffness for actuation of the whole bearing pad in vertical direction, either of the load cases shown in [Figure 4.2](#) can be utilized for the objective. When using the load case shown in [Figure 4.2a](#), where a distributed force is applied to the bottom boundary, the corresponding strain energy term SE_y^f is minimized in the objective. For use of the load case shown in [Figure 4.2b](#), where a uniform displacement of the bottom boundary in vertical direction is applied, the corresponding strain energy term SE_y^p is maximized in the objective (because of the minus sign in the objective for this term in [Equation 4.9](#)).

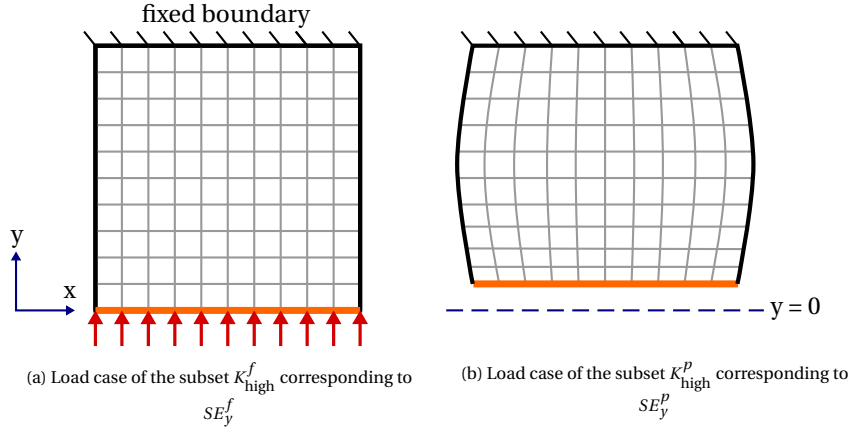


Figure 4.2: Load cases used in the objective for stiffness maximization in vertical direction for a design domain and FE- discretization of 10x10 elements

Optionally stiffness in horizontal direction can be achieved by inclusion of one of the load cases shown in Figure 4.3. When using the load case shown in Figure 4.3a, where a distributed force is applied to the bottom boundary, the corresponding strain energy term SE_x^f is minimized in the objective. For use of the load case shown in Figure 4.3b, where a uniform displacement of the bottom boundary in vertical direction is applied, the corresponding strain energy term SE_x^p is maximized in the objective. Note that the strain energy is equal for the force or prescribed displacement acting in opposite direction. Therefore only the presented load case has to be included.

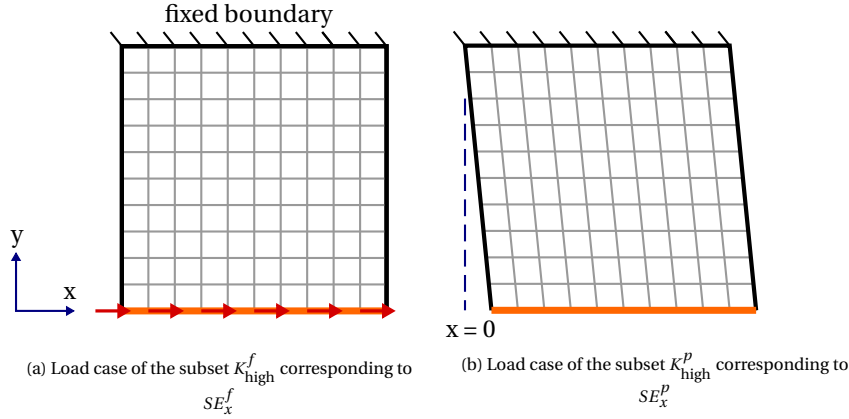


Figure 4.3: Load cases used in the objective for stiffness maximization in horizontal direction for a design domain and FE- discretization of 10x10 elements

4.2.3. LOAD CASES FOR CONSTRAINTS

As described in subsection 4.2.1, the considered load cases for the constraints are deformation of the bearing pad in the skew part of the counter surface and at the crest or trough. In the real case the deformations of the bearing pad have to be achieved under compressive loads. The prescribed displacements however are averaged around zero for the skew case as this resembles the behavior of a rotational joint for pad lengths smaller than 0.5λ . This is illustrated in Figure 4.4a. The corresponding strain energy SE_{skew}^p is constrained by $SE_{\text{skew,max}}^p$ which limits the stiffness for those deformations:

$$SE_{\text{skew}}^p \leq SE_{\text{skew,max}}^p \quad (4.10)$$

For the prescribed displacements at the crest or trough a configurable offset from zero is implemented around which the displacements are averaged (see Figure 4.4b). We remind that the strain energy will not change if the prescribed displacements act in opposite direction. This means that the strain energy for the case where the prescribed displacements imitate the structure sitting at the crest, is equal to the case where the

prescribed displacements imitate the structure sitting at the trough with opposite offset. For this reason, only one of the two cases has to be considered in the constraints if the offset is chosen appropriately. This is further explained in the following section. The strain energy corresponding to SE_{crest}^p is constrained by $SE_{crest,max}^p$ which limits the stiffness for those deformations:

$$SE_{crest}^p \leq SE_{crest,max}^p \quad (4.11)$$

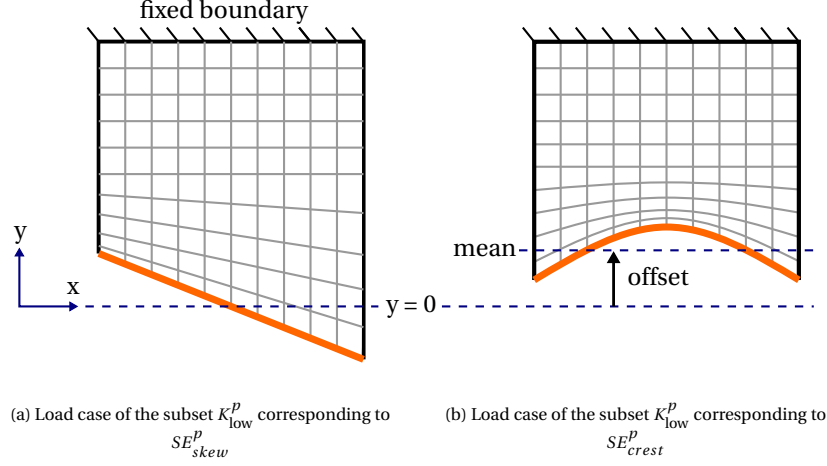


Figure 4.4: Load cases used in the constraints on the stiffness for a design domain and FE- discretization of 10x10 elements

INFLUENCE OFFSET PARAMETER

The load case for the structure sitting at the crest can be adapted through the offset. For an offset of zero the displacements are averaged around zero and the design domain is subjected to an equal amount of positive and negative prescribed displacements. Since the strain energy term SE_{crest}^p is independent of the sign of the displacements, the strain energy for the case where the displacements of the trough are averaged around zero is exactly the same as for the crest. In Figure 4.5 the prescribed displacements for the load case corresponding to SE_{crest}^p is given for different offsets and a pad length of being 20 % of the wavelength of the counter surface (meaning: pad length = 0.2λ). The strain energy equivalent displacements are shown in the same respective colors with dashed lines. Intersection of the strain energy equivalent displacement cases always happens where the prescribed displacement is zero. This means that the resulting structure should enable rotation at these intersections for the bottom domain to switch between the strain energy equivalent cases. As visible in Figure 4.5 these 'rotation points' can be shifted through adaption of the offset.

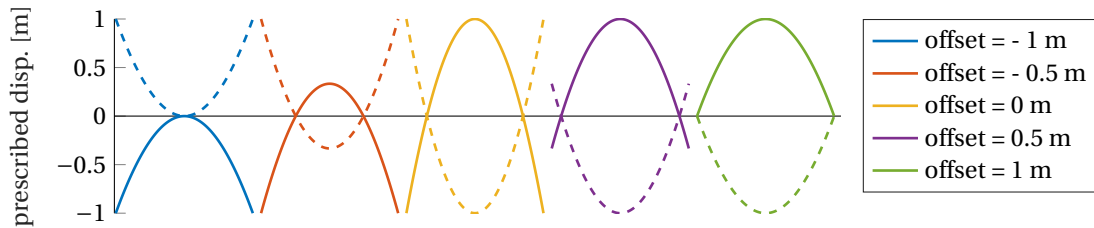


Figure 4.5: Prescribed displacements of the bottom domain for the load case corresponding to SE_{crest}^p together with their strain energy equivalent counterpart (dashed lines with respective same color) for pad length of 0.2λ

4.3. REACTION FORCE PENALTY/CONSTRAINT

As stated in the third requirement in section 3.5 the reaction force profile for compression against a flat surface should follow a triangular profile. Satisfaction of this requirement is expected to result in a hydrostatic bearing without preference towards either a convex or concave shaped counter surface which both are

present on a sinusoidal counter surface. Two different approaches were implemented in the optimizations in order to achieve this. Those are described in detail in [subsection 4.3.1](#) and [subsection 4.3.2](#).

4.3.1. PRESSURE PROFILE MATCHING

To achieve a triangular reaction profile for uniform compression a penalty term is implemented in the optimization. As an approximation for the reaction pressure, to avoid an expensive contact study during the optimization, we use the reaction forces. Those can be obtained based on [Equation 4.1](#):

$$\mathbf{f}_p(\mathbf{x}) = \mathbf{K}_{pf}(\mathbf{x})\mathbf{u}_f(\mathbf{x}) + \mathbf{K}_{pp}(\mathbf{x})\mathbf{u}_p \quad (4.12)$$

\mathbf{f}_p implicitly depends on \mathbf{x} through the explicit dependence of \mathbf{K}_{pf} and \mathbf{K}_{pp} and the implicit dependence of \mathbf{u}_f on \mathbf{x} . In order to let the reaction forces at the bottom boundary ($\mathbf{f}_{p,bot}$) adopt the shape of a desired predefined profile the dot product formulation developed by Maas et. al [30] is utilized:

$$P(\mathbf{x}) = 1 - \frac{\mathbf{f}_{p,bot}^{\text{tar}} \cdot \mathbf{f}_{p,bot}(\mathbf{x})}{|\mathbf{f}_{p,bot}^{\text{tar}}| |\mathbf{f}_{p,bot}(\mathbf{x})|} \quad (4.13)$$

Here $\mathbf{f}_{p,bot}^{\text{tar}}$ is a vector describing the desired shape of the reaction forces at the bottom of the design domain ($\mathbf{f}_{p,bot}$). The term P approaches zero if the shapes of $\mathbf{f}_{p,bot}^{\text{tar}}$ and $\mathbf{f}_{p,bot}$ are equal, and approaches one if the shapes of $\mathbf{f}_{p,bot}^{\text{tar}}$ and $\mathbf{f}_{p,bot}$ are completely different. The relative magnitude of the vectors with respect to each other has no influence due to division by the product of the magnitudes of the vectors. This makes it convenient to implement P as the magnitude of the reaction forces does not have to be predicted which would be the case for other shape morphing formulations. Note that P can both be implemented directly in the objective function as a penalty term to be added to the existing objective or as a constraint. In this work P is implemented as a penalty so that a constraint value does not have to be tuned.

Two possibilities for the load case under which the reaction forces are determined are shown in [Figure 4.6](#). The top boundary is either subjected to a uniformly distributed force (see [Figure 4.6a](#)) or a uniform prescribed displacement (see [Figure 4.6b](#)) in vertical direction. Nodes at the bottom boundary are free to move in horizontal direction except the node on the left side which is fixed against movement in horizontal direction. This way the problem is properly constrained while approaching a contact interface in the best way possible with a linear FE analysis

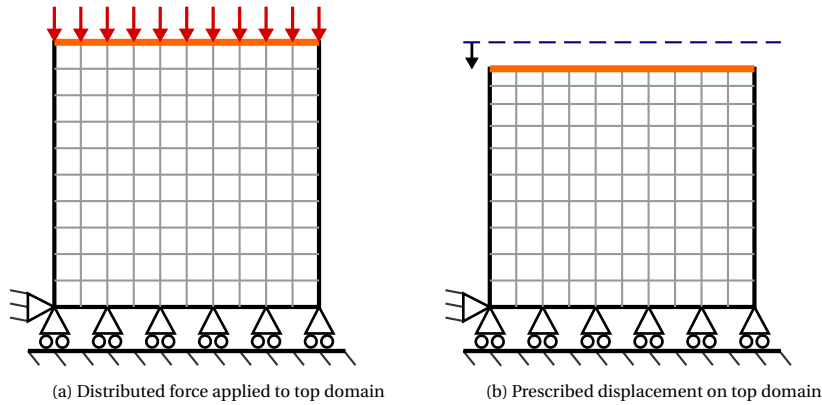


Figure 4.6: Possible load cases for determination of the reaction forces $\mathbf{f}_{p,bot}$ for a design domain and FE- discretization of 10x10 elements

4.3.2. SOFT REACTION CONSTRAINT

In an alternative approach the requirement for the reaction force profile is attempted to be relaxed to make it easier for the optimizer to find a solution. Here the reaction forces are only required to monotonically decrease from the middle to the sides. There is thus no strictly prescribed shape which is why we call it soft reaction constraint. The way this is done is that the bottom domain is first split into the left and right side.

For the left side, the reaction force of each node (except the leftmost one) is subtracted by the reaction force of the node on the left side of it. This way we obtain a measure Δ_{left} which is positive if the reaction force of the current node is higher than then one to the left and negative otherwise for each pair of nodes:

$$\Delta_{\text{left},i}(\mathbf{x}) = \mathbf{f}_{p,bot,j}(\mathbf{x}) - \mathbf{f}_{p,bot,j-1}(\mathbf{x}) \quad j = 2, 3, \dots, n_{\text{left}} \quad (4.14)$$

where i is the index of the pair of considered nodes, j is the index of the nodes at the bottom domain starting on the left and n_{left} is the index of the last node on the left side. The same thing is done for the right side:

$$\Delta_{\text{right},k}(\mathbf{x}) = \mathbf{f}_{p,bot,j}(\mathbf{x}) - \mathbf{f}_{p,bot,j+1}(\mathbf{x}) \quad j = n_{\text{left}} + 1, n_{\text{left}} + 2, \dots, n_{\text{right}} \quad (4.15)$$

where k is the index of the pair of considered nodes and n_{right} is the index of the last node on the right side. In order to have a monotonic decrease of the reaction force from the middle of the bottom domain $\Delta_{\text{left},i}$ and $\Delta_{\text{right},k}$ should be positive. To avoid implementing all of those values as an individual constraint, which is computationally expensive, they are aggregated in a sum. A smooth maximum function [31] is used to make the negative values of $\Delta_{\text{left},i}$ and $\Delta_{\text{right},k}$ approach zero:

$$C(\mathbf{x}) = \sum_{i=1} \frac{\ln(1 + e^{k_{sm}\Delta_{\text{left},i}(\mathbf{x})})}{k_{sm}} + \sum_{k=1} \frac{\ln(1 + e^{k_{sm}\Delta_{\text{right},k}(\mathbf{x})})}{k_{sm}} \quad (4.16)$$

This way, a measure C is obtained which attains a larger value the better forces are monotonically decreasing from the middle to the sides. The parameter k_{sm} is used to control the smoothness of the transition as visualized in figure Figure 4.7. C is implemented as an additional constraint in the formulation presented in

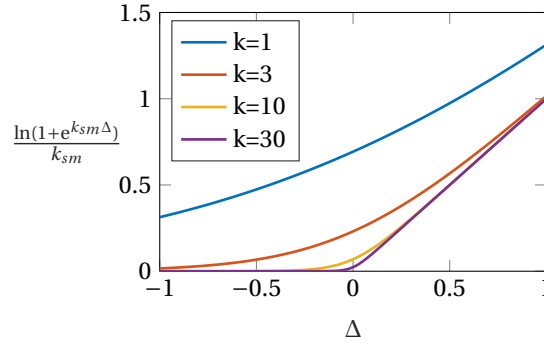


Figure 4.7: Visualization of the smooth maximum function used in $C(\mathbf{x})$ for Δ between -1 and 1

Equation 4.9 like shown below:

$$C \leq u_b \quad (4.17)$$

where u_b is a configurable upper bound for C which is essentially the allowed constraint violation.

4.4. FILTERING AND SIMP

In order to avoid checkerboarding and to achieve mesh independence the implemented method makes use of a density filter [32] on the design variable field \mathbf{x} , which is the second type of filter explained in subsection 2.2.5. The filtered field is called the physical field and represented by $\bar{\mathbf{x}}$. In this work we use SIMP (as explained in subsection 2.2.1) to penalize intermediate densities. This way the optimizer is forced to converge to black and white solutions which can be interpreted as compliant mechanisms. The filtered design variables \bar{x} from the field $\bar{\mathbf{x}}$ are used in the SIMP interpolation that modifies the Young's moduli of the elements:

$$E_i = E_{min} + \bar{x}_i^p (E_{mat} - E_{min}) \quad (4.18)$$

Division of above equation by E_{mat} results in another field which will be denoted as $\hat{\mathbf{x}}$ [30]:

$$\hat{x}_i = \frac{E_{min}}{E_{mat}} + \bar{x}_i^p \left(1 - \frac{E_{min}}{E_{mat}}\right) \quad (4.19)$$

The stiffness matrix of the FE analysis depends on $\hat{\mathbf{x}}$ (i.e. $\mathbf{K}(\hat{\mathbf{x}})$). A penalization power of $p = 3$ was implemented for the optimizations in this work.

4.5. ROBUST FORMULATION

To enforce convergence to black and white solutions the robust formulation, introduced by Sigmund [33] and Wang [34], is used whenever needed. Robustness against manufacturing errors and length scale control on the features in both the solid and void phase are the most important reasons to choose for the robust formulation over a single Heaviside projection. The way it works is that the filtered densities \bar{x} are projected onto three new fields through a smooth Heaviside projection (type 3 filter described in subsection 2.2.5):

$$\begin{aligned}\tilde{x}_e &= \frac{\tanh(\beta\eta_e) + \tanh(\beta(\bar{x} - \eta_e))}{\tanh(\beta\eta_e) + \tanh(\beta(1 - \eta_e))} & 0.5 < \eta_e < 1 \\ \tilde{x}_i &= \frac{\tanh(\beta\eta_i) + \tanh(\beta(\bar{x} - \eta_i))}{\tanh(\beta\eta_i) + \tanh(\beta(1 - \eta_i))} & \eta_i = 0.5 \\ \tilde{x}_d &= \frac{\tanh(\beta\eta_d) + \tanh(\beta(\bar{x} - \eta_d))}{\tanh(\beta\eta_d) + \tanh(\beta(1 - \eta_d))} & 0 < \eta_d < 0.5\end{aligned}\quad (4.20)$$

where β is a projection parameter controlling the steepness of the smooth Heaviside step. A larger value for β leads to less grey area in the designs. This parameter is gradually increased during the optimization in order to relax the problem in the initial phase and avoid getting into local minima early. η_e is the threshold for the eroded field \tilde{x}_e , η_i the threshold for the intermediate field \tilde{x}_i , and η_d the threshold for the dilated field \tilde{x}_d . The behavior of the projections is shown in Figure 4.8 where the densities \tilde{x} corresponding to the fields \tilde{x}_e , \tilde{x}_i and \tilde{x}_d are shown for all values the density \bar{x} of the physical field \bar{x} can attain. For the eroded field, elements with intermediate densities are more likely to be projected onto the void phase (density equal to zero) leading to a uniformly 'shrunk' version of the design with respect to the intermediate field. On the contrary, in the dilated field elements with intermediate densities are more likely to be projected to the solid phase (density equal one) which leads to a uniformly 'thickened' representation of the design. The intermediate field provides the final representation of the topology which is robust against manufacturing errors and is free of features smaller than the minimum feature size. In this work the distance of η_e and η_d to $\eta_i = 0.5$, which is

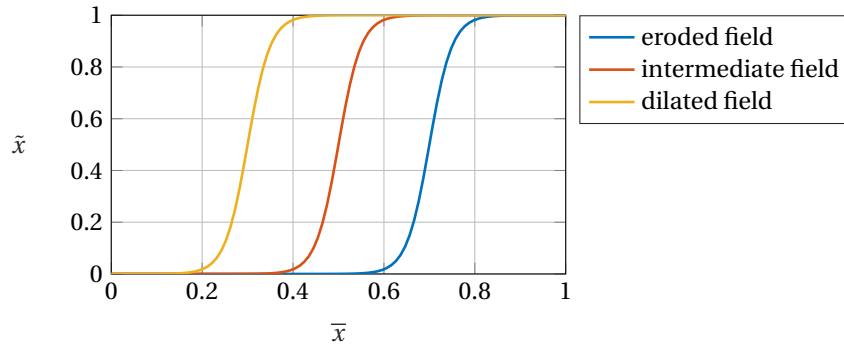


Figure 4.8: Visualization of the 3 projections of the filtered field \bar{x} onto the projected fields \tilde{x}_e , \tilde{x}_i and \tilde{x}_d for $\beta = 20$, $\eta_e = 0.7$ and $\eta_d = 0.3$

the parameter controlling the robustness, is denoted as Δ_η where:

$$\Delta_\eta = \eta_e - 0.5 = 0.5 - \eta_d \quad (4.21)$$

The minimum feature size which is equal for both the solid and void phase can be controlled by the radius of the density filter and Δ_η . Larger values for the filter radius or Δ_η lead to a larger minimal feature size and thus suppression of small features in the intermediate design.

The eroded representation will always have the lowest stiffness while the dilated representation has the highest stiffness. To achieve robustness against manufacturing errors the worst performing representation in terms of stiffness (being the eroded field) will be used for the objective where maximum stiffness is sought. For the constraints, where low stiffness is sought, the worst performing representation in terms of stiffness (being the dilated field) is utilized. The general robust problem formulation (based on Equation 4.9) is given

below:

$$\begin{aligned}
\min_{\mathbf{x}} \quad & \sum \alpha_j SE_j^f(\tilde{\mathbf{x}}_e) - \sum \gamma_k SE_k^p(\tilde{\mathbf{x}}_e) \quad j \in K_{\text{high}}^f, k \in K_{\text{high}}^p \\
\text{s.t.} \quad & SE_l^p(\tilde{\mathbf{x}}_d) \leq SE_{l,\text{max}}^p \quad l \in K_{\text{low}}^p \\
& \sum_{m=1}^{n_{el}} \tilde{x}_{d,m} \leq n_{el} V_{\text{max}}^* \quad 0 \leq x_m \leq 1
\end{aligned} \tag{4.22}$$

Here the densities of the dilated field \tilde{x}_d which are contained in the vector $\tilde{\mathbf{x}}_d$ are used in the volume constraint. V_{max}^* is updated every 20th iteration as follows:

$$V_{\text{max}}^* = V_{\text{max}} * \frac{\sum_{m=1}^{n_{el}} \tilde{x}_{d,m}}{\sum_{n=1}^{n_{el}} \tilde{x}_{i,n}} \tag{4.23}$$

where \tilde{x}_i are the densities of the intermediate field contained in the vector $\tilde{\mathbf{x}}_i$. This way the volume of the intermediate design ($\sum_{n=1}^{n_{el}} \tilde{x}_{i,n}$) becomes equal to V_{max} [34]. Note that for every field that is utilized in the optimization a governing equation has to be solved. In case of Equation 4.22 there are thus two governing equations. The governing equations for all three fields are provided below.

$$\mathbf{f}^e = \mathbf{K}(\tilde{\mathbf{x}}(\tilde{\mathbf{x}}_e)) \mathbf{u}^e \quad \mathbf{f}^i = \mathbf{K}(\tilde{\mathbf{x}}(\tilde{\mathbf{x}}_i)) \mathbf{u}^i \quad \mathbf{f}^d = \mathbf{K}(\tilde{\mathbf{x}}(\tilde{\mathbf{x}}_d)) \mathbf{u}^d \tag{4.24}$$

For the performance parameters of the reaction force profile it is not possible to predict which of the three design presentations will perform worst. Therefore, the terms have to be evaluated for all three fields as shown for P below:

$$P_e(\tilde{\mathbf{x}}_e) = 1 - \frac{\mathbf{f}_{p,\text{bot}}^{\text{tar}} \cdot \mathbf{f}_{p,\text{bot}}^e(\tilde{\mathbf{x}}_e)}{|\mathbf{f}_{p,\text{bot}}^{\text{tar}}| |\mathbf{f}_{p,\text{bot}}^e(\tilde{\mathbf{x}}_e)|} \quad P_i(\tilde{\mathbf{x}}_i) = 1 - \frac{\mathbf{f}_{p,\text{bot}}^{\text{tar}} \cdot \mathbf{f}_{p,\text{bot}}^i(\tilde{\mathbf{x}}_i)}{|\mathbf{f}_{p,\text{bot}}^{\text{tar}}| |\mathbf{f}_{p,\text{bot}}^i(\tilde{\mathbf{x}}_i)|} \quad P_d(\tilde{\mathbf{x}}_d) = 1 - \frac{\mathbf{f}_{p,\text{bot}}^{\text{tar}} \cdot \mathbf{f}_{p,\text{bot}}^d(\tilde{\mathbf{x}}_d)}{|\mathbf{f}_{p,\text{bot}}^{\text{tar}}| |\mathbf{f}_{p,\text{bot}}^d(\tilde{\mathbf{x}}_d)|} \tag{4.25}$$

The same procedure is applied to C . The results are aggregated in a smooth maximum operation in order to arrive at a single penalty or constraint value which is close to the one of the worst performing field:

$$P_{\text{rob}}(\tilde{\mathbf{x}}_e, \tilde{\mathbf{x}}_i, \tilde{\mathbf{x}}_d) = \frac{\ln(e^{k*P_e} + e^{k*P_i} + e^{k*P_d})}{k} \tag{4.26}$$

$$C_{\text{rob}}(\tilde{\mathbf{x}}_e, \tilde{\mathbf{x}}_i, \tilde{\mathbf{x}}_d) = \frac{\ln(e^{k*C_e} + e^{k*C_i} + e^{k*C_d})}{k} \tag{4.27}$$

Here, k is controlling the 'strictness' of the soft maximum [31]. It was manually tuned and a value of $k = 600$ was used for P_{rob} while a value of $k = 6$ was used for C_{rob} .

4.6. SENSITIVITIES

The gradient based optimizer used in this work must be provided with the sensitivities of the objective and constraints with respect to the design variables. The design variables \mathbf{x} are first modified by the density filter resulting in the field $\bar{\mathbf{x}}$. If the robust formulation is used, the filtered field $\bar{\mathbf{x}}$ goes through the Heaviside projections which results in fields $\tilde{\mathbf{x}}_e$, $\tilde{\mathbf{x}}_i$, and $\tilde{\mathbf{x}}_d$. In case the robust formulation is not utilized, the filtered field $\bar{\mathbf{x}}$ gets modified by the SIMP interpolation into the field $\hat{\mathbf{x}}$. For the robust formulation, the fields $\tilde{\mathbf{x}}_e$, $\tilde{\mathbf{x}}_i$, and $\tilde{\mathbf{x}}_d$ get modified by the SIMP interpolation into the fields $\hat{\mathbf{x}}_e$, $\hat{\mathbf{x}}_i$, and $\hat{\mathbf{x}}_d$ respectively. This means that the chain rule has to be applied in order to obtain the sensitivities for any response $f(\hat{\mathbf{x}})$ with respect to the design variables \mathbf{x} . Without the robust formulation the sensitivities in general form can be given as:

$$\frac{df}{d\mathbf{x}} = \frac{df}{d\hat{\mathbf{x}}} \frac{d\hat{\mathbf{x}}}{d\bar{\mathbf{x}}} \frac{d\bar{\mathbf{x}}}{d\mathbf{x}} \tag{4.28}$$

To obtain $\frac{d\bar{\mathbf{x}}}{d\mathbf{x}}$ the same filter as used for the densities (section 4.4) is applied to the sensitivities. The sensitivity of the SIMP-field $\hat{\mathbf{x}}$ with respect to the i -th element of $\bar{\mathbf{x}}$ is given below:

$$\frac{\partial \hat{\mathbf{x}}}{\partial \bar{x}_i} = p \bar{x}_i^{p-1} \left(1 - \frac{E_{\text{min}}}{E_{\text{mat}}} \right) \tag{4.29}$$

For the robust formulation, a general form of the sensitivities is provided below:

$$\frac{df}{d\mathbf{x}} = \frac{df}{d\hat{\mathbf{x}}} \frac{d\hat{\mathbf{x}}}{d\bar{\mathbf{x}}} \frac{d\bar{\mathbf{x}}}{d\mathbf{x}} \quad (4.30)$$

$\frac{d\hat{\mathbf{x}}}{d\bar{\mathbf{x}}}$ is calculated the same way as in Equation 4.29 with the difference of acting on the field $\hat{\mathbf{x}}$ instead of $\bar{\mathbf{x}}$. In the robust case, the term $\frac{d\bar{\mathbf{x}}}{d\mathbf{x}}$ has to be calculated additionally which is shown below (based on Equation 4.20):

$$\frac{d\bar{\mathbf{x}}}{d\mathbf{x}} = \frac{\beta \text{sech}^2(\beta(\bar{\mathbf{x}} - \eta_e))}{\tanh(\beta\eta_e) + \tanh(\beta(1 - \eta_e))} \quad (4.31)$$

4.6.1. SENSITIVITIES OF STRAIN ENERGY TERMS

The sensitivities of the strain energy terms with respect to the field $\hat{\mathbf{x}}$ are given below. Further details and derivation can be found in Appendix A.1.

$$\frac{dSE^f}{d\hat{\mathbf{x}}} = -\frac{1}{2} \mathbf{u}^T \frac{d\mathbf{K}}{d\hat{\mathbf{x}}} \mathbf{u} \quad (4.32) \quad \frac{dSE^p}{d\hat{\mathbf{x}}} = \frac{1}{2} \mathbf{u}^T \frac{d\mathbf{K}}{d\hat{\mathbf{x}}} \mathbf{u} \quad (4.33)$$

4.6.2. SENSITIVITIES OF PERFORMANCE MEASURES FOR REACTION FORCE PROFILE

PRESSURE PROFILE MATCHING

In order to obtain the sensitivities for P with respect to the design variables \mathbf{x} it is useful to first split up the sensitivity of P with respect to the field $\hat{\mathbf{x}}$ like shown below:

$$\frac{dP}{d\hat{\mathbf{x}}} = \frac{dP}{d\mathbf{f}_{p,bot}} \frac{d\mathbf{f}_{p,bot}}{d\hat{\mathbf{x}}} \quad (4.34)$$

Here, $\frac{dP}{d\mathbf{f}_{p,bot}}$ is a row vector with the same length as $\mathbf{f}_{p,bot}$ and $\frac{d\mathbf{f}_{p,bot}}{d\hat{\mathbf{x}}}$ is a matrix where each row contains the sensitivities for the respective reaction force component at the bottom. Using the quotient rule the sensitivities of P with respect to $\mathbf{f}_{p,bot}$ can be given as:

$$\frac{dP}{d\mathbf{f}_{p,bot}} = -\frac{|\mathbf{f}_{p,bot}^{\text{tar}}| |\mathbf{f}_{p,bot}| \mathbf{f}_{p,bot}^{\text{tar}^T} - \mathbf{f}_{p,bot}^{\text{tar}} \cdot \mathbf{f}_{p,bot} |\mathbf{f}_{p,bot}^{\text{tar}}|^{\frac{1}{2}} \frac{1}{|\mathbf{f}_{p,bot}|} 2\mathbf{f}_{p,bot}^T}{|\mathbf{f}_{p,bot}^{\text{tar}}|^2 |\mathbf{f}_{p,bot}|^2} \quad (4.35)$$

We make use of selection vectors \mathbf{s} to select each respective reaction force component of the bottom domain from \mathbf{f}_p as follows:

$$\mathbf{f}_{p,bot,i} = \mathbf{s}_i \mathbf{f}_p \quad (4.36)$$

The sensitivities of any response $g(\mathbf{f}_p)$ dependent on the reaction forces are derived in detail in Appendix A.2 for the utilized load case. Due to the fact that $\mathbf{f}_{p,bot,i}$ is dependent on \mathbf{f}_p (as just shown) the sensitivities with respect to the field $\hat{\mathbf{x}}$ can be given as:

$$\frac{d\mathbf{f}_{p,bot,i}}{d\hat{\mathbf{x}}} = \begin{bmatrix} -\lambda_f^T & \mathbf{s}_i^T \end{bmatrix} \frac{d\mathbf{K}}{d\hat{\mathbf{x}}} \mathbf{u} \quad (4.37)$$

where:

$$\lambda_f^T = \mathbf{s}_i \mathbf{K}_{pf} \mathbf{K}_{ff}^{-1} \quad (4.38)$$

SOFT REACTION FORCE CONSTRAINT

The sensitivities for C are obtained as follows:

$$\frac{dC}{d\hat{\mathbf{x}}} = \frac{dC}{d\Delta} \frac{d\Delta}{d\mathbf{f}_{p,bot}} \frac{d\mathbf{f}_{p,bot}}{d\hat{\mathbf{x}}} \quad (4.39)$$

where:

$$\frac{dC}{d\Delta} = \sum_{i=1} \frac{e^{k_{sm}\Delta_{left,i}}}{1 + e^{k_{sm}\Delta_{left,i}}} + \sum_{k=1} \frac{e^{k_{sm}\Delta_{right,k}}}{1 + e^{k_{sm}\Delta_{right,k}}} \quad (4.40)$$

Equation 4.37 can be utilized to obtain $\frac{d\Delta}{df_{p,bot}} \frac{df_{p,bot}}{d\mathbf{\hat{x}}}$ which is straightforward.

ROBUST FORMULATION

The sensitivities of the smooth maximum operation given in Equation 4.26 and Equation 4.27 with respect to $\mathbf{\hat{x}}$ are provided below:

$$\frac{dP_{rob}}{d\mathbf{\hat{x}}} = \frac{e^{k*P_e} \frac{dP}{d\mathbf{\hat{x}}_e} + e^{k*P_i} \frac{dP}{d\mathbf{\hat{x}}_i} + e^{k*P_d} \frac{dP}{d\mathbf{\hat{x}}_d}}{e^{k*P_e} + e^{k*P_i} + e^{k*P_d}} \quad (4.41)$$

$$\frac{dC_{rob}}{d\mathbf{\hat{x}}} = \frac{e^{k*C_e} \frac{dC}{d\mathbf{\hat{x}}_e} + e^{k*C_i} \frac{dC}{d\mathbf{\hat{x}}_i} + e^{k*C_d} \frac{dC}{d\mathbf{\hat{x}}_d}}{e^{k*C_e} + e^{k*C_i} + e^{k*C_d}} \quad (4.42)$$

4.7. IMPLEMENTATION

The topology optimizations in this work are performed using MATLAB®. To perform the optimizations in this work the code from Koppen et al in [28] which is based on the very popular 88-line TO code [35] was used as a starting point. The design domain is rectangular and discretized into square elements similar to the finite element discretization. The utilized optimizer is the famous MMA algorithm by Svanberg [25].

For every strain energy term that is utilized in the optimization, the corresponding system of equations is solved to obtain the displacements. MATLAB automatically uses the QR-solver for this purpose. The decomposition is reused for load cases with the same boundary conditions which means that (in case of the robust formulation) a single decomposition for all strain energies per set (K_{high}^f , K_{high}^p or K_{low}^p) is performed. For the robust formulation, inclusion of the reaction force constraint/penalty adds three systems of equations that have to be solved every iteration. As those are regarding three different fields, the decomposition can not be reused in this case.

In order to ensure correct implementation of the sensitivities, a finite difference check was performed for all of those before performing the optimizations.

5 TOPOLOGY OPTIMIZATION RESULTS

In this chapter the results of the TO runs based on the methodology presented in [chapter 4](#) are provided in a structured manner. After presentation of the utilized parameters for the optimizations in [section 5.1](#), follows an investigation into the influence of the offset parameter on the results ([section 5.2](#)). Thereafter, the choice of the utilized load case for the objective is clarified. The results of optimizations without implemented requirement on the reaction profile are presented and discussed in [section 5.4](#). Outcomes of optimizations which included a requirement on the reaction profile are provided and discussed in [section 5.5](#). Finally, results for optimizations which included a requirement on the horizontal stiffness are presented in [section 5.6](#).

As a general note on how the most important designs in this chapter are named, we provide a short clarification. Designs obtained through optimizations with the same combination of the constraint values $SE_{crest,max}^p$ and $SE_{skew,max}^p$ have been named with the same letter. The letter is followed by a subscript containing an abbreviation indicating the problem setup. A table which explains the utilized abbreviations is presented below:

Table 5.1: Used abbreviations to name the TO results

Abbreviation	Explanation
std	'standard' optimization without requirement on the reaction constraint (Table 5.5)
r,f	optimization with the pressure profile matching penalty utilizing the distributed force load case (Table 5.8)
r,d	optimization with the pressure profile matching penalty utilizing the prescribed displacement load case (Table 5.9)
tri	optimization without requirement on the reaction constraint using a triangular force for the objective (Table 5.10)
pad	optimization with the pressure profile matching penalty and a low stiffness pad (Table 5.11)
r,f2	same as (r,f) with a coarser mesh to determine the reaction profile ('coarseness' indicated by the number) (Table 5.12)
x	optimization with additional horizontal stiffness requirement (Table 5.15)

5.1. GENERAL PARAMETERS FOR OPTIMIZATIONS

The implemented values for different parameters used in the performed optimizations are given in [Table 5.2](#). It should be noted that the dimensions and Young's modulus are not representative for the eventual design but don't affect the final topologies as long as the strain energy constraints are scaled accordingly.

The chosen design domain size of 150 by 75 elements was the maximal discretization with reasonable run times (≈ 15 seconds per iteration on an Intel(R) Core(TM) i7-6700HQ processor) for the optimizations with the largest computational expense. For additional info on the run times the reader is referred to [Appendix B.1](#). Symmetry around the vertical axis in the middle of the design domain was enforced. The used relative pad length of 0.2λ meant that, according to [Figure 3.4](#), the maximal deformations for the skew case are 6.25 times larger than for the crest case in reality. For the optimizations however, the applied displacements of the crest

Table 5.2: Assigned values for parameters used in the optimizations

Parameter	Assigned value
# of elements in x ($n_{el,x}$)	150
# of elements in y ($n_{el,y}$)	75
element size	1x1x1 m
relative pad length $l_{pad,rel}$	0.2λ
filter radius (r)	3 m
initial densities (x_0)	$0.2 \frac{\text{kg}}{\text{m}^3}$
Young's modulus (E)	1 Pa
Poisson's ratio (ν)	0.3
g_{scale}	0.01

and skew case (to calculate SE_{skew} and SE_{crest} from the set K_{low}^p) were scaled down and applied such that the maximal applied displacement always was one meter in either positive or negative y-direction (exactly like shown in Figure 4.5). The stiffness of the two cases with respect to each other was thus controlled by the upper bound for the strain energy of the respective load case $SE_{skew,max}$ and $SE_{crest,max}$. This way there was freedom to either consider the fact that the structure experiences larger deformations in the skew case, or to explore the solution space with parameters that don't exactly represent the real proportions. To ensure that material is placed at the bottom a non-design region with the height of one element across the complete lower boundary of the design domain was implemented (see Figure 5.1). The initial design was homogeneous with all elements having the same density x_0 . As for the volume constraint an upper bound of 0.25 was unless stated otherwise. Such a low value was found to reduce the amount of grey area without changing the topology with respect to results with higher bounds on the volume constraint.

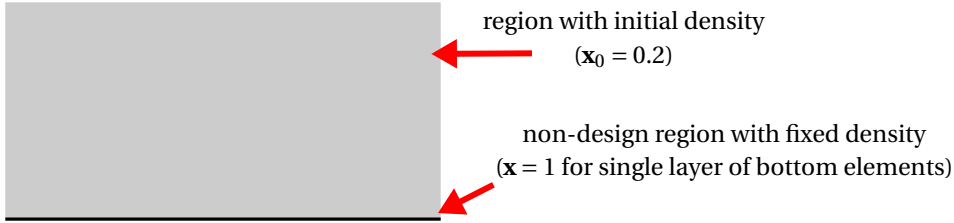


Figure 5.1: Design domain at the start of the optimization

It has to be noted that the optimization results are largely dependent on the initial design, however in order to limit the number of variables that have to be tuned this was not further investigated. In cases where the robust formulation is utilized the robustness value β was increased during the optimization according to the following scheme:

$$\beta_{i+1} = \min(\beta_{max}, 1.03\beta_i) \quad (5.1)$$

Here, i indicates the current iteration count. As an initial value $\beta_0 = 0.5$ was chosen for all optimizations with the robust formulation.

The optimizations without the robust formulation were terminated in case all constraints were satisfied within a tolerance of $1 * 10^{-4}$, the average design variable change with respect to the previous iteration was less than $5 * 10^{-4}$, and the KKT-norm was lower than $5 * 10^{-4}$. In case of the robust formulation the KKT-condition was neglected 100 iterations after the constraints have been satisfied and the average variable change has been below $5 * 10^{-4}$.

5.2. INVESTIGATION OFFSET PARAMETER

To investigate the influence of the offset parameter (introduced in [subsection 4.2.3](#)), a design study is performed where the offset is varied. This is done for the two different objectives (load based and displacement based objective) as shown in the problem formulations below. The corresponding load cases for the objective can be found in [subsection 4.2.2](#) and the ones for the constraints in [subsection 4.2.3](#).

$$\begin{aligned} \min_{\mathbf{x}} \quad & -\frac{1}{SE_{y1}^p} SE_y^p(\mathbf{x}) \\ \text{s.t.} \quad & g_{scale} \left(\frac{SE_{crest}^p(\mathbf{x})}{10^{-4}J} - 1 \right) \leq 0 \\ & \sum_{m=1}^{n_{el}} x_m \leq n_{el} V_{max} \end{aligned} \quad (5.2)$$

$$\begin{aligned} \min_{\mathbf{x}} \quad & \frac{1}{SE_{y1}^f} SE_y^f(\mathbf{x}) \\ \text{s.t.} \quad & g_{scale} \left(\frac{SE_{crest}^p(\mathbf{x})}{5 * 10^{-3}J} \right) \leq 0 \\ & \sum_{m=1}^{n_{el}} x_m \leq n_{el} V_{max} \end{aligned} \quad (5.3)$$

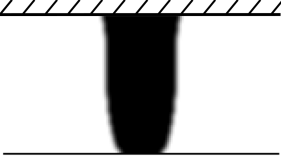
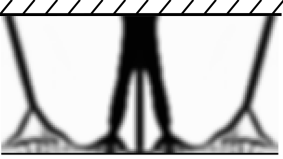
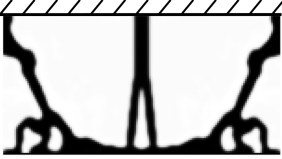
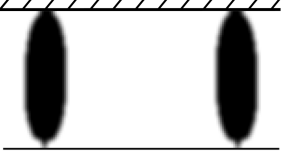

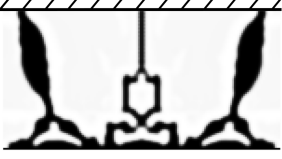
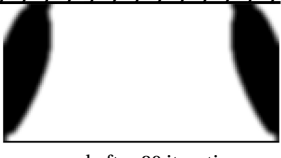

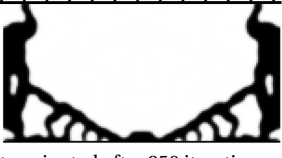
Here, $n_{el} = 150 * 75 = 11250$ and $V_{max} = 0.25$. Note the scaling of the objective with respect to the strain energy of the objective load case in the first iteration $1/SE_{y1}^p$ and $1/SE_{y1}^f$. The constraints are scaled with g_{scale} (provided earlier in [Table 5.2](#)) in order to get the same order of magnitude for the absolute value of objective and constraints. This way we avoid numerical issues which makes the problem easier to handle for the optimizer. The results are shown in the first two columns of [Table 5.3](#).

It is evident that the resulting topologies for the displacement objective (first column in [Table 5.3](#)) have a high stiffness for vertical compression while the bearing pad is easily deformable into a curved shape for the different offsets. The offset parameter influences the positioning of the flexures with respect to the bearing pad. The connections of the flexures to the pad are placed at the points where the prescribed displacements, corresponding to the load case for SE_{crest}^p , are zero (as previously displayed in [Figure 4.5](#)). The results for the force based objective without robust formulation in the second column show that grey areas appear at the locations where the prescribed displacements are largest. At those positions the mechanism is supposed to allow for large deformations while having to support a distributed load which is contradictory and leads to grey areas. The robust formulation is required to get clear black and white results. The problem formulation for the robust version of [Equation 5.3](#) is given below:

$$\begin{aligned} \min_{\mathbf{x}} \quad & \frac{1}{SE_{y1}^f} SE_y^f(\tilde{\mathbf{x}}_e) \\ \text{s.t.} \quad & g_{scale} \left(\frac{SE_{crest}^p(\tilde{\mathbf{x}}_d)}{5 * 10^{-3}J} \right) \leq 0 \\ & \sum_{m=1}^{n_{el}} \tilde{x}_{d,m} \leq n_{el} V_{max}^* \end{aligned} \quad (5.4)$$

Here, $\beta_{max} = 5$ (slope of Heaviside projection) and $\Delta_\eta = 0.1$ (robustness parameter, for more details see [section 4.5](#)). The results for the forced based objective with implementation of the robust formulation are provided in the third column of [Table 5.3](#).

Table 5.3: Design study for offset parameter

offset [m]	TO result displacement based objective	TO result force based objective	TO result force based objective robust formulation
-1	 converged after 43 iterations	 converged after 93 iterations	 terminated after 250 iterations
0	 converged after 180 iterations	 terminated after 500 iterations	 terminated after 250 iterations
1	 converged after 80 iterations	 terminated after 500 iterations	 terminated after 250 iterations

As previously mentioned in [section 3.5](#), the structure should allow the compliant pad to deform into the shape of the counter surface for any position on it. Observation of the results for the displacement based objective displayed in [Table 5.3](#) leads to the conclusion that for an offset of -1 m the structure should easily conform to the counter surface when pressed against it at the trough. However, at the crest of the counter surface this design wouldn't work well because there is nothing that initiates downward movement of the sides of the bearing pad. This leads to a lower contact area which decreases the performance of the bearing. The TO result of the displacement based objective with an offset of 1 m works the opposite and is expected to have large contact area at the crest but a small area at the trough. Similar observations, although less prominent, can be made for the designs with the force based objective. This suggests that we should use an offset somewhere between -1 and 1 m.

For an offset of -0.5 m the area between the 'hinges' is equal to the combined area towards the outsides of the hinges (see [Figure 5.2](#)). This is expected to result in designs without a preference towards either the crest or the trough position and therefore the offset = -0.5 m is chosen for the optimizations.

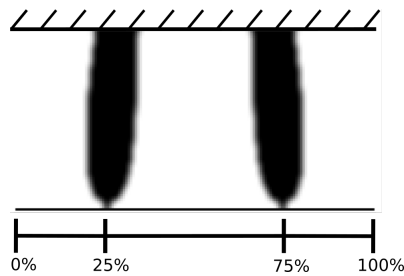


Figure 5.2: Result of optimization with displacement based objective and offset = -0.5 m

5.3. CHOICE OF OBJECTIVE LOAD CASE

[Table 5.3](#) shows that results for the displacement based objective with an offset of 0 or 1 only have two 'connectors' between bearing pad and structure. Those kind of designs are prone to the effect of forming a recess

when a fluid supply is introduced as described earlier in [section 3.4](#) making them again have a preference for the crest of the counter surface. This effect is not as present in the results of the TO's with the force based objective because of the fact that the bearing pad is required to be stiff against a distributed force instead of vertical displacement of the bearing pad as a whole. The distributed force working on the bearing pad in the force based objective is also closer to the real case, where a fluid film pressure will act on it, than the displacement based objective. Therefore, the choice is made to use the force based objective in the optimizations that follow in this report.

5.4. RESULTS WITHOUT REACTION PROFILE REQUIREMENT

In this section the results for optimizations which include one or both constraints for the deformability of the bearing pad are presented for the parameter choices explained in [section 5.1](#), [section 5.2](#), and [section 5.3](#). The influence of the constraint values on the resulting topologies is investigated.

For an offset of -0.5 m the optimization described in the following problem statement is performed.

$$\begin{aligned}
 \min_{\mathbf{x}} \quad & \frac{1}{SE_{y1}^f} SE_y^f(\tilde{\mathbf{x}}_e) \\
 \text{s.t.} \quad & g_{scale} \left(\frac{SE_{crest}^p(\tilde{\mathbf{x}}_d)}{SE_{crest,max}^p} - 1 \right) \leq 0 \\
 & g_{scale} \left(\frac{SE_{skew}^p(\tilde{\mathbf{x}}_d)}{SE_{skew,max}^p} - 1 \right) \leq 0 \\
 & \sum_{m=1}^{n_{el}} \tilde{x}_{d,m} \leq n_{el} V_{max}^*
 \end{aligned} \tag{5.5}$$

At first, some results with either of the constraints implemented (SE_{crest}^p or SE_{skew}^p) are presented in [Table 5.4](#). It is evident that lowering the bound of the constraint leads to designs with lower stiffness. When SE_{max}^p is set too low however, we no longer obtain a clear black and white solution and grey areas appear which can be seen in the result in the fourth row of the crest constraint. Results with $SE_{max}^p = 5.0 \cdot 10^{-3}$ on the other hand are harder to interpret as mechanisms and make more use of distributed compliance. In order to obtain designs that can conveniently interpreted as compliant mechanisms it is decided to stay in the presented range for SE_{max}^p .

Results of optimizations where both constraints have been implemented within the same range of upper bounds $SE_{skew,max}^p$ and $SE_{crest,max}^p$ as used earlier in [Table 5.4](#), are presented in [Table 5.5](#). In the table, results on the same row have equal upper bounds on SE_{skew}^p , and results on the same column have equal upper bounds on SE_{crest}^p . The resulting structures spark curiosity for further investigation. For the most part, the structures can be clearly interpreted as mechanisms with wide regions representing 'semi-rigid' links and narrow regions functioning as 'hinges' in the compliant mechanisms. The results can be divided into three categories depending on the number of connections to the fixed boundary:

1. design \mathbf{G}_{std} , \mathbf{H}_{std} and \mathbf{I}_{std}
2. design \mathbf{B}_{std} and \mathbf{C}_{std}
3. design \mathbf{A}_{std} , \mathbf{D}_{std} , \mathbf{E}_{std} and \mathbf{F}_{std}

Designs within each of those categories show great similarities in their fundamental topology. The predefined bearing pad¹ with a height of one row of elements is thickened either partially or over the whole domain during the optimization. A trend of decreasing bearing pad thickness as well as the presence of narrower and longer 'hinges' for lower values of $SE_{crest,max}^p$ is clearly notable. Closer inspection of design \mathbf{A}_{std} and \mathbf{D}_{std} reveals that some gaps are formed inside the bearing pad in those cases. In the following section the working principle for category 3 designs is briefly explained.

¹The word bearing pad is used for the bottom region in the design which will be in contact with the fluid film/counter surface.

Table 5.4: TO results for optimizations with offset = -0.5 where only one of the two constraints is implemented with varying upper $SE_{skew,max}^p$ or $SE_{crest,max}^p$ (both represented as SE_{max}^p in the table). $V_{max} = 0.25$, offset = -0.5, $\beta_{max} = 5$, and $\Delta\eta = 0.1$. The final value of SE_y^f is provided for each result. All results converged after the indicated number of iterations.


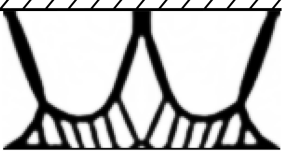
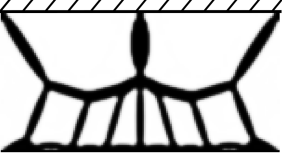

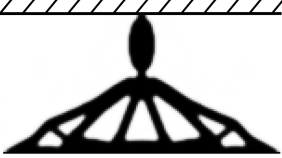
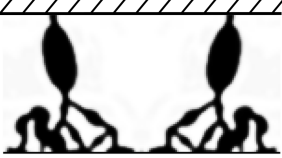
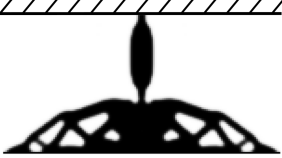

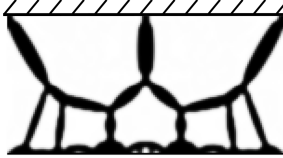

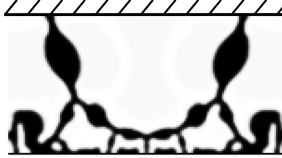
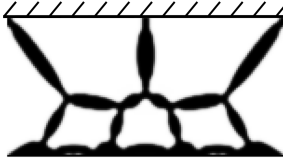
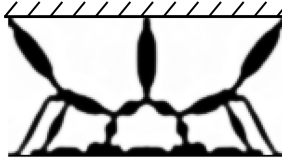
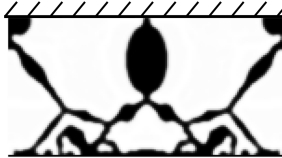
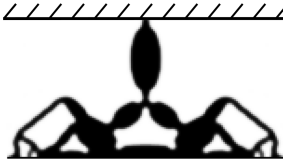
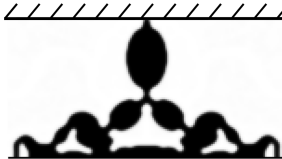
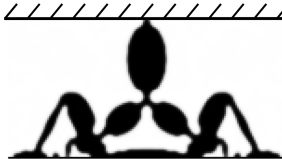
SE_{max}^p [J]	TO result skew constraint only	TO result crest constraint only
$5.0 * 10^{-3}$	 $SE_y^f = 1.10 * 10^5$, 331 iterations	 $SE_y^f = 8.07 * 10^4$, 442 iterations
$2.5 * 10^{-3}$	 $SE_y^f = 3.23 * 10^5$, 280 iterations	 $SE_y^f = 1.08 * 10^5$, 227 iterations
$1.0 * 10^{-3}$	 $SE_y^f = 2.02 * 10^5$, 247 iterations	 $SE_y^f = 2.35 * 10^5$, 228 iterations
$2.0 * 10^{-4}$	 $SE_y^f = 3.19 * 10^5$, 287 iterations	 $SE_y^f = 1.72 * 10^6$, 266 iterations

Table 5.5: TO results for optimizations with various combinations of upper bounds $SE_{skew,max}^p$ and $SE_{crest,max}^p$. $V_{max} = 0.25$, offset = -0.5, $\beta_{max} = 5$, and $\Delta\eta = 0.1$. The final value of SE_y^f is provided for each result. All results converged after the indicated number of iterations

$SE_{skew,max}^p$ [J]	$SE_{crest,max}^p$ [J]		
	$5.0 * 10^{-3}$	$2.5 * 10^{-3}$	$1.0 * 10^{-3}$
$5.0 * 10^{-3}$	 (A _{std}) $SE_y^f = 1.26 * 10^5$, 225 iterations	 (B _{std}) $SE_y^f = 1.61 * 10^5$, 213 iterations	 (C _{std}) $SE_y^f = 3.40 * 10^5$, 328 iterations
$1.0 * 10^{-3}$	 (D _{std}) $SE_y^f = 2.01 * 10^5$, 232 iterations	 (E _{std}) $SE_y^f = 2.77 * 10^5$, 216 iterations	 (F _{std}) $SE_y^f = 5.78 * 10^5$, 338 iterations
$2.0 * 10^{-4}$	 (G _{std}) $SE_y^f = 4.09 * 10^5$, 268 iterations	 (H _{std}) $SE_y^f = 4.74 * 10^5$, 347 iterations	 (I _{std}) $SE_y^f = 7.17 * 10^5$, 453 iterations

5.4.1. WORKING PRINCIPLE OF CATEGORY 3 DESIGNS

The designs with three connections to the boundary share the same fundamental working principle which will be explained on design D_{std} . The design in its scaled-up deformed configuration for the crest, skew, and trough case is shown in Figure 5.3. In Figure 5.3a each of the 'links' in mechanism is assigned a letter-number combination. Imagine the design going from the trough to the crest position. An upward directed force working on the pad below links C2 and C3 (which is what happens when the mechanism is pressed against the crest of the counter surface) causes B1, B2, B3 and B4 to rotate towards a more horizontal position. This in turn initiates rotation of links A1 and A3 into a more upright position and leads to a downward movement of links C1 and C4 which effectively increases the number of contact points with the counter surface. Conversely, an upward directed force acting on links C1 and C4 will cause downward movement of links C2 and C3. This makes sure that the bearing pad is also supported in the middle when pressed against the trough position of the counter surface. Rotation of the bearing pad as a whole in order to deform into the skew position is achieved by rotation of links A1, A2, and A3 in the same direction. This causes upward movement of link C1 and downward movement of link C4.

Because of the symmetry the structure is in a 'locked' state (i.e. an equivalent ideal rigid body model would be infinitely stiff in vertical direction) for the crest and trough position, which enables high load bearing capability. For the skew case, the horizontal reaction component of the reaction force of the counter surface can solely be compensated by link A3. This means that the mechanism is theoretically in a 'locked' state up to the point where link A3 gets into an upright position where it loses the ability to compensate for horizontal stiffness.

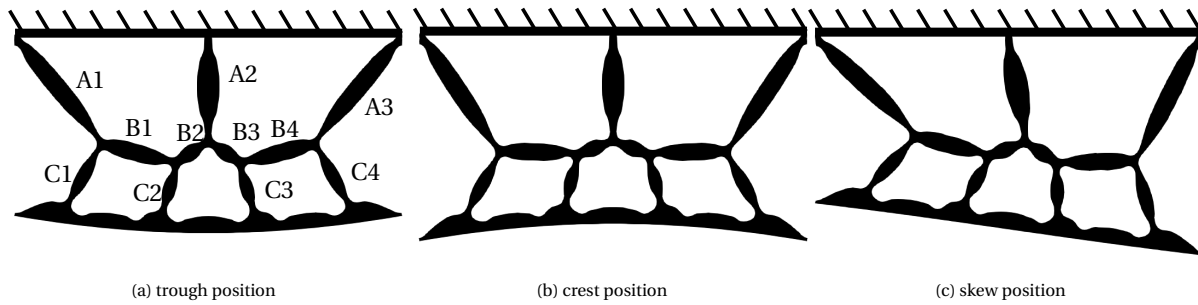


Figure 5.3: Scaled up deformed configurations of design D_{std} for the load cases utilized in the optimizations

5.5. RESULTS WITH INCLUSION OF REACTION PROFILE REQUIREMENTS

As described earlier in section 4.3 there are two possibilities for the implementation of the requirement on the reaction profile. The first approach is based on the principle of pressure profile matching in which a triangular target shape is required for the reaction profile of the structure. This is implemented with a penalty, as previously described in subsection 4.3.1. The results for this approach are presented in subsection 5.5.1. Several modified approaches with the same goal of achieving a triangular reaction profile are presented in subsection 5.5.2. In the second approach the requirement on the shape of the reaction profile is relaxed, and a constraint is used to achieve monotonic decrease of the reaction forces from the middle to the sides of the structure. The results for this approach are provided in subsection 4.3.2.

5.5.1. PRESSURE PROFILE MATCHING PENALTY

The problem statement for implementation of the pressure profile matching penalty (introduced in subsection 4.3.1) is given in Equation 5.6. To determine $P_{rob}(\tilde{x}_e, \tilde{x}_i, \tilde{x}_d)$, the target reaction force profile shown in Figure 5.4 is used. According to [9], this profile is the ideal reaction profile in order to get a fluid film with uniform height over the whole pad length for a flat counter surface.

$$\begin{aligned}
\min_{\mathbf{x}} \quad & \frac{1}{SE_{y1}^f} SE_{y1}^f(\tilde{\mathbf{x}}_e) + P_{rob}(\tilde{\mathbf{x}}_e, \tilde{\mathbf{x}}_i, \tilde{\mathbf{x}}_d) \\
\text{s.t.} \quad & g_{scale} \left(\frac{SE_{crest}^p(\tilde{\mathbf{x}}_d)}{SE_{crest,max}^p} - 1 \right) \leq 0 \\
& g_{scale} \left(\frac{SE_{skew}^p(\tilde{\mathbf{x}}_d)}{SE_{skew,max}^p} - 1 \right) \leq 0 \\
& \sum_{m=1}^{n_{el}} \tilde{x}_{d,m} \leq n_{el} V_{max}^*
\end{aligned} \tag{5.6}$$

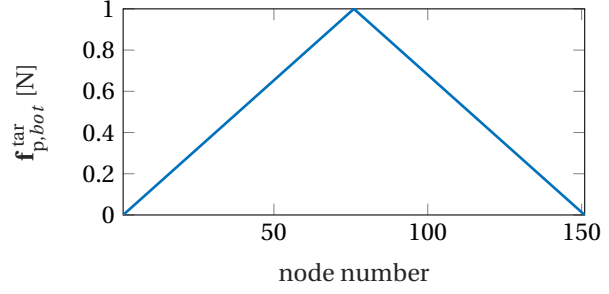
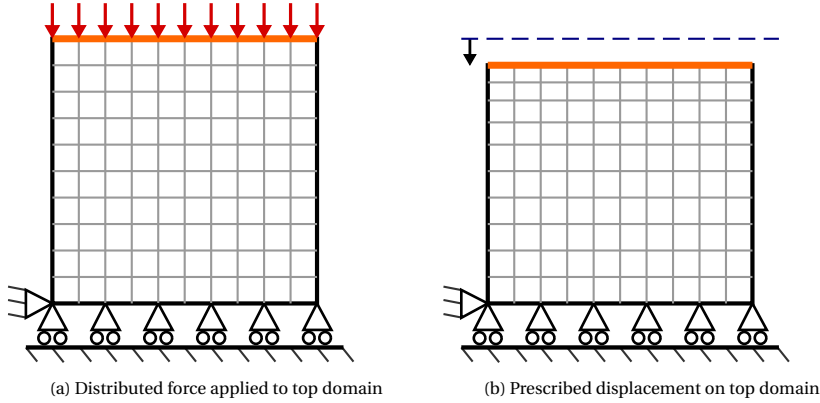


Figure 5.4: Implemented target reaction force profile

ON THE CHOICE OF LOAD CASE FOR REACTION PROFILE DETERMINATION

In Figure 4.6 two possible load cases for the determination of the reaction profile at the bottom surface are given which are provided again in this chapter (Figure 5.5) for convenience. The load case with a prescribed displacement of the top domain (Figure 5.5b, implemented with a downward displacement of 1 meter of the top domain) is closer to the uniform compression scenario used by Nijssen in [9]. The load case with a distributed force acting on the top domain (Figure 5.5a, implemented with a force of 1 Newton on each node at the top domain) represents a case which approximates the uniform compression scenario.

Figure 5.5: Possible load cases for determination of the reaction forces $\mathbf{f}_{p,bot}$ for a design domain and FE-discretization of 10x10 elements

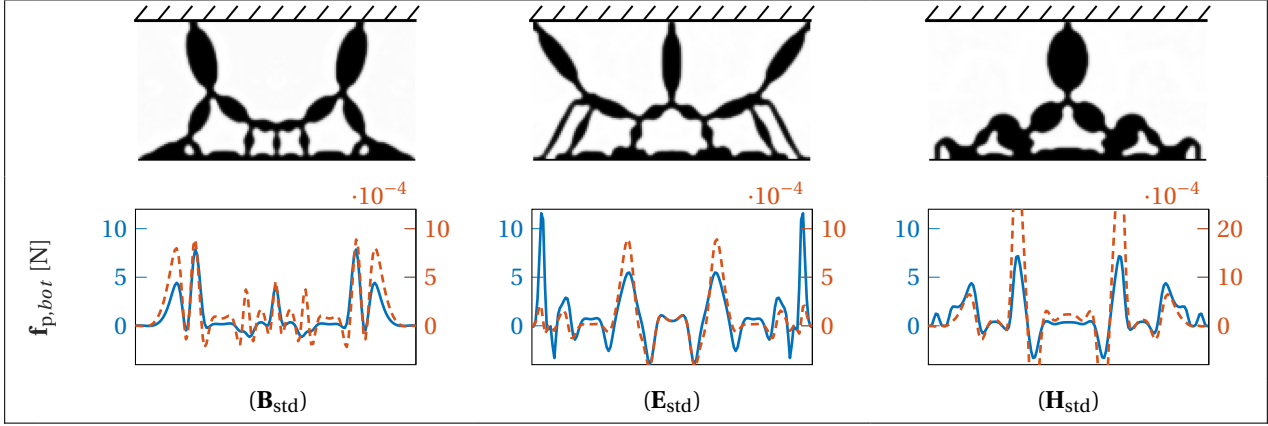
A big advantage of using the load case shown in Figure 5.5a is computational expense. Crucial in that regard is the calculation of λ_f^T for the sensitivities of $\mathbf{f}_{p,bot}$ (Equation 4.37 and Equation 4.38) where the term $\mathbf{K}_{pf} \mathbf{K}_{ff}^{-1}$ has to be calculated once per considered field, per iteration. Since the robust formulation is required it has to be calculated three times per iteration. For the load case with prescribed displacements at the top domain, \mathbf{K}_{pf} has twice the number of rows compared to the case with an applied force acting on the top domain. This means that the prescribed displacement case is twice as expensive computationally.

As a reference the reaction profiles of design \mathbf{B}_{std} , \mathbf{E}_{std} and \mathbf{H}_{std} are determined with both load cases and shown in Table 5.6. The linear FE analysis from the optimizations is used for this purpose. In order to make a clear distinction, reaction profiles which are obtained with the distributed force case are always presented with a blue line, while the reaction profiles obtained with the prescribed displacement case are always presented with an orange line. This holds for the whole report. Furthermore, the reader is informed that the descriptions of the x-axis are omitted in order to improve readability of the tables. The plots for the reaction profiles are always lined up correctly with the design representation above.

The results indicate that reaction profiles are not of triangular shape for results that don't include measures to achieve this in the formulation. Comparison of the profiles obtained with the two different cases shows that there is some agreement between the shapes. At some points however, there are also significant differences. For example, in design \mathbf{E}_{std} the reaction forces of the distributed force load case (blue line) are much larger

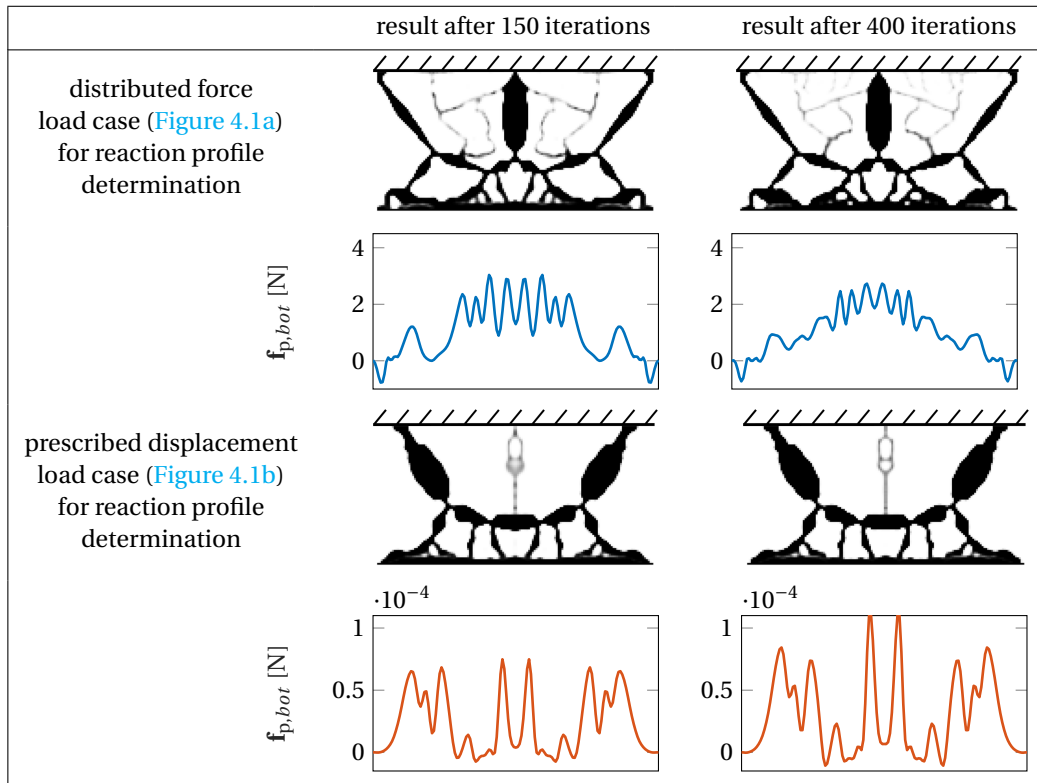
at the sides compared to the reaction forces for the prescribed displacement load case (orange dashed line). Important to mention is that both load cases show negative reaction forces which is something that can't be encountered when evaluating the reaction pressure in a contact study. This is not accounted for in the optimizations.

Table 5.6: Three TO results from Table 5.5 together with their respective reaction profiles for the load case presented in Figure 5.5a (blue line) and the load case presented in Figure 5.5b (orange dashed line)



TO results for the distributed force case are presented in Table 5.8 and the results for the prescribed displacement case in Table 5.9. The optimizations didn't converge according to the criteria given in section 5.1 but showed no significant changes in topology after 150 iterations for both load cases. This can be seen in Table 5.7. Additionally, the convergence history plots for design $E_{r,f}$, given in Figure 5.6, indicate that there is minimal change in objective and constraint values after 150 iterations. Based on these observations it is deemed reasonable to terminate the optimizations after 150 iterations in order to save valuable time.

Table 5.7: TO results + corresponding reaction profile for optimization according to Equation 5.6 with $SE_{crest,max}^p = 2.5 \cdot 10^{-3}$, $SE_{skew,max}^p = 1.0 \cdot 10^{-3}$, $V_{max} = 0.25$, offset = -0.5, $\beta_{max} = 20$ and $\Delta\eta = 0.05$ for 150 and 400 iterations



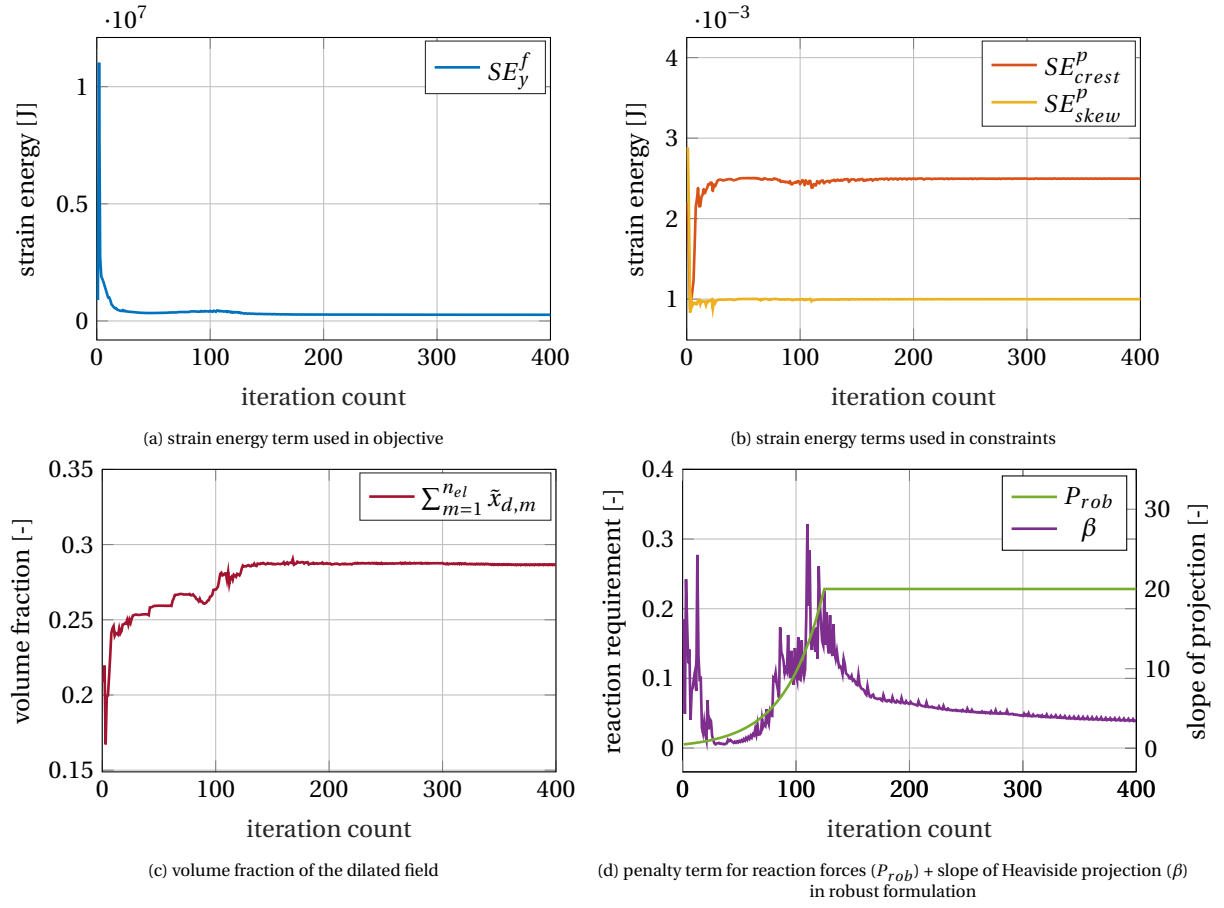
Figure 5.6: Convergence histories for design $\mathbf{E}_{r,f}$

Table 5.8: TO results + corresponding reaction profiles for optimizations where P_{rob} is included (according to Equation 5.6). The load case with applied distributed force (shown in Figure 5.5a) was used for reaction profile determination. $V_{max} = 0.25$, $offset = -0.5$, $\beta_{max} = 20$ and $\Delta\eta = 0.05$. The final values of SE_y^f and P_{rob} are provided as well as the final value of SE_{crest}^p and/or SE_{skew}^p in cases it wasn't equal to its respective upper bound. The optimizations did not converge and were terminated after 150 iterations.

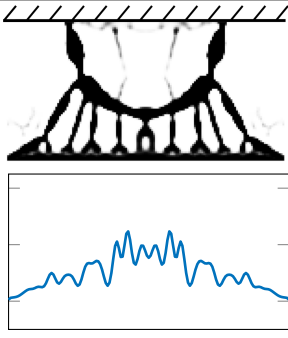
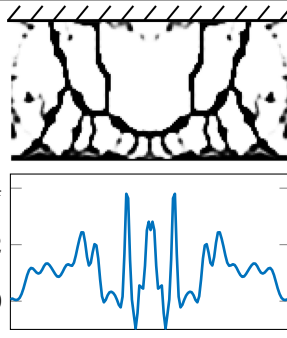
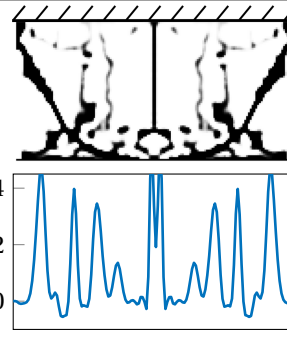
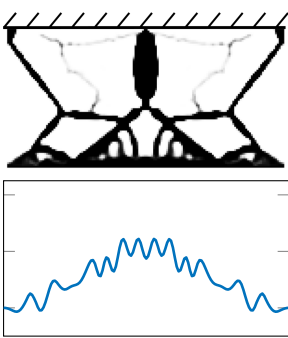
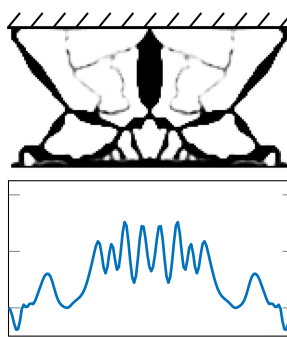
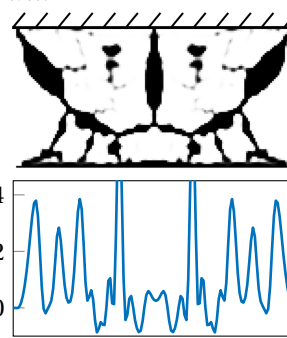
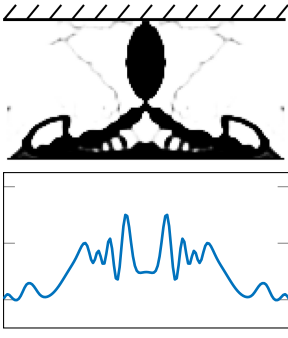
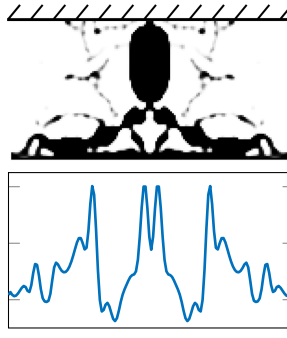
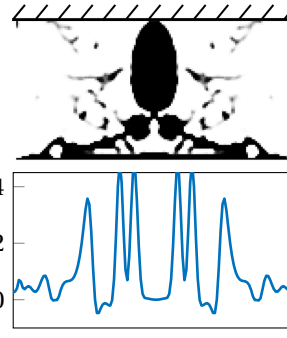
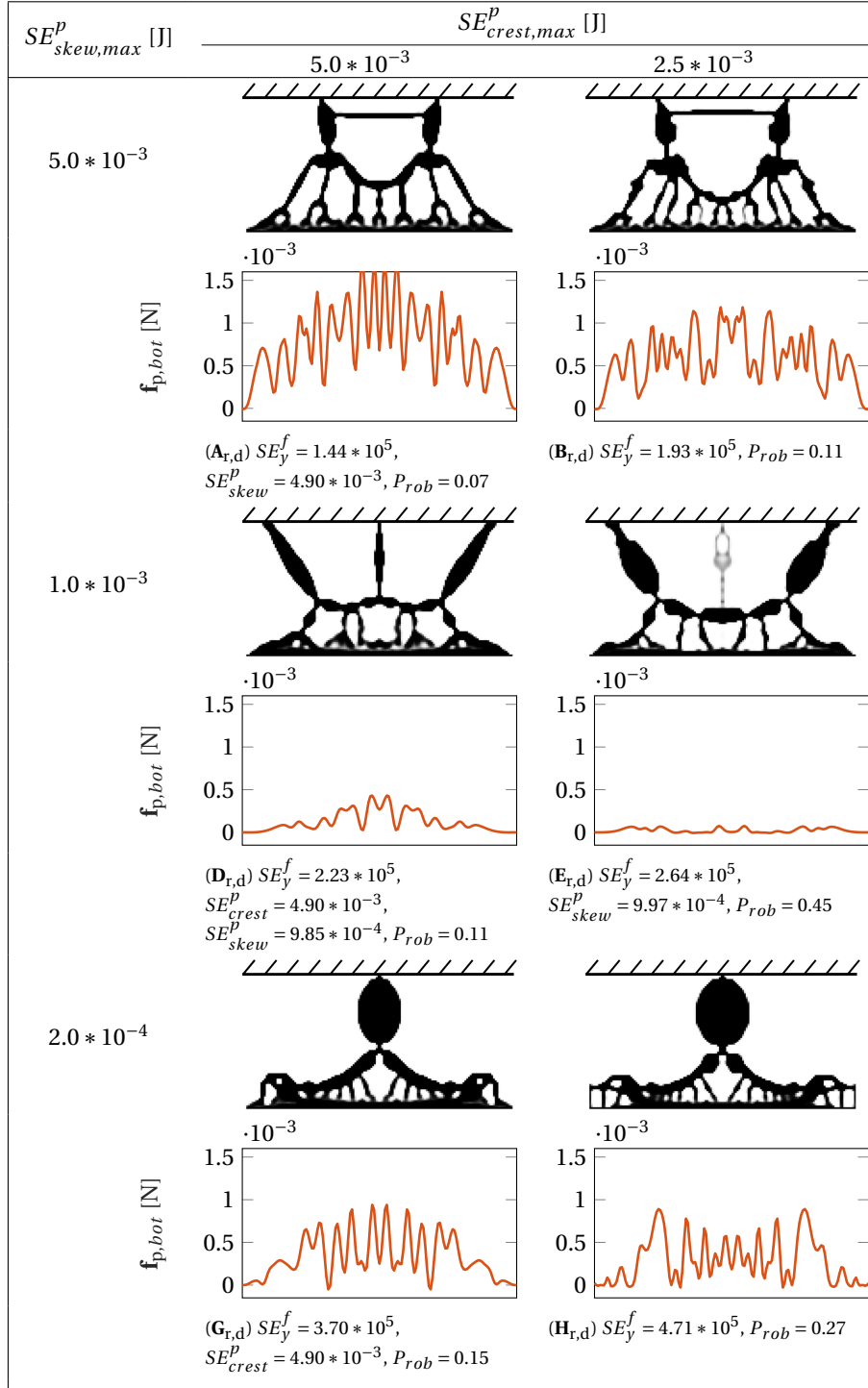
$SE_{skew,max}^p$ [J]	$SE_{crest,max}^p$ [J]		
	$5.0 * 10^{-3}$	$2.5 * 10^{-3}$	$1.0 * 10^{-3}$
$5.0 * 10^{-3}$	 <p>(A_{r,f}) $SE_y^f = 1.29 * 10^5$, $P_{rob} = 0.06$</p>	 <p>(B_{r,f}) $SE_y^f = 2.54 * 10^5$, $P_{rob} = 0.32$</p>	 <p>(C_{r,f}) $SE_y^f = 4.86 * 10^5$, $SE_{crest}^p = 9.96 * 10^{-4}$, $P_{rob} = 0.51$</p>
$1.0 * 10^{-3}$	 <p>(D_{r,f}) $SE_y^f = 2.20 * 10^5$, $SE_{crest}^p = 4.90 * 10^{-3}$, $SE_{skew}^p = 9.98 * 10^{-4}$, $P_{rob} = 0.03$</p>	 <p>(E_{r,f}) $SE_y^f = 2.99 * 10^5$, $SE_{skew}^p = 9.99 * 10^{-4}$, $P_{rob} = 0.12$</p>	 <p>(F_{r,f}) $SE_y^f = 3.64 * 10^5$, $SE_{crest}^p = 9.98 * 10^{-4}$, $SE_{skew}^p = 9.97 * 10^{-4}$, $P_{rob} = 0.68$</p>
$2.0 * 10^{-4}$	 <p>(G_{r,f}) $SE_y^f = 4.15 * 10^5$, $P_{rob} = 0.09$</p>	 <p>(H_{r,f}) $SE_y^f = 5.21 * 10^5$, $P_{rob} = 0.32$</p>	 <p>(I_{r,f}) $SE_y^f = 9.67 * 10^5$, $SE_{crest}^p = 9.93 * 10^{-4}$, $SE_{skew}^p = 1.99 * 10^{-4}$, $P_{rob} = 0.37$</p>

Table 5.9: TO results + corresponding reaction profiles for optimizations where P_{rob} is included (according to Equation 5.6). The load case with a prescribed downward displacement of the top domain (shown in Figure 5.5b) was used for reaction profile determination. $V_{max} = 0.25$, $offset = -0.5$, $\beta_{max} = 20$ and $\Delta\eta = 0.05$. The final values of SE_y^f and P_{rob} are provided as well as the final value of SE_{crest}^p and/or SE_{skew}^p in cases it wasn't equal to its respective upper bound. The optimizations did not converge and were terminated after 150 iterations.



The obtained designs show at most a rough approximation of a triangular shape in their reaction profiles. It is difficult for the optimizer to find clearly defined designs while satisfying the requirement of a triangular reaction profile. This is the case even though the robustness value $\Delta\eta$ is relatively low, which ensures that the difference between the three projected fields in the robust formulation is as small as possible². The large

value for β_{max} , that has been implemented to get clear black and white designs, is not able to get rid of grey areas while also causing artifacts. Those are especially visible in Table 5.8. It stands out that the results in Table 5.9 show significantly less grey area towards the upper side of the design domain. However, the grey areas that are present are often in crucial regions such as in the middle directly above the pad in design $\mathbf{D}_{r,d}$, or the grey 'link' connecting topology and boundary in design $\mathbf{E}_{r,d}$. Optimizations performed with more iterations (up to 250) or higher β_{max} (up to 30) didn't result in designs without this grey 'link'.

In the tables the final value for the implemented reaction penalty P_{rob} is provided. The closer P_{rob} is to zero the better the reaction profile requirement is satisfied. It can be noted that there is a negative correlation between $SE_{crest,max}^p$ and P_{rob} , whereas $SE_{skew,max}^p$ and P_{rob} seem uncorrelated. A stricter limit on SE_{crest}^p basically tells the optimizer to enable upward movement of the middle of the pad more easily. This conflicts with the objective of getting the largest reaction forces at the same position, which is the fundamental problem we seek solutions for.

Something that can be noted is that the optimizer tries to achieve the prescribed reaction profile through distributed compliance and makes a connection to the bearing pad at more instances than before. An interesting strategy, most heavily utilized in design $\mathbf{E}_{r,f}$, $\mathbf{G}_{r,d}$, and $\mathbf{H}_{r,d}$, is the placement of numerous thin members directly above the bearing pad. The members closest to the middle make the largest angle with the bearing pad which decreases for the members placed more towards the sides.

5.5.2. MODIFIED APPROACHES TO IMPROVE SATISFACTION OF THE TRIANGULAR REACTION PROFILE REQUIREMENT

The results presented in subsection 5.5.1 show the difficulty of finding designs with a triangular reaction profile without getting grey area or artifacts. For completeness, this chapter shows TO results for some of the additional attempts that have been made to find structures with a better reaction profile and/or less grey area.

TRIANGULAR SHAPED LOAD PROFILE IN OBJECTIVE

In this attempt the same problem formulation as presented in Equation 5.5. The only difference was the shape of the applied force in the load case for the objective. The standard load case used to obtain $SE_y^f(\tilde{\mathbf{x}}_e)$ is the uniformly distributed load as shown in Figure 4.3a. This load has been changed into a triangular shape with an offset, which is shown in figure Figure 5.7. This way the optimizer should seek designs which are stiffer towards the middle without having to implement an additional penalty. Three results for this approach together with the reaction profile evaluated with the load case from Figure 4.1b are presented in Table 5.10.

The approach works to some extent and the reaction forces are higher in the middle than towards the sides. However, we do not obtain a triangular profile. Comparing the results with designs obtained for the 'standard' optimizations (shown in Table 5.5), great similarities between design \mathbf{E}_{tri} and \mathbf{E}_{std} can be noted. This can provide some inspiration on how the standard designs could be improved to better suit the application. The approach taken by the optimizer to support a larger load in the middle is to place the outer members connected to the fixed boundary closer towards the middle. These members are also placed in a more upright position. Similarly, the two members connected to the middle of the bearing pad are placed closer together and almost vertically instead of under a slight angle. Thickness of the members is also increased towards the middle.

²Note that the lower implemented Δ_η also reduces the minimum feature size with respect to the results from section 5.4 where $\Delta_\eta = 0.1$ was used.

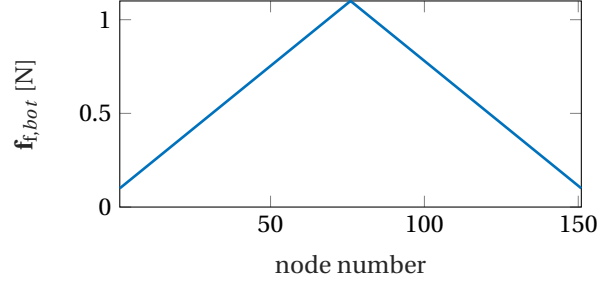


Figure 5.7: Triangular profile with offset for the applied force in the objective load case

Table 5.10: TO results + corresponding reaction profiles (determined with prescribed displacement load case shown in Figure 5.5b). The optimizations follow the problem formulation provided in Equation 5.7 with a triangular shaped force in the objective load case (Figure 5.7). $V_{max} = 0.25$, $offset = -0.5$, $\beta_{max} = 5$ and $\Delta\eta = 0.05$. The final value of the strain energy for the objective load case under the triangle shaped applied force ($SE_{y,tri}^f$) is provided. The optimizations converged after the indicated number of iterations.



$SE_{crest,max}^p$ [J]	$5.0 * 10^{-3}$	$2.5 * 10^{-3}$	$1.0 * 10^{-3}$
$SE_{skew,max}^p$ [J]	$1.0 * 10^{-3}$	$1.0 * 10^{-3}$	$1.0 * 10^{-3}$
<div style="display: flex; justify-content: space-around;"> <div> <p>$(D_{tri}) SE_{y,tri}^f = 3.92 * 10^4, 274$ iterations</p> </div> <div> <p>$(E_{tri}) SE_{y,tri}^f = 4.33 * 10^4, 300$ iterations</p> </div> <div> <p>$(F_{tri}) SE_{y,tri}^f = 6.42 * 10^4, 254$ iterations</p> </div> </div>			

LOW STIFFNESS BEARING PAD

In this approach the non-design region for the bearing pad is altered. Instead of using a single row of elements with fixed densities $\mathbf{x} = 1$, now three rows with fixed densities $\mathbf{x} = 0.13572$ are utilized. Because of the SIMP interpolation this approaches a material with a Young's modulus of $E = 0.13572^3 \approx 2.5 * 10^{-3}$, which is 400 times smaller than the Young's modulus of elements with full density. This ratio could be achieved in practice when using steel for the structural parts and an elastomer for the pad. Note that the Poisson's ratio of the low density elements is still equal to elements in the remainder of the design domain. Two results for an optimization with the modified design domain according to the problem formulation provided in Equation 5.6 are provided in Table 5.11.

The reaction profiles show significant improvement towards a triangular shape. Design $F_{pad,d}$ is the more promising one as it seems to have no grey area apart from the bearing pad. The optimizer places a lot of material directly above the pad which can be interpreted as rigid segments where the regions with little material function as joints. There is also a support placed in the middle with an interesting setup that seems to be self-locking when subjected to a vertical load pointed upwards. The low stiffness pad does however also introduce some uncertainty and the real reaction profile might deviate. Previous results without a low stiffness pad give a more 'honest' picture of the performance of the compliant structure and can always be improved by the addition low stiffness bearing pad in a post-processing stage.

Table 5.11: TO results + corresponding reaction profiles for optimizations (according to Equation 5.6) with a lower stiffness bearing pad. $V_{max} = 0.25$ and offset = -0.5. The final values of SE_y^f and P_{rob} are provided. The final values of SE_{crest}^p and SE_{skew}^p are equal to their respective upper bound. The optimizations were terminated after the indicated number of iterations.

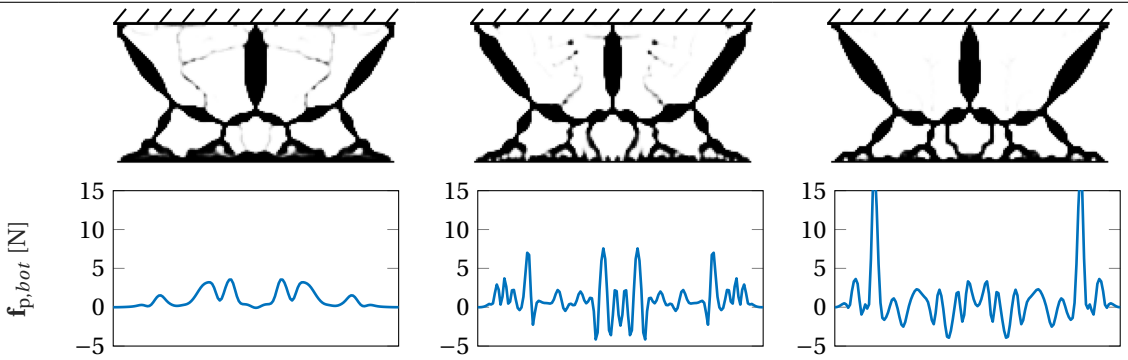
$SE_{crest,max}^p$ [J]	$1.0 * 10^{-3}$	$1.0 * 10^{-3}$
$SE_{skew,max}^p$ [J]	$1.0 * 10^{-3}$	$1.0 * 10^{-3}$
$\beta_{max} \mid \Delta\eta$	20 0.1	25 0.05
<div style="display: flex; justify-content: space-around; align-items: flex-end;"> <div style="text-align: center;">  <p>$f_{p,bot}$ [N]</p> <p>($F_{pad,f}$) $SE_y^f = 8.70 * 10^5$, $P_{rob} = 0.02$, 250 iterations</p> </div> <div style="text-align: center;">  <p>$\cdot 10^{-4}$</p> <p>($F_{pad,d}$) $SE_y^f = 3.05 * 10^5$, $P_{rob} = 0.03$, 160 iterations</p> </div> </div>		

COARSER MESH FOR REACTION PROFILE DETERMINATION

It is possible to relax the requirement of the triangular reaction profile by taking fewer nodes into account when determining the reaction profile. This is done for the problem formulation provided in Equation 5.6, while only using every 2nd, 4th, or 8th node of the reaction profile in order to determine P_{rob} . The results are shown in Table 5.12.

Clearly a coarser mesh leads to a decrease in grey area. At the same time the shape of the reaction profile gets far off the desired triangular shape. This is however not reflected in the respective value of P_{rob} (which actually improves) since not all of the nodes are taken into account. This indicates that the optimizer takes advantage of formulations which seek to provide more freedom. It also shows that there is a tradeoff between grey area and satisfaction of the triangular reaction profile.

Table 5.12: TO results + corresponding reaction profiles (determined with applied load case shown in Figure 5.5a). The optimizations follow the problem formulation provided in Equation 5.6, where P_{rob} is implemented with a coarser mesh on the reaction profile. $V_{max} = 0.25$, offset = -0.5, $\beta_{max} = 20$ and $\Delta\eta = 0.05$. The final value of SE_y^f is provided while the final values of SE_{crest}^p and SE_{skew}^p are equal to their respective upper bound. The optimizations were terminated after 150 iterations

$SE_{crest,max}^p$ [J]	$2.5 * 10^{-3}$	$2.5 * 10^{-3}$	$2.5 * 10^{-3}$
$SE_{skew,max}^p$ [J]	$1.0 * 10^{-3}$	$1.0 * 10^{-3}$	$1.0 * 10^{-3}$
# of nodes for reaction profile	every 2nd	every 4th	every 8th
 <div style="display: flex; justify-content: space-around; margin-top: 10px;"> <div style="text-align: center;"> <p>(E_{r,f2}) $SE_y^f = 2.41 * 10^5$, $P_{rob,2} = 0.25$</p> </div> <div style="text-align: center;"> <p>(E_{r,f4}) $SE_y^f = 2.47 * 10^4$, $P_{rob,4} = 0.11$</p> </div> <div style="text-align: center;"> <p>(E_{r,f8}) $SE_y^f = 2.13 * 10^4$, $P_{rob,8} = 0.004$</p> </div> </div>			

5.5.3. SOFT REACTION FORCE CONSTRAINT

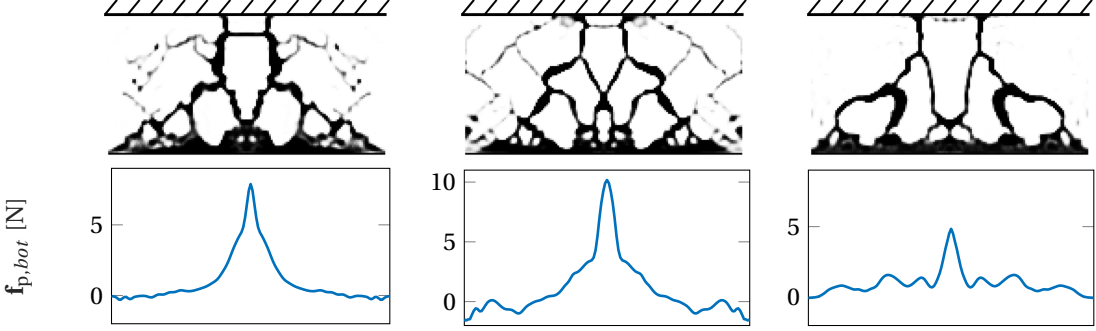
The current section presents results for the second approach with a reaction profile requirement.

For implementation of the soft reaction force constraint (as introduced in subsection 4.3.2) the problem formulation is provided in Equation 5.7. The results for this approach with an acceptable amount of grey area are shown in Table 5.13. Note that a slightly different offset of -0.45 m was used in those cases. This altered the positions of the 'hinges' (section 5.2) by 1.2 % of the pad length in relation to an offset of -0.5 m which is negligible.

$$\begin{aligned}
 \min_{\mathbf{x}} \quad & \frac{1}{SE_{y1}^f} SE_y^f(\tilde{\mathbf{x}}_e) \\
 \text{s.t.} \quad & g_{scale} \left(\frac{SE_{crest}^p(\tilde{\mathbf{x}}_d)}{SE_{crest,max}^p} - 1 \right) \leq 0 \\
 & g_{scale} \left(\frac{SE_{skew}^p(\tilde{\mathbf{x}}_d)}{SE_{skew,max}^p} - 1 \right) \leq 0 \\
 & C_{rob}(\tilde{\mathbf{x}}_e, \tilde{\mathbf{x}}_i, \tilde{\mathbf{x}}_d) \leq u_b \\
 & \sum_{m=1}^{n_{el}} \tilde{x}_{d,m} \leq n_{el} V_{max}^*
 \end{aligned} \tag{5.7}$$

In order to obtain clear designs a large value for β_{max} had to be used which also introduces some artifacts. Grey area is however still present in the members directly above the bearing pad for design J and L. The typical reaction profile quickly decreases in the middle of the structure while not changing much towards the sides. The structures differ significantly from the results for the shape morphing penalty (Table 5.8) and the optimizer relies even heavier on distributed compliance in the designs in its attempt to satisfy the reaction force constraint. It can be seen on design L that tuning V_{max} can lead to a design with less artifacts and less grey area above the structure. The downside is that this is also producing thinner and longer members. All of the structures obtained with the current approach have a higher final objective value for SE_y^f compared to the results previously presented. This means that the stiffness in y-direction is poor which can also be concluded by visual inspection of the designs because of the thin curved members.

Table 5.13: TO results + corresponding reaction profiles for optimizations where C_{rob} is included (according to Equation 5.7). offset = -0.5, $\beta_{max} = 25$ and $\Delta\eta = 0.05$. The final values of SE_y^f as well as SE_{crest}^p and SE_{skew}^p are provided. The optimizations have been terminated after the indicated number of iterations.

$SE_{crest,max}^p$ [J]	$5.0 * 10^{-3}$	$2.5 * 10^{-3}$	$2.5 * 10^{-3}$
$SE_{skew,max}^p$ [J]	$5.0 * 10^{-3}$	$2.5 * 10^{-3}$	$2.5 * 10^{-3}$
$V_{max} u_b$	0.25 0.05	0.25 0.05	0.23 0.03
			
<p>(J) $SE_y^f = 1.61 * 10^6$, $SE_{crest}^p = 4.00 * 10^{-3}$, $SE_{skew}^p = 2.80 * 10^{-3}$, $C_{rob} = 7.7$, 250 iterations</p> <p>(K) $SE_y^f = 2.14 * 10^6$, $SE_{crest}^p = 2.10 * 10^{-3}$, $SE_{skew}^p = 1.78 * 10^{-3}$, $C_{rob} = 8.4$, 500 iterations</p> <p>(L) $SE_y^f = 2.30 * 10^6$, $SE_{crest}^p = 4.19 * 10^{-3}$, $SE_{skew}^p = 2.42 * 10^{-3}$, $C_{rob} = 12.6$, 250 iterations</p>			

From the large number of iterations as well as the high value for β_{max} it is evident that the setup with the 'soft' reaction force constraint is harder to solve than the first approach in subsection 5.5.1. Using lower values than $2.5 * 10^{-3}$ for either $SE_{crest,max}^p$ or $SE_{skew,max}^p$ was found to produce even more artifacts.

Most of the results with the penalty to get a triangular reaction profile presented in Table 5.8 and Table 5.9 show a 'dip' in their reaction profile exactly in the middle. This is caused by the constraint on SE_{crest}^p which requires the structure to enable large deformations in the middle as previously pointed out in subsection 5.5.1. For the formulation using the P_{rob} , the optimizer can go for solutions with a 'dip' in reaction force in the middle if this allows the shape to be improved at the other positions such that P_{rob} is decreased. When C_{rob} is implemented, the middle node is strictly required to be largest which makes this approach harder to solve even though a specific shape is not prescribed. This again displays the fundamental difficulty of the design problem which is to enable large deformations for the middle of the bearing pad where it is also supposed to provide high reaction forces in case the pad is in full contact a counter surface.

5.6. RESULTS WITH ADDITIONAL X-STIFFNESS REQUIREMENT

In this last section of the current chapter, a requirement for the x-stiffness is added to the objective and results are shown for optimizations with and without an implemented requirement on the reaction profile.

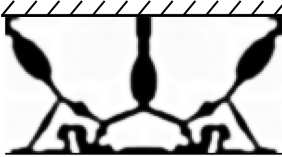



The objective can be extended in order to achieve higher stiffness in horizontal direction. This is expected to improve performance of the designs in the skew part of the counter surface. For the implementation, the term SE_x^f (related to the load case presented in Figure 4.3a) is added to the objectives of Equation 5.5 (without

P_{rob}) and Equation 5.6 (which includes P_{rob}).

$$\begin{aligned}
 \min_{\mathbf{x}} \quad & \frac{1}{SE_{y1}^f} SE_y^f(\tilde{\mathbf{x}}_e) + \gamma_x \frac{1}{SE_{x1}^f} SE_x^f(\tilde{\mathbf{x}}_e) \left(+ P_{rob}(\tilde{\mathbf{x}}_e, \tilde{\mathbf{x}}_i, \tilde{\mathbf{x}}_d) \right) \\
 \text{s.t.} \quad & g_{scale} \left(\frac{SE_{crest}^p(\tilde{\mathbf{x}}_d)}{SE_{crest,max}^p} - 1 \right) \leq 0 \\
 & g_{scale} \left(\frac{SE_{skew}^p(\tilde{\mathbf{x}}_d)}{SE_{skew,max}^p} - 1 \right) \leq 0 \\
 & \sum_{m=1}^{n_{el}} \tilde{x}_{d,m} \leq n_{el} V_{max}^*
 \end{aligned} \tag{5.8}$$

Here, γ_x is a scale factor which controls the relative importance of the SE_x^f -term in relation to the SE_y^f -term. P_{rob} can be included to get results with a reaction profile requirement which is why it's put between brackets. Table 5.14 shows four TO results without P_{rob} and differing values of γ_x while all other parameters are kept constant. It can be seen that the final value of SE_x^f decreases as γ_x gets larger which means that the structure

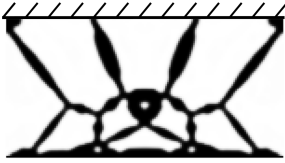
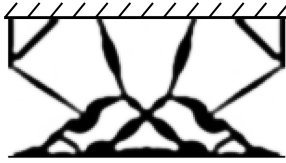
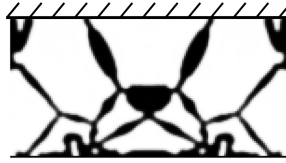
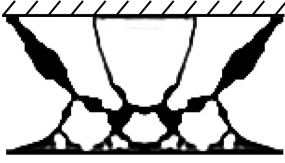

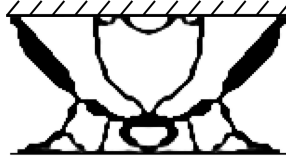
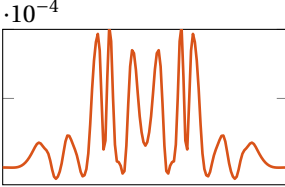
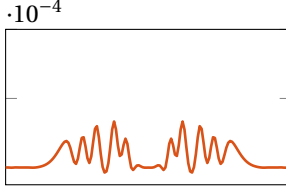
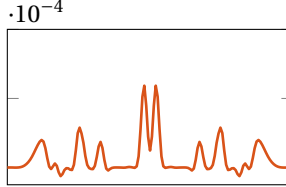
Table 5.14: TO results with additional term for horizontal stiffness objective where $SE_{skew,max}^p = 1.0 * 10^{-3}$, $SE_{crest,max}^p = 1.0 * 10^{-3}$, $V_{max} = 0.25$, offset = -0.45, $\beta_{max} = 5$ and $\Delta\eta = 0.1$. The importance of horizontal stiffness is adjusted through γ_x . The final values of SE_y^f , SE_x^f as well as SE_{crest}^p and SE_{skew}^p are provided. All results converged after the indicated number of iterations.

γ_x			
0.1	0.25	0.5	1
			
$SE_y^f = 5.87 * 10^5$, $SE_x^f = 5.58 * 10^6$, 292 iterations	$SE_y^f = 7.83 * 10^5$, $SE_x^f = 2.99 * 10^6$, 260 iterations	$SE_y^f = 7.47 * 10^5$, $SE_x^f = 1.58 * 10^6$, 262 iterations	$SE_y^f = 7.55 * 10^5$, $SE_x^f = 1.24 * 10^6$, 289 iterations

is getting stiffer against horizontal actuation for larger γ_x . For $\gamma_x = 0.1$ the TO result still shows significant similarities to design \mathbf{F}_{std} from Table 5.5. The choice is made to use $\gamma_x = 0.5$ for further optimizations since it offers the largest gain in horizontal stiffness for the lowest decrease in vertical stiffness. Table 5.15 shows the results of optimizations with the same settings and parameters as used for design \mathbf{E}_{std} , \mathbf{F}_{std} and \mathbf{H}_{std} where the horizontal stiffness term is added in the objective as shown in Equation 5.8. In the same table the results with additional reaction force penalty (P_{rob}) are displayed. Note that result \mathbf{F}_{std} is the same as the third result from the left in Table 5.14.

The optimizations result in clear designs with minimal amounts of grey area. Design \mathbf{E}_x and \mathbf{F}_x share similarities to the standard results \mathbf{E}_{std} and \mathbf{F}_{std} (Table 5.5) especially towards the sides. The most prominent difference can be observed in the middle of the structures. In design \mathbf{E}_x and \mathbf{F}_x two links under a slight angle make a connection to the fixed boundary instead of a single straight one as in design \mathbf{E}_{std} and \mathbf{F}_{std} . This means that there is an additional link to support the horizontal load experienced in the skew position as previously discussed in subsection 5.4.1. Comparison of design \mathbf{H}_x with \mathbf{H}_{std} shows that the implementation of an additional x-stiffness requirement can yield a completely different type of structure for low bounds on SE_{crest}^p .

Table 5.15: TO results for optimizations according to Equation 5.8 with some combinations of upper bounds $SE_{skew,max}^P$ and $SE_{crest,max}^P$. $V_{max} = 0.25$. The final values of SE_y^f and P_{rob} are provided.

$SE_{crest,max}^P$ [J]	$2.5 * 10^{-3}$	$2.5 * 10^{-3}$	$1.0 * 10^{-3}$
$SE_{skew,max}^P$ [J]	$1.0 * 10^{-3}$	$2.0 * 10^{-4}$	$1.0 * 10^{-3}$
results without P_{rob} where: $\beta_{max} = 5$ $\Delta_\eta = 0.1$			
	(E_x) $SE_y^f = 3.50 * 10^5$, $SE_x^f = 1.05 * 10^6$, offset = -0.5, converged after 243 iterations	(H_x) $SE_y^f = 5.91 * 10^5$, $SE_x^f = 1.75 * 10^6$, offset = -0.5, converged after 372 iterations	(F_x) $SE_y^f = 7.47 * 10^5$, $SE_x^f = 1.58 * 10^6$, offset = -0.45, converged after 262 iterations
results with P_{rob} where: $\beta_{max} = 25$ $\Delta_\eta = 0.05$			
$f_{p,bot}$ [N]			
	($E_{x,r,d}$) $SE_y^f = 3.85 * 10^5$, $SE_x^f = 1.42 * 10^6$, $P_{rob} = 0.57$, offset = -0.5, terminated after 170 iterations	($H_{x,r,d}$) $SE_y^f = 4.97 * 10^5$, $SE_x^f = 1.30 * 10^6$, $P_{rob} = 0.33$, offset = -0.5, terminated after 160 iterations	($F_{x,r,d}$) $SE_y^f = 4.76 * 10^5$, $SE_x^f = 1.93 * 10^6$, $P_{rob} = 0.46$, offset = -0.5, terminated after 160 iterations

6 EVALUATION OF DESIGNS

In the previous chapter, results of the performed TO's were presented for different configurations of the problem. Although some interesting observations can be made by looking at the designs we can not yet draw quantitative conclusions on their performance. [section 3.5](#) provided a list of requirements for the structures to be generated. After performing the TO's, where further simplifications (see [subsection 4.2.1](#)) have been made, it will be checked in the current chapter if and how well the requirements are satisfied. In [section 6.1](#) it is further described how the designs are evaluated using a contact study in COMSOL. In [section 6.2](#) the results are presented and discussed for a selection of the designs presented in [chapter 5](#). Additionally, the approach to simplify the contact pressure with a roller constraint during the optimizations is evaluated in [section 6.3](#).

6.1. DEVELOPMENT OF THE EVALUATION MODEL

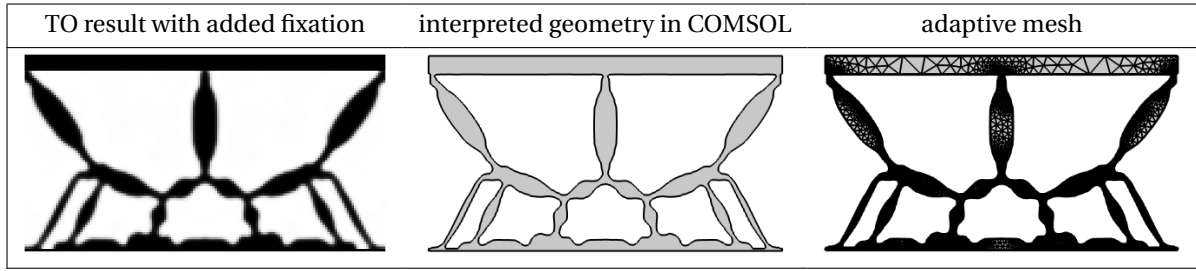
In [section 3.5](#) the three requirements for the intermediate structure between bearing pad and top domain have been listed. A good and realistic way of measuring the performance for these requirements is to perform a contact study where the structure is pushed against the counter surface at different positions. Investigation of the contact pressure reveals if the structure enables sufficient deformation of the bearing pad into the shape of the counter surface when pushed against it (requirement 1). Next to that, the stiffness in vertical direction between top domain and bearing pad, which is sought to be large, can be determined (requirement 2). Finally, the contact pressure profile can be evaluated for a flat counter surface in order to check if the bearing is expected to have a predisposition towards a convex or concave counter surface [9] (requirement 3).

In the following subsections it is described in more detail how the evaluations are performed. First the resulting designs are post processed and imported into COMSOL Multiphysics® to get a geometry which is usable for the FEA ([subsection 6.1.1](#)). After selection of the material ([subsection 6.1.2](#)), the maximum amplitude of the counter surface before yielding occurs is determined ([Table 6.1.4](#)). The resulting value of the maximal amplitude is used for the counter surface in the contact study ([subsection 6.1.3](#)).

6.1.1. POST-PROCESSING OF TO RESULTS

The outcomes of the TO's are density distributions within the design domain consisting of quadrilateral elements. Here, void regions have a very low density (see [subsection 2.2.1](#)). Additionally, all designs have elements with intermediate densities on the boundaries between structural (full density) and void elements. The results where reaction profile requirements have been implemented also show artifacts which have to be dealt with. To evaluate the performance of the designs in a more realistic model compared to the FE simulations performed during the optimizations, the results are post processed. As a result we obtain a clear topology representing the design for the contact study in COMSOL. This is illustrated in [Table 6.1](#) for design E_{std} . In a first step the image file of the TO result is edited and a rectangle drawn at the top of the design in order to get a fixation for the structure. Afterwards the "Image to curve" add-on in COMSOL is used to create a contour based on the black and white TO result after it has been filtered with a Gaussian filter. By adding the fixation before using "Image to curve", a smooth transition between design and fixture is obtained automatically. This way we don't have to manually add fillets in order to avoid stress concentrations in those areas. The number of nodes for the bottom boundary (provided in [Table C.1](#)) is checked in order to ensure that the contact interface is meshed with sufficient accuracy. Additional details on the setup of the model can be found in [Appendix C](#).

Table 6.1: Illustration of post processing steps of the TO results (result E in this case)



6.1.2. MATERIAL SELECTION FOR EVALUATIONS

In the desired practical application for the hydrostatic bearing (DOT piston pump introduced in [chapter 1](#)) the sinusoidal counter surface has a relatively large amplitude with respect to the available space for the bearing. This means we want to get as much deformability out of the compliant structure as possible. For this reason, it was determined that the best candidate materials for the structure should have a high yield strength (σ_{yield}) together with a low Young's modulus (E). This can also be expressed as a desire for maximization of the ratio: $\frac{\sigma_{yield}}{E}$. A search in Ansys Granta EduPack for materials with Young's modulus above 450 MPa (in order to avoid too soft materials) with a large value for the aforementioned ratio was combined with consultation of data-sheet for purchasable materials. This resulted in the selection of materials given in [Table 6.2](#) where also the Poisson's ratio (ν) is provided. The best metal and the best polymer found are given.

Table 6.2: Selected materials and their properties

Material	E [MPa]	σ_{yield} [MPa]	$\frac{\sigma_{yield}}{E}$	ν
Stanyl TW363 PA46-I [36]	600	45	$7.50 * 10^{-2}$	0.4
Titanium grade 19 [37]	102 000	1105	$1.08 * 10^{-2}$	0.34

6.1.3. CONTACT MODEL IN COMSOL

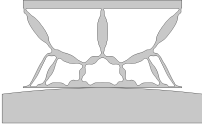
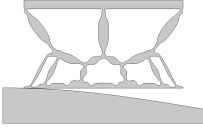
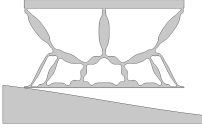
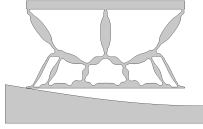
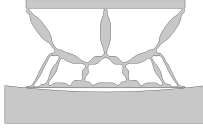
For the contact study a second separate solid representing a section of the counter surface is created below the design. The top boundary of this surface consists of a parametric curve which is represented by a function in the form of:

$$\alpha * \sin\left(2\pi \frac{l_{pad,rel}}{\lambda w_d} x + \text{shift}_x\right) + \text{shift}_y \quad (6.1)$$

where, α specifies the amplitude of the sinusoidal counter surface in meters, $l_{pad,rel}$ is the relative pad length as specified in [Table 5.2](#), w_d is the width assigned to the design in the simulation and x refers to the horizontal position in the coordinate system of the geometry. Variation of the parameter shift_x enables the solid to represent the counter surface at different positions within one wavelength. The parameter shift_y is chosen such that the bottom boundary of the design is sufficiently close to the top boundary of the counter surface. This is required for the assumption of initial contact between design and counter surface to hold. The design together with the additional solid for the counter surface is shown for five positions on the counter surface in [Table 6.3](#). It can be seen that the three most extreme positions at the crest, trough, and skew part, as well as two intermediate positions are considered. For each of those positions a stationary contact study is performed.

The contact pair in COMSOL is created with the top side of the counter surface being the source and the boundary at the bottom of the design being the destination boundary (see [Figure 6.1](#)). A fixed domain constraint is applied to the solid of the counter surface while a displacement in negative y-direction is prescribed for the top boundary of the design. Displacement in x-direction of the same boundary is prescribed to be zero. The Augmented Lagrangian method is utilized in order to satisfy the non-penetration condition between the solids. In the stationary study an auxiliary sweep over the negative y-displacement of the upper boundary

Table 6.3: Geometry of design \mathbf{E}_{std} together with counter surface at 5 positions on the counter surface. In this case $\alpha = 30$ mm

$\frac{1}{2}\pi$	$\frac{3}{4}\pi$	shift_x π	$\frac{5}{4}\pi$	$\frac{3}{2}\pi$
				
crest		skew		trough

of the fixture is performed. The analysis is terminated when the maximal Von Mises stress (σ_{\max}) in the design has passed the yield strength of the material. In all performed simulations geometric nonlinearity is considered.

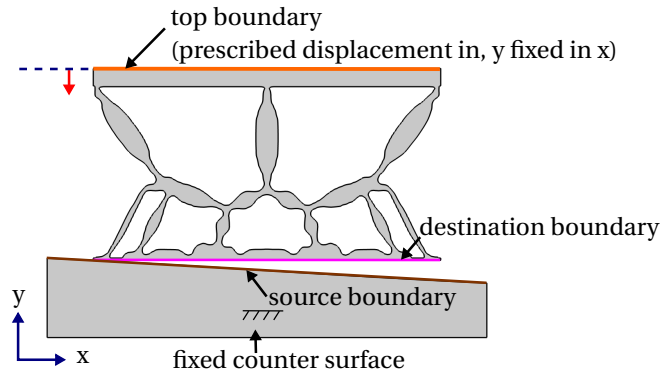


Figure 6.1: Boundary conditions for the contact model in COMSOL

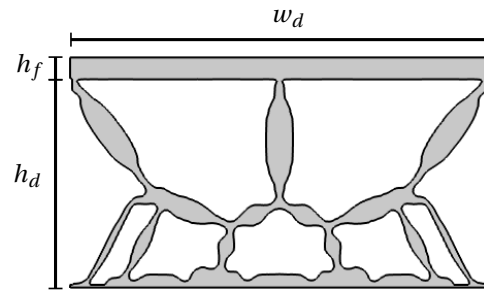
6.1.4. CHOICE OF PARAMETERS FOR EVALUATION MODEL

The dimensions used for the COMSOL evaluation model are listed in Table 6.4. The chosen width of the design w_d is similar to the diameter of a cam-roller (300 mm) utilized for the model of a large-scale piston pump in a recent publication [5]. The thickness t is chosen to be 20 % of w_d . In the auxiliary sweep the prescribed y-displacement of the top domain has a starting value between 0.1 mm and 0.5 mm and is increased in steps between 0.15 mm and 0.78 mm. The utilized value depends on the positioning above the counter surface (determined by shift_x) as well as the specific design.

The remainder of this section treats the choice of amplitude of the counter surface in the contact model. This directly affects which designs can be evaluated, which is also discussed. Finally, some details about the finite element mesh at the contact interface are provided.

Table 6.4: Dimensions used in the evaluation model

Parameter	Assigned value
design width (w_d)	226.0 mm
design height (h_d)	113.0 mm
fixture height (h_f)	11.0 mm
thickness (t)	45.2 mm

Figure 6.2: Clarification of nomenclature for the dimensions using design \mathbf{E}_{std}

MAXIMUM AMPLITUDE FOR THE COUNTER SURFACE

In order to get an idea on how large the amplitude α can be made without getting plastic deformation, a standard FE analysis is used to do an investigation on design E_{std} before performing the contact studies. The displacement for the upper boundary of the fixture is prescribed to be zero. The bottom boundary of the design is subjected to prescribed y-displacements which correspond to the skew part of the counter surface (see Figure 6.4a). The displacements in x-direction are not prescribed and thus free.

To determine an appropriate mesh size the deformations of the load case explained above are evaluated for a fixed amplitude of $\alpha = 14$ mm while the element size for the physics-controlled mesh (consisting of triangular elements) is varied. The corresponding value for σ_{max} together with the mesh size is provided in Table 6.5. Based on the results it can be argued that the 'normal' element size provides sufficient accuracy for a reasonable number of elements. As we are still in the investigation phase to determine the parameters and not yet have to solve the more expensive contact studies we use the 'finer' element size for the analyses described in the remainder of this subsection. The amplitude for the counter surface is incrementally increased in 10 steps. In Table 6.3 σ_{max} is plotted against the amplitude of the counter surface for the materials Titanium and PA46-I.

Table 6.5: Mesh convergence study for the load case shown in Figure 6.4a with $\alpha = 14$ mm and material PA46-I

Element size ²	# of elements	σ_{max} [MPa]
extremely coarse	651	23.912
extra coarse	1027	24.526
coarser	3083	32.265
coarse	10363	39.714
normal	36663	43.652
fine	36703	43.666
finer	54233	43.462
extra fine	69059	43.462
extremely fine	170615	43.462

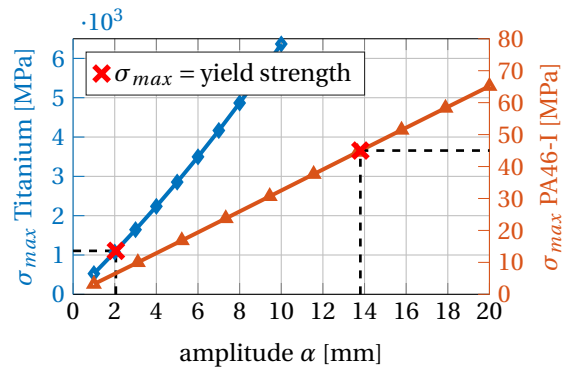


Figure 6.3: Maximal von Mises stress (σ_{max}) plotted against amplitude (α) of the counter surface for design E_{std} subjected to the load case displayed in Figure 6.4a

It appears that titanium starts yielding at an amplitude of 2 mm which is around 2 % of the height of the design. For PA46-I yielding occurs at an amplitude of 14 mm which is around 13 % of the height of the design. One of the reasons to generate compliant mechanisms was the potential of handling larger amplitudes of the counter surface with respect to the bearing with functionally graded material developed by Nijssen [9]. The functionally graded bearing could handle amplitudes up to 1/100th of the height of the design. In this work we want to push things further and investigate how hydrostatic bearings behave for larger amplitude counter surfaces. Therefore the choice is made to use PA46-I as specified in Table 6.2 for further analyses. The use of a polymer does have its limit in practice like fatigue as well as the dependence of the yield strength on the strain rate and temperature. The current work neglects those which will provide insight into the theoretical limits of the obtained designs for the application.

A study of determining the maximum amplitude of the counter surface based on the skew and crest deformations (with an offset of -0.5 m see Figure 6.4b) with the same boundary conditions as for the material selection is performed. In all cases the applied material is PA46-I. The designs for this study are selected such that the range of implemented strain energy bounds ($SE_{\text{crest,max}}^p$ and $SE_{\text{crest,max}}^p$) is covered as good as possible. By including the results from different TO formulations, we get an idea of how those affect the behavior of the structures. The outcomes are presented in Table 6.6³.

²as configured in the options for the utilized Physics-Controlled Mesh within COMSOL Multiphysics®

³Three additional results are provided in Table D.1

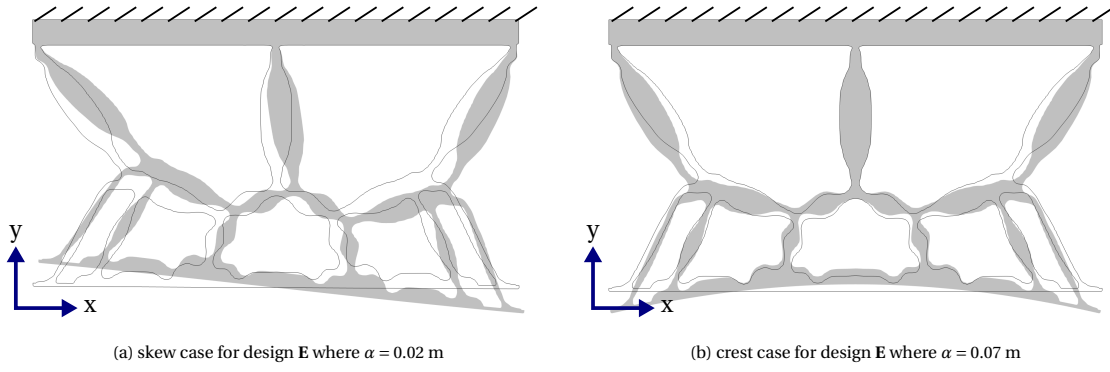
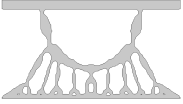

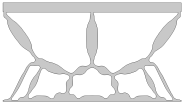
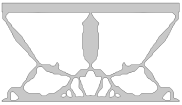
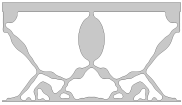

Figure 6.4: Illustration of load cases used to check max α before yielding occurs

Table 6.6: Maximum amplitude for different TO results based on the skew and crest deformation case shown in Figure 6.4

$SE_{skew,max}^p$	$SE_{crest,max}^p$			
	$5.0 * 10^{-3}$	$2.5 * 10^{-3}$		$1.0 * 10^{-3}$
$5.0 * 10^{-3}$				
	A_{r,f}	B_{std}		
α_{max} crest [mm]	24.4	50.0		
α_{max} skew [mm]	4.5	7.8		
$1.0 * 10^{-3}$				
		E_{std}	E_{r,f}	F_{std}
α_{max} crest [mm]		59.6	26.8	87.9
α_{max} skew [mm]		13.8	17.5	16.1
$2.0 * 10^{-4}$				
		H_{std}		
α_{max} crest [mm]		56.4		
α_{max} skew [mm]		32.5		

The results of this study already provide some insights into the behavior of the structures. The maximum amplitude for the crest deformations (α_{max} crest) is similar for results **B_{std}**, **E_{std}** and **H_{std}**. This is in line with the expectations as those have an equal constraint on the strain energy for the crest deformation case (SE_{crest}^p). For the same results, the maximum amplitude for the skew deformation (α_{max} skew) shows a negative correlation with SE_{skew}^p which is again in line with the expectations. Comparing results **E_{std}** and **E_{r,f}** we see that the requirement for the reaction force profile leads to a significant decrease in deformability for the crest case while it is increased for the skew case. On the contrary, inclusion of horizontal stiffness in the objective (when comparing **F_{std}** and **F_x**) doesn't seem to significantly affect the deformability for both cases.

Based on the values of α_{max} skew in Table 6.6 the choice is made to use an amplitude of 11.3 mm for the counter surface in the evaluations which is 10 % of the height of the designs in the evaluation model. This way the structure will be subjected to comparably large deformations and geometric nonlinear effects will also be captured in the analyses. Designs with a value for α_{max} skew lower than 11.3 mm are not evaluated with the same contact study as they are expected to yield before their bottom surface can fully conform to the counter surface. Looking at the values of α_{max} skew for design **A_{r,f}** and **B_{std}** this seems to exclude designs from optimizations where $SE_{skew,max}^p = 5.0 * 10^{-3}$ has been used. All of those designs are indicated with the

letter **A**, **B** or **C**.

CHOICE OF DESIGNS TO BE EVALUATED

Due to the computational expense of the contact studies a narrow selection in the designs to be evaluated has to be made. Design E_{std} is chosen as a starting point and compared to F_{std} and H_{std} to gain insight in how $SE_{crest,max}^p$ and $SE_{skew,max}^p$ affect the performance. The effect of horizontal stiffness on the performance is investigated by consideration of design F_x and H_x . In order to check performance of a design where P_{rob} was used in the formulation design $E_{r,d}$ is also selected. It showed a relatively good satisfaction of the triangular reaction profile without too much grey area in the middle of the design where its effects are thought to be most significant (see Table 5.8). Design **K** is also chosen since it was the most promising result of the soft reaction constraint approach (Table 5.13).

MESH SIZE OF DESIGN MODELS AND MESHING OF THE COUNTER SURFACE

For the contact studies the 'normal' element size is selected for the physics-controlled mesh. Based on the convergence study provided in Table 6.5 this mesh size is expected to deliver sufficient accuracy while not using an excessive number of elements. Note that since the physics-controlled mesh is an automated routine the number of elements will differ between the designs.

As we deal with a curved source boundary for the contact it is important that it is meshed with sufficient accuracy. Therefore, an element size of 1 mm is prescribed for the counter surface. Because the source boundary is rigid there is no need to take the element size of the counter surface relative to the element size at the bottom of the design into account [38]. Figure 6.5 illustrates the utilized mesh for design E_{std} for part of the design and counter surface.

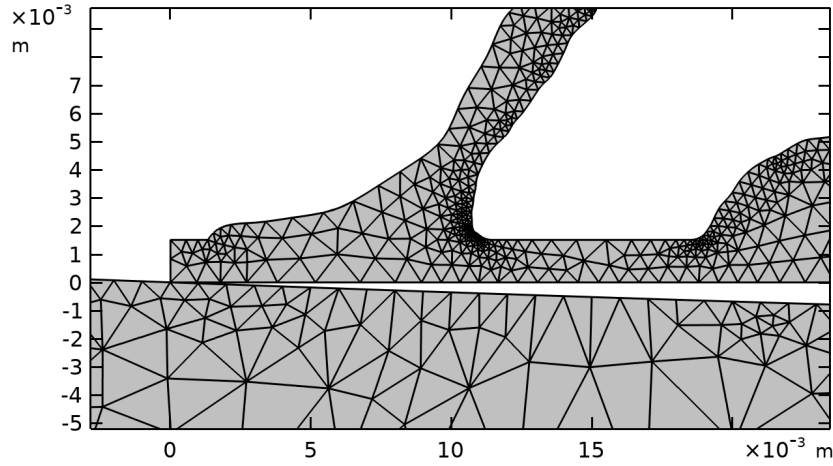


Figure 6.5: Zoomed in illustration of the normal sized physics-controlled mesh for design **E**

6.2. RESULTS OF CONTACT STUDIES

In Figure 6.6 the deformed configuration after the final step of the auxiliary sweep in all 5 positions is given for design E_{std} . For all other designs which have been evaluated a similar figure can be found in Appendix D.2.

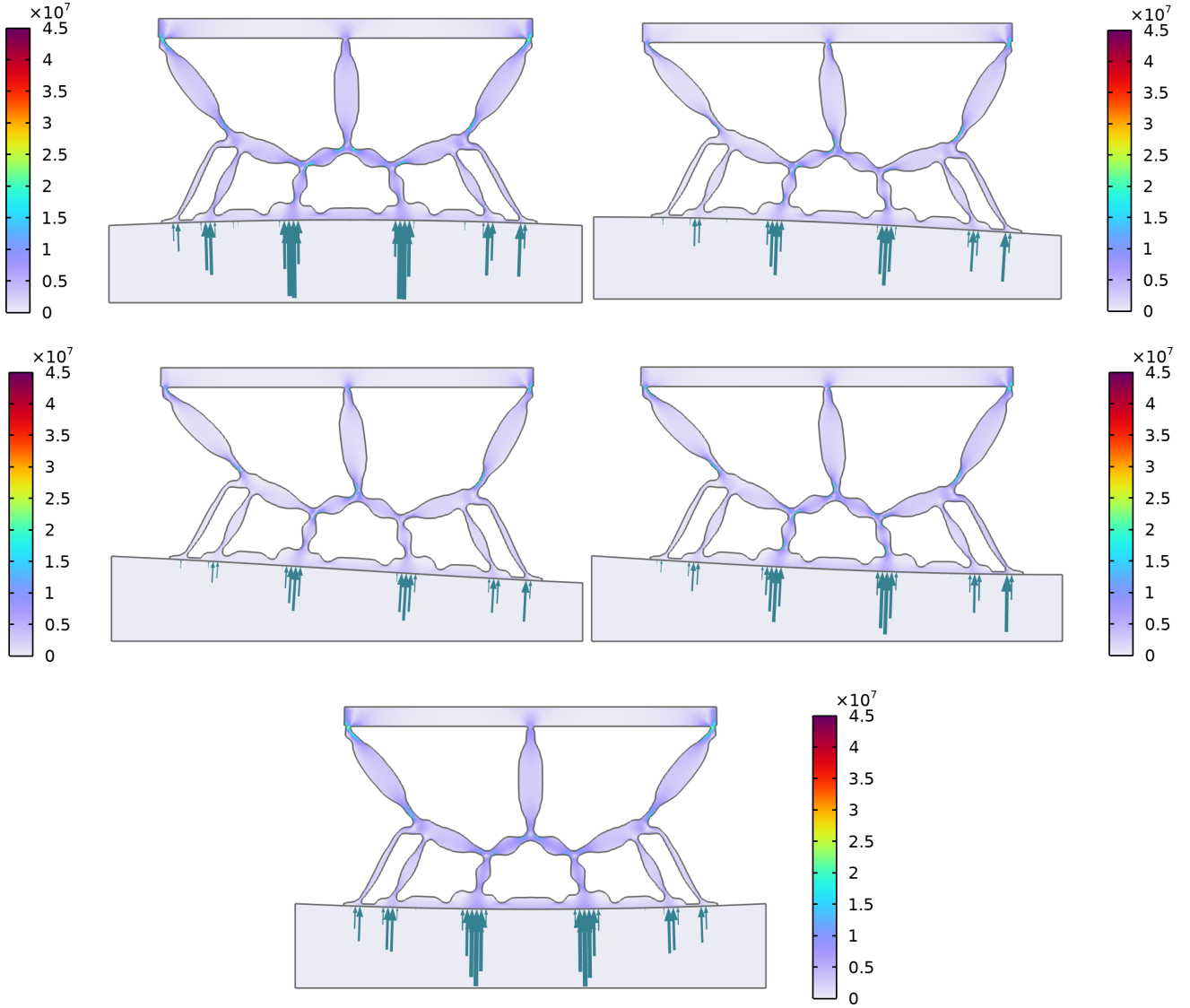


Figure 6.6: Unscaled deformed configuration of the final step for design E_{std} at all evaluated positions above the counter surface. The Von Mises stress in [Pa] is also visualized. The size of the blue arrows is proportional to the contact pressure. However, note that different scaling is applied across various positions

From the contact studies the y-component of the total reaction force for the counter surface is extracted at each step and plotted against the y-displacement of the top domain in [Figure 6.9](#). This load is equal to the required load to bring the top domain to the prescribed vertical displacement. Note that the slope of the curves represents the stiffness of the mechanism in vertical direction. Supplementary plots providing the stiffness based on the numerical gradients of the data from [Figure 6.9](#) are provided in [Figure D.8](#). In [Figure 6.9](#) it is additionally indicated at which point σ_{max} gets equal to the yield strength of 45 MPa. The point where the effective contact area gets to 90 % of the width of the bearing pad is also marked. This way the maximum load which can be put on top of the fixture as well as the load required to get 90 % effective contact area can be derived from the same plot. The corresponding values are additionally provided in [Table D.2](#). Separate plots for the effective contact area can be found in [Figure 6.10](#).

In the remainder of this section the method to determine the maximum load is explained in [subsection 6.2.1](#) followed by an explanation of how the effective contact area is obtained ([subsection 6.2.2](#)). An indication of the usable load range for the different designs is provided in [subsection 6.2.3](#) and the section concludes with the plots for the reaction forces, effective contact area and maximum gap height.

6.2.1. DETERMINING THE MAXIMUM LOAD

As stated before, the auxiliary sweep of the contact studies is automatically terminated as soon as the maximum von Mises stress in the domain of the design has passed the yield strength of 45 MPa. An evaluation of the maximum von Mises stress in the domain of the design is performed for each step in the contact study and plotted against the y-displacement of the top domain as shown for design E_{std} in Figure 6.7. From this plot the y-displacement for which yielding occurs is approximated by determining the value corresponding to $\sigma_{max} = 45$ MPa. The approximated maximum vertical load on the structure is equal to the reaction force for the y-displacement determined with the σ_{max} plot. This load is marked in Figure 6.9 for each respective position on the counter surface.

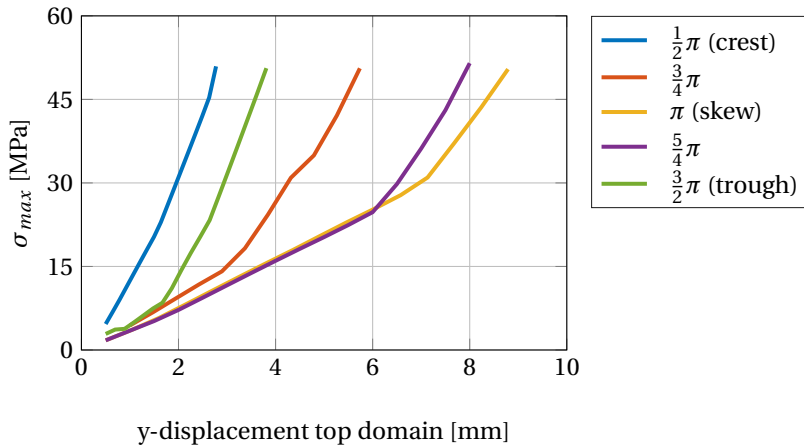


Figure 6.7: Maximum von Mises stress plotted against the y-displacement for the contact studies of design E

6.2.2. DETERMINING THE EFFECTIVE CONTACT AREA

As mentioned in section 6.1 we want to determine if the structures enable sufficient deformation of the bearing pad into the shape of the counter surface. To define what actually is sufficient we have to go back to the use case of the designs as hydrostatic bearings. From an investigation of the deformed configuration of the bearing pad in Figure 6.8a it can be seen that some gaps are formed even under the maximum load. Note that in the real application a fluid film will be present between bearing pad and counter surface. As long as gaps are enclosed by points where contact is made the fluid is expected to fill up those gaps and increase the fluid film height up to the point where the elastic forces in the bearing pad form an equilibrium with the pressure inside the fluid film. Only if the bearing pad loses contact at the edges, the usable area of the bearing is decreased. Therefore, we define the effective contact area to be the distance between the most outward contact points. The contact pressure data is used in order to determine the position of the first and last node where the contact pressure is nonzero, as shown in Figure 6.8b⁴. The distance between those contact points is defined as the effective contact area ($A_{c,eff}$) and determined at each instance of the contact studies. For the plots, this measure is divided by the length of the bearing pad (w_d). It should be noted that this way of determining the effective contact area results in the fact that for the trough position $A_{c,eff}$ will always be maximal initially since both outer edges of the bearing pad are in contact with the counter surface in that particular case. The plots for the effective contact area are provided in Figure 6.10.

If the size of the gaps is getting too large this can imply that the fluid film gets turbulent leading to unpredictable behavior of the bearing since the assumptions for the Reynolds equation⁵ does no longer hold. In order to get some more insight, the maximum gap size (G_{max}) is also determined for all instances in the contact studies where the measure $A_{c,eff}/w_d$ is greater than 0.5. The corresponding plots are provided in Figure 6.11.

⁴Note that the arc length of the bearing pad is on the x-axis and therefore a straight line in this plot represents the effective contact area.

⁵The 1D Reynolds equation is usually used to model the pressure and film height in full film lubricated bearings. It can be used under the assumption of laminar flow.

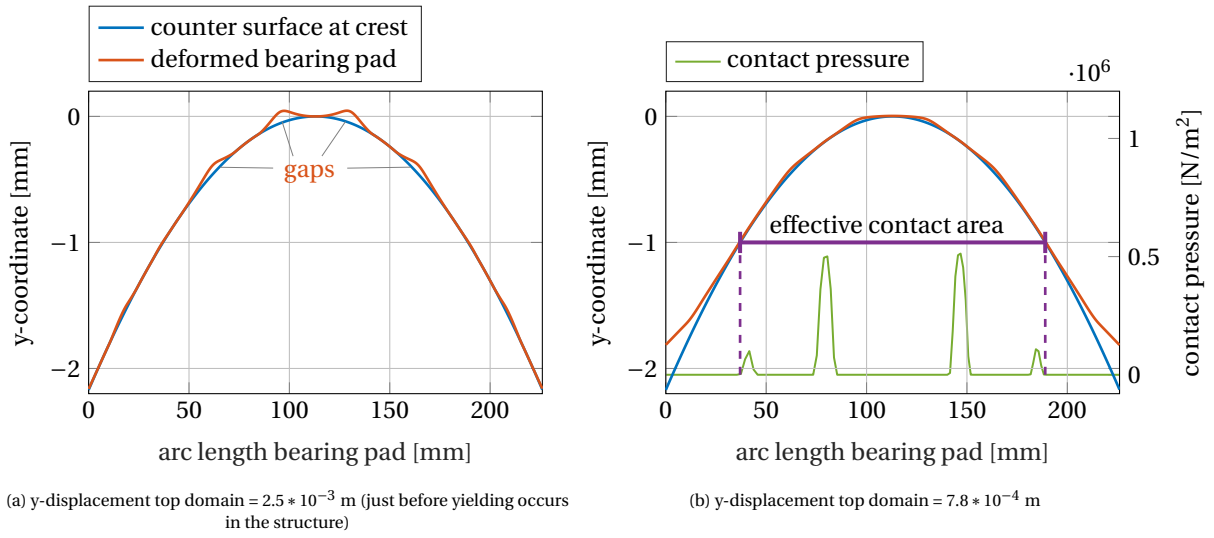


Figure 6.8: Deformations of the bearing pad for design E from a contact study at the crest position. Two different instances for the y-displacement of the top domain in the auxiliary sweep are shown. Additionally, the contact pressure at the same instance is displayed in the right subfigure in order to show how the effective contact area is determined.

6.2.3. USABLE LOAD RANGE FOR THE EVALUATED DESIGNS

Based on Figure 6.9 and Table D.2 a load range for which the evaluated designs are expected to be usable can be determined. To achieve this, we determine the minimum load at which yielding occurs (F_{max}) for each mechanism. It should be noted that a second check must be performed in order to ensure that the mechanism provides sufficient stiffness for the case which determines F_{max} . The corresponding y-stiffness values can be found in Figure D.8. Additionally, the maximum load required to get to 90 % contact area (F_{min}) is identified. Division of the loads by the contact area of the bearing pad ($w_d \cdot t = 10.2 \cdot 10^{-3} \text{ m}^2$) yields the minimum inlet pressure ($p_{in,min}$) and maximum outlet pressure ($p_{out,max}$) for a pump utilizing the designs. This is provided in Table 6.7 for design E_{std} , $E_{r,f}$, F_{std} , F_x and H_x . Please note that this is done solely to provide an indication/upper bound of how applicable current designs are with the chosen material PA46-I. If the designs are to be utilized in a real application, it is unfeasible to use them up to their yield strength. Additional factors like fatigue and nonlinear behavior of the material will have to be accounted for.

Table 6.7: Estimation of operating range of different designs if applied in a piston pump and used up to their yield strength.

Design	F_{max} [kN]	y-stiffness at F_{max} [kN/m]	F_{min} [kN]	$p_{in,min}$ [bar]	$p_{out,max}$ [bar]
E_{std}	0.85	1.94	$1.45 \cdot 10^3$	0.84	1.89
$E_{r,f}$	1.18	2.59	$1.15 \cdot 10^3$	1.15	2.53
F_{std}	1.38	2.20	$1.37 \cdot 10^3$	1.35	2.15
F_x	1.58	3.05	$1.66 \cdot 10^3$	1.55	2.99
H_x	3.49	4.64	$1.04 \cdot 10^3$	3.41	4.54

6.2.4. REACTION FORCE PLOTS

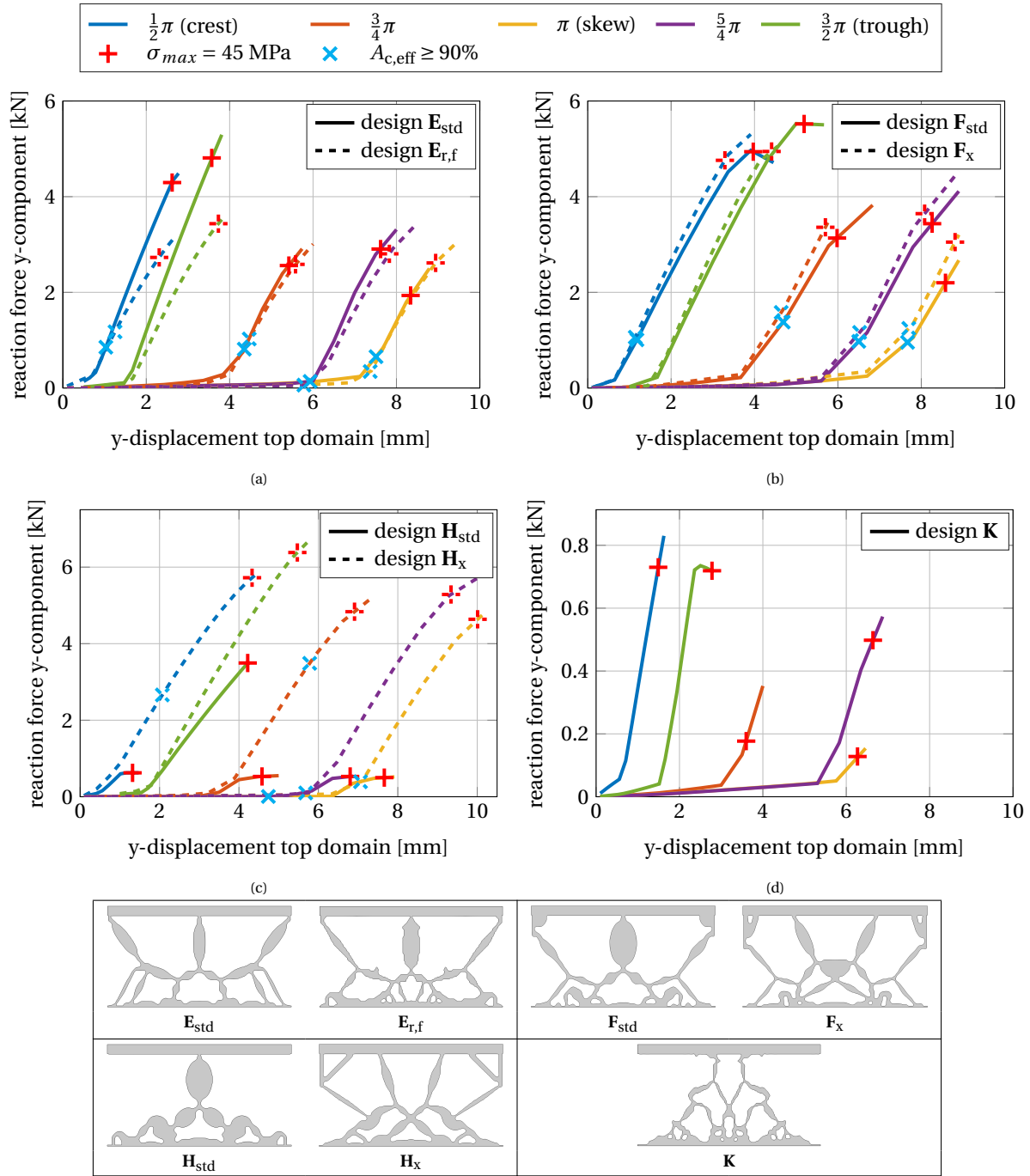


Figure 6.9: y-component of the reaction force of the counter surface during the contact studies versus the absolute prescribed y-displacement of the top domain. The loads where σ_{max} gets equal to the yield strength as well as the loads required to achieve 90% contact area (in relation to the width of the bearing pad w_d) are marked.

6.2.5. CONTACT AREA PLOTS

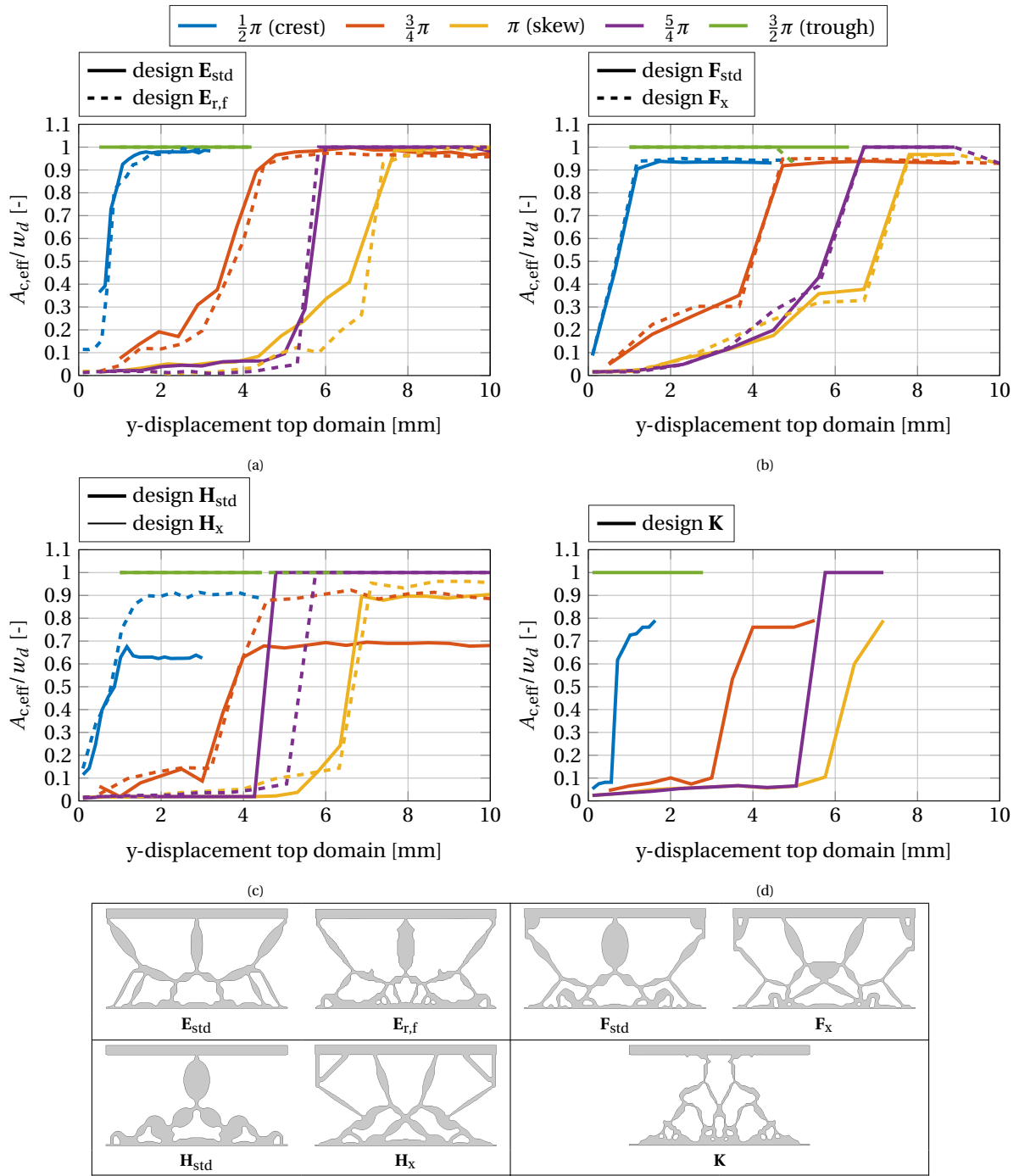


Figure 6.10: Effective contact area $A_{c,eff}$ relative to pad length w_d during the contact studies versus the absolute prescribed y-displacement of the top domain

6.2.6. MAX GAP PLOTS

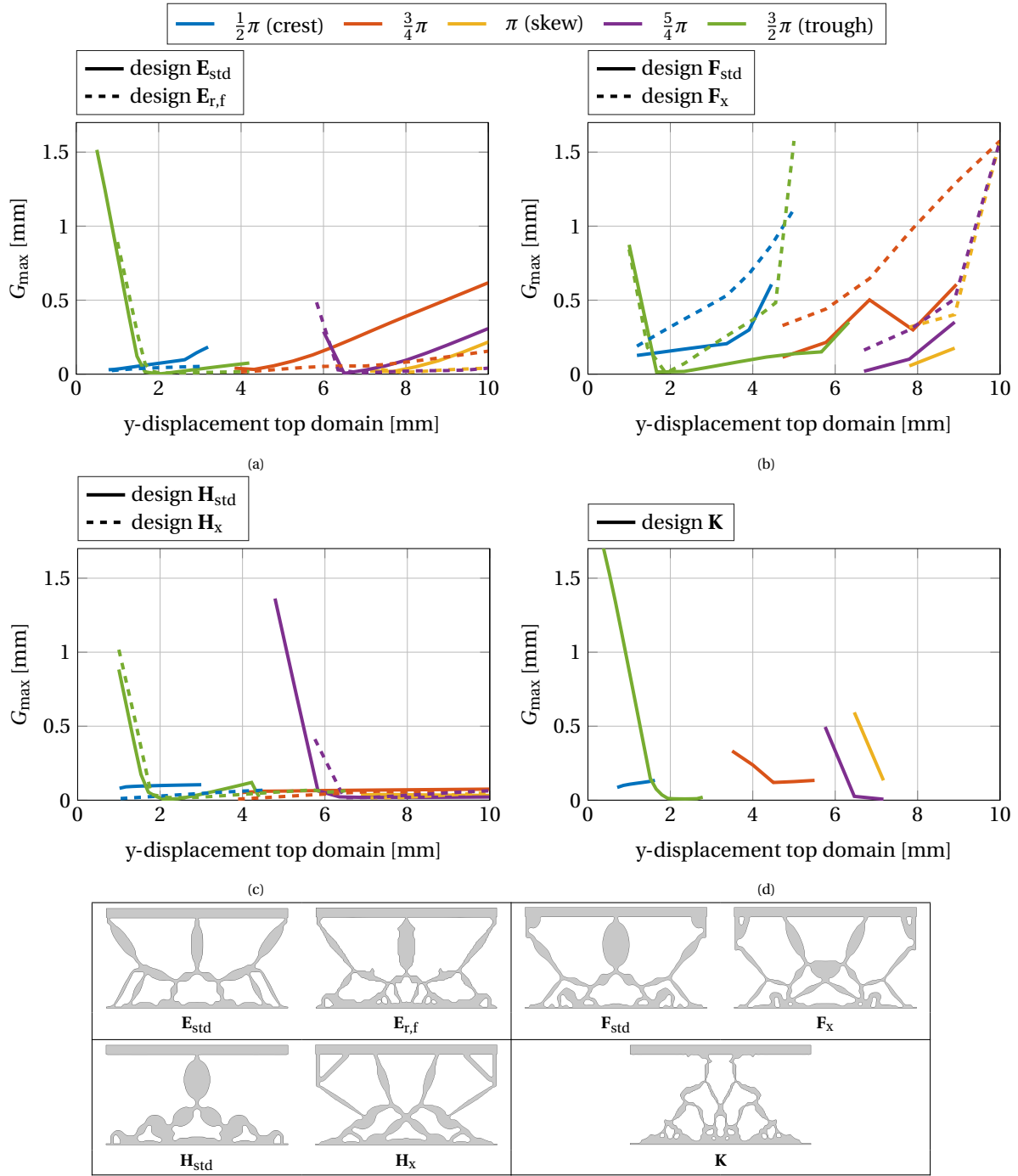


Figure 6.11: Maximum gap size G_{\max} during the contact studies versus the absolute prescribed y-displacement of the top domain. Note that G_{\max} is only determined for instances where the effective contact area relative to the pad length ($A_{c,\text{eff}}/w_d$) is greater than 0.5.

6.2.7. DISCUSSION

If we were to evaluate an ideal rigid body mechanism with zero-friction joints, the reaction forces for the performed studies would be zero up to the point where the bearing pad makes full contact with the counter surface. At that instance, the reaction forces would jump to a large value in case the mechanism gets into a 'locked' state. Due to the elasticity in the structures this behavior is only approximated but the trend can still be recognized in Figure 6.9. The curves transition from a gentle into a steep slope within a narrow region in

all evaluated positions on the counter surface.

EFFECTIVE CONTACT AREA AND MAXIMUM GAP SIZE

Ideally 100 % effective contact area should be achieved at the inflection point. This would indicate that the bearing pad easily deforms into the shape of the counter surface in all positions. Figure 6.10 reveals that none of the designs achieve 100 % contact area at all positions. However, 90 % is achieved in most cases except for design \mathbf{H}_{std} and \mathbf{K} . The force needed to get to 90 % contact area is largest for the positions where the counter surface is convex (being the crest position and the position between crest and skew where $\text{shift}_x = \frac{3}{4}\pi$). This is actually the desired behavior since adding a pressure supply in the middle of the bearing pad facilitates deformation into the convex positions and will thus compensate for the higher stiffness in those positions.

Since the effective contact area plots for the through position (where $\text{shift}_x = \frac{3}{2}\pi$) are constantly at 100% for most of the designs we have to take a look at the plots for the maximum gap size (G_{max}) in Figure 6.11. For all of the designs G_{max} gets down to values below 0.1 mm close to the inflection point of the reaction forces which indicates that sufficient deformation of the bearing pad in the trough position is not an issue. Considering the other positions as well, the figures show that G_{max} is consistently below 0.25 mm for for design $\mathbf{E}_{r,f}$, \mathbf{H}_{std} and \mathbf{H}_x after the contact area got over 90 %. The other designs show larger maximum gap sizes, especially design \mathbf{F}_x where the values get up to 1.5 mm. In order to determine if this is still acceptable, we recommended to setup a structural model of the designs and extend it with a 1D Reynolds equation at the bearing pad to simulate the fluid film. This will provide insight into the typical film height for a chosen supply pressure which can be compared to the maximum gap size.

EFFECTS OF OPTIMIZATION PARAMETERS

Figure 6.9a shows that the performance of design \mathbf{E}_{std} and $\mathbf{E}_{r,f}$ is very similar even though a reaction force requirement was implemented for design $\mathbf{E}_{r,f}$. Design $\mathbf{E}_{r,f}$ does even improve the maximum load for the skew position. Comparing design \mathbf{E}_{std} to \mathbf{F}_{std} and \mathbf{F}_x (Figure 6.9b) it can be noticed that the load to achieve 90 % contact for the crest position is larger for design \mathbf{F}_{std} and \mathbf{F}_x even though they have a lower constraint value for the crest deformations. The value for $SE_{crest,max}^p$ was $1.0 * 10^{-3}$ for design \mathbf{F}_{std} and \mathbf{F}_x compared to $2.5 * 10^{-3}$ for design \mathbf{E}_{std} which should enable design \mathbf{F}_{std} and \mathbf{F}_x to have much better deformability for the crest position. It is suspected that the amplitude of the counter surface ($\alpha = 11.3$ mm) was not large enough to reveal the influence of $SE_{crest,max}^p$ on the performance since Table 6.6 predicted a maximum value for α ranging from 59.6 to 87.9 mm for design \mathbf{E}_{std} , \mathbf{F}_{std} and \mathbf{F}_x .

From Figure 6.9c it is evident that design \mathbf{H}_{std} has very low load bearing capability. This is caused by its low x-stiffness making the design prone to 'sliding' on top of the counter surface (see Figure 6.12). The addition of the horizontal stiffness term in the objective as done for design \mathbf{H}_x proves to significantly improve performance of the bearing in all aspects for those particular boundary conditions. The the maximum load as well as the stiffness (Figure D.8c) are more than doubled for almost all positions at the counter surface. The maximum contact area for the convex positions (where $\text{shift}_x = \frac{3}{4}\pi$ or π) is also increased from 70 % to 90 %. Comparison of design \mathbf{F}_{std} and \mathbf{F}_x (Figure 6.9b) also shows that the inclusion of x-stiffness in the objective can improve the performance of designs with a larger bound on SE_{skew}^p . Design \mathbf{F}_x proves to have a higher stiffness for all positions as well as an increased maximum load in most cases. The improvement is greatest for the skew position (where $\text{shift}_x = \pi$) which was expected since the horizontal loads are largest for this case.

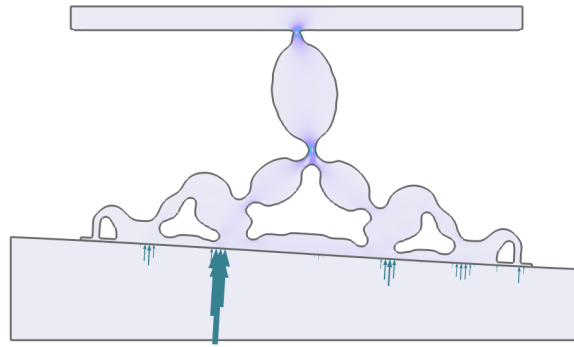


Figure 6.12: Sliding behavior of design H_{std} in the skew position ($shift_x = \pi$). More details can be found in Figure D.5.

Generally speaking, it is desirable to minimize the difference in maximum load between the positions on the counter surface since the lowest maximum load determines the maximal output pressure as explained in subsection 6.2.3. Significant variations in maximum load indicate that the design has a predisposition for one of the positions on the sinusoidal counter surface. Design $E_{r,f}$, F_x and H_x show the lowest amount of variation in maximum load. On the contrary, design K is performing worst in that regard. The design is especially limited for the skew position which can be explained by the higher implemented bound for SE_{skew}^p compared to the other designs. In hindsight this could also have been predicted based on the performed α_{max} study shown in Table D.1. There, the design was estimated to yield at the skew position for $\alpha = 11.5$ mm in a load case with only prescribed displacements on the bearing pad. The implemented amplitude of 11.3 mm for the counter surface was apparently too close to this bound. A limit of looking at the variation for the maximum load is that it has been determined based on the yield strength of the material. To improve on this, it should be investigated if the same behavior is present for a material of the structures that is more realistic for the application where also fatigue life and material nonlinearity is considered.

INVESTIGATION OF CONTACT PRESSURE PROFILES

Lastly, we take a look at the shape of the contact pressure profiles for the designs at the different positions on the counter surface. For this purpose, the reader is referred to the plots of the deformed configurations in Appendix D.2 where blue arrows are used to give an indication for the contact pressure profile. The arrows are proportional to the magnitude of the contact pressure but scaled differently between the positions on the counter surface. Note that in those plots the step in the auxiliary sweep where σ_{max} is closest to 45 MPa is visualized and not necessarily the final step like in Figure 6.6.

It can be observed that for most of the designs, the contact pressure peaks at few distinct regions where a 'link' is connected to the bearing pad. Design E_{std} has 6 peaks and design F_{std} , F_x and H_x have 4. Design H_{std} and K exhibit inconsistent behavior across the positions on the counter surface and will not be further considered. It is interesting to note that for design $E_{r,f}$ the contact pressure is more evenly distributed which is attributed to the increased thickness of the bearing pad. When examining the shape of the contact pressure profiles of design E_{std} , F_{std} , F_x and H_x it can be observed that the peak heights are higher towards the middle fairly consistently and thus very roughly adhere to the requirement of a triangular reaction profile. To understand why this is happening, even though none of these structures included a requirement on the reaction profile, we have to look back at the load case for SE_{crest}^p in Figure 4.5. For the implemented offset of -0.5 m it can be seen that the deformations in the middle of the pad are lower than at the sides. This leads to designs with higher stiffness in the middle and lower stiffness towards the sides of the structure. Another thing notable is the fact that design $E_{r,f}$, which actually did include a reaction profile requirement, has a seemingly worse contact pressure profile where the largest peaks are found to be at the sides of the structure.

Based on the above observations it is recommended refrain from investing additional effort into TO approaches with a requirement on the reaction profile. Instead, the performance of designs which show a rough satisfaction of the triangular reaction profile (like design E_{std} , F_{std} , F_x and H_x) should be evaluated with the inclusion of the fluid film for a fluid supply in the middle of the bearing pad. The insights gained from the results in chapter 5 can also be used to further improve their performance or as an inspiration for novel de-

signs.

6.3. VALIDATION OF REACTION PROFILES USED IN THE OPTIMIZATIONS

The final section of the current chapter investigates how well the shape of the reaction profiles found during the optimizations corresponds with the contact pressure profile obtained with a contact study. The same contact model as introduced in subsection 6.1.3 is used with the difference that the counter surface is now flat and in initial contact with the bearing pad over its entire length. This is shown in Figure 6.13. The material utilized remains the same polymer (PA46-I) as previously. Its properties are provided in Table 6.2.

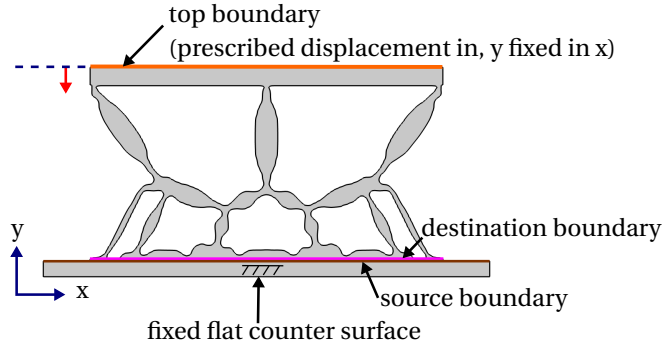


Figure 6.13: Boundary conditions for contact model in COMSOL to determine the contact pressure profile for a flat counter surface

Like in the contact studies before, the downward y-displacement of the top domain is incrementally increased in a parameter sweep. Figure 6.16 shows the deformed configuration of the evaluated designs together with the corresponding contact pressure profiles. In the same plots the reaction profiles obtained with the FE-analyses during the optimizations are provided. This is done for both investigated load cases provided in Figure 5.5. Note that we are only interested in how well the shape matches the contact pressure and not actual magnitudes. Therefore, the reaction forces obtained with the FE-model used in the optimizations are scaled such that comparison of the shapes is conveniently possible. The contact pressure from the step in the study where the σ_{max} is closest to the yield strength is used if possible. For design **K** and $F_{pad,d}$ the structure starts to 'slide' towards one of the sides before σ_{max} gets close to the yield strength which is illustrated in Figure 6.14. In those cases, the contact pressure from the last step before the sliding occurs is used.

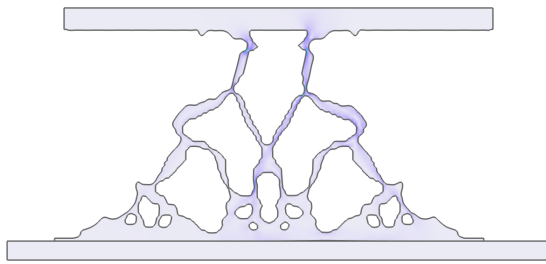


Figure 6.14: Sliding behavior of design **K** in contact study under compression against a flat counter surface.

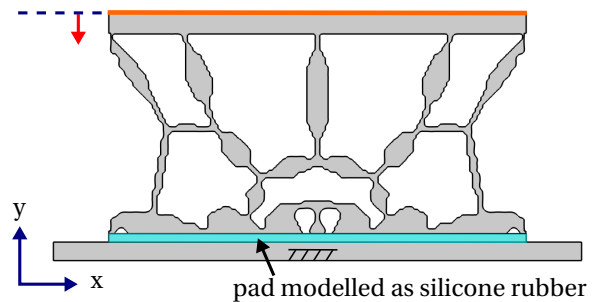


Figure 6.15: Model setup for design $F_{pad,d}$

For the TO result from the approach with the low stiffness bearing pad Table 5.5.2 a separate domain is added to the geometry (see Figure 6.15) and assigned the material properties of silicon rubber with Young's modulus $E_{pad} = 1$ MPa and Poisson's ratio $\nu_{pad} = 0.49$.

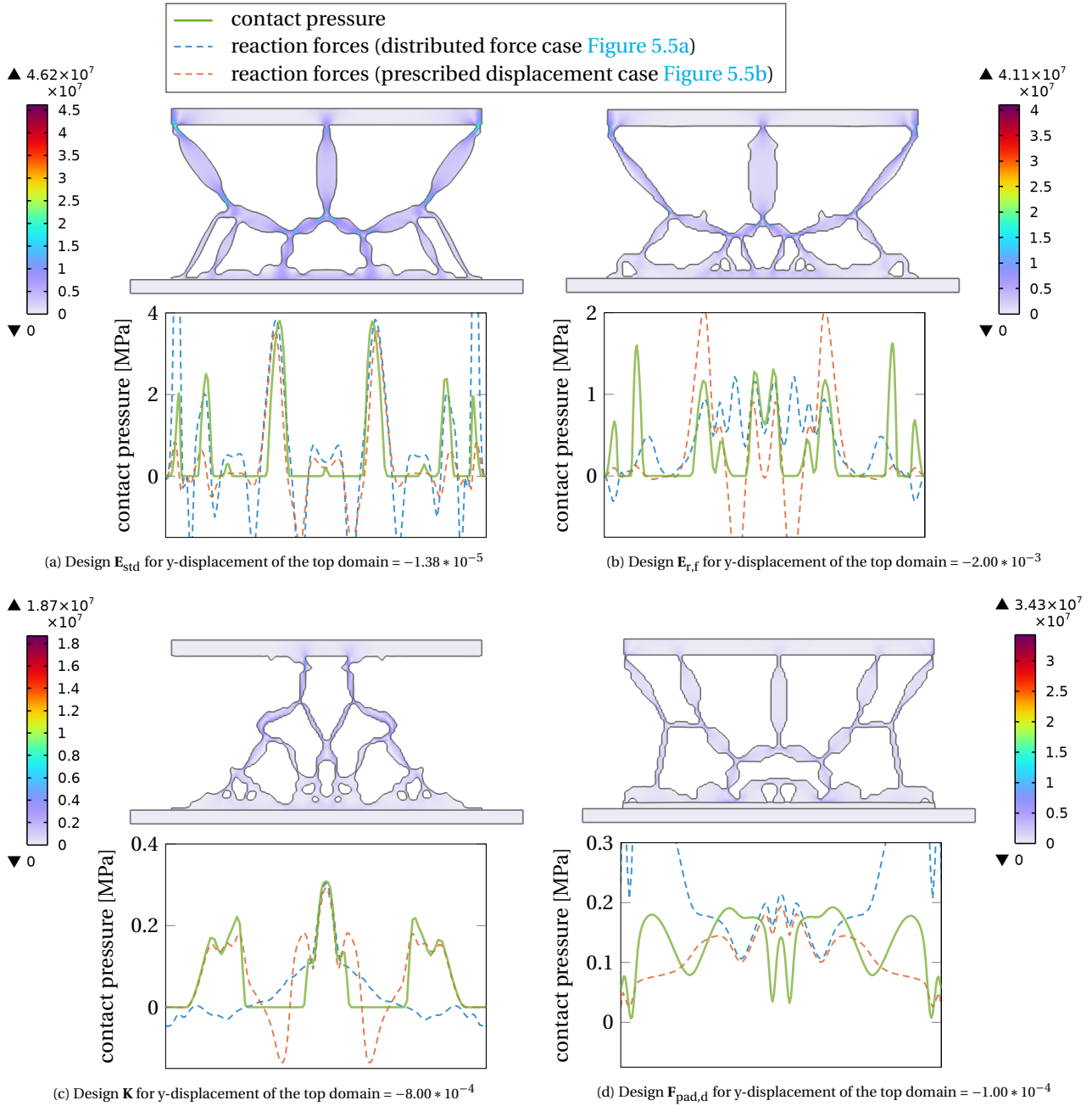


Figure 6.16: Contact pressure profile from a contact study of design E_{std} , $E_{r,f}$, K , and $F_{pad,d}$ compared to the reaction force profiles obtained with the FE model used in the optimizations

6.3.1. DISCUSSION

Before going into the findings, we would like to emphasize the differences between the FE model used during the optimizations and the model for the contact study. During the optimizations, the contact interface is simplified and modeled as a roller constraint which means that reaction forces can get negative. Another factor is the difference in mesh size of the contact boundary. Also, the post-processing step where the designs are translated from a grey scale representation within a quadrilateral element mesh of 150 by 75 elements to a geometry represented by between roughly 33000 and 55000 triangular elements Table C.1, inherently introduces some error.

Keeping the differences of the models in mind, the results displayed in Figure 6.16a show a remarkable coincidence in relative peak height between the contact pressure and the reaction forces determined with the

distributed force case. There, only the reaction forces of the most outward peaks are significantly overestimated for the FE model in the optimizations. On the contrary, for the prescribed displacement case the reaction forces are underestimated for the peaks towards the outside of the structure. For the result in [Figure 6.16c](#) the reaction profile determined with the prescribed displacement case is representing the shape of the contact pressure quite well over the entire pad while the shape obtained with the distributed force case is getting inaccurate towards the sides. This shows that FE models are very inconsistent in their prediction of the reaction forces towards the sides of the bearing pad.

For design $\mathbf{E}_{r,f}$ and $\mathbf{F}_{pad,d}$ ([Figure 6.16b](#) and [Figure 6.16d](#)) the reaction force profiles obtained with both load cases are not a good representation of the contact pressure. For design in [Figure 6.16d](#) the low stiffness bearing pad was expected to cause unpredictable behavior ([Table 5.5.2](#)) which is confirmed here.

Considering both load cases, the reaction force profiles seem to correspond best with the contact pressure of the real model for design \mathbf{E}_{std} . This is attributed to the fact that the corresponding TO result has less grey elements and artifacts than present in $\mathbf{E}_{r,f}$ and \mathbf{K} . The higher robustness value Δ_η of 0.1 compared to 0.05 utilized for design $\mathbf{E}_{r,f}$ and \mathbf{K} could also play a role in minimizing the effects of the translation step from black and white image into the geometry for the COMSOL model.

Generally, this brief study proves that the shape of the contact pressure can be predicted with the approach used in the optimizations with sufficient accuracy in some cases. However, it can not be concluded that either of the utilized load cases is performing better overall. A more in-depth study on this matter would have to be executed in order to find out why the observed deviations for some of the cases occur.

7 CONCLUSIONS AND RECOMMENDATIONS

7.1. CONCLUSIONS

The development of deformable hydrostatic bearings for sinusoidal counter surfaces is still in its infancy and alternatives to the existing approaches are sought. This work presented the implementation of topology optimization for the design problem of deformable hydrostatic bearings.

Structures for use in this new type of hydrostatic bearings need to enable deformation of a bearing pad into the continuously changing shape of the counter surface while supporting large vertical loads. This was considered in the fundamental problem formulation of the optimization problems through utilization of strain energy terms under different loading conditions. The performed optimizations resulted in compliant mechanisms which can easily be translated into their linkage mechanism counterparts. The novel designs show interesting strategies to enable deformation of the bearing pad into the required positions on the sinusoidal counter surface while maintaining high load bearing capability. Slight variations of the formulation, like adding a requirement for horizontal stiffness, prove to deliver insight in how the designs can be improved.

Based on the reaction profile of the designs, under the correct loading conditions, a prediction about the performance can be made. Ideally the reaction profile should have a triangular shape in case the fluid supply is placed in the middle. The problem formulation of the optimization has been extended in order to obtain designs adhering to this requirement. Two different ways were considered in the implementation under the name of 'pressure profile matching' and 'soft reaction constraint' (where the requirement was relaxed). For the 'pressure profile matching' approach it was found that there is a tradeoff between the amount of grey area present and how well the reaction profile is satisfied. In results with acceptable amount of grey area a triangular reaction profile can only be achieved approximately. Optimization problems formulated according to the 'soft reaction constraint' approach prove to be even harder to solve without obtaining grey area. The 'soft reaction approach,' was found to be more restrictive in practice, particularly at the center of the bearing pad. Overall, the designs generated with both approaches provide insights in how the reaction profile of a deformable hydrostatic bearing could be improved. However, finding clear-cut designs with the ideal shape for the reaction profile appears to be exceedingly challenging, if not impossible, for a finite minimum feature size.

In order to evaluate the performance of the designs, a more realistic model was setup with COMSOL Multiphysics®. In this model the contact interface is simulated correctly as opposed to the simplified FE models used for the optimizations. The evaluation of numerous results of the optimizations provides an indication of the load range that can be handled by the designs when made out of a polymer. It has been found that most of the evaluated designs enable sufficient deformation of the bearing pad into the shape of the counter surface for all positions on the sinusoidal counter surface. Including a horizontal stiffness requirement in the optimization is demonstrated to improve performance of the predicted maximum load without significantly affecting the performance in other areas. Therefore, horizontal stiffness should be considered in future approaches utilizing topology optimization. Investigation of the contact pressures revealed that the inclusion of a requirement on the reaction profile doesn't necessarily result in a triangular profile of the contact pressure. Interestingly, results for optimizations without requirement on the reaction profile consistently show more desirable shapes for the contact pressure which makes them the more promising candidates to consider in future efforts on the research topic.

7.2. RECOMMENDATIONS

It is recommended to further investigate the behavior of the structures by performing simulations where a fluid supply is added in the middle of the bearing pad and the lubricating film modeled with the Reynolds equation. This should be done for the designs which didn't include a requirement on the reaction profile in the optimization since those are expected to have more potential. In case the desired performance is not achieved, the designs could be manually improved by incorporating some of the approaches found by the optimizer in this work.

Another approach that is deemed valuable to pursue is translation of a selection of designs into an ideal linkage mechanism where a single compliant link at the bottom acts as the bearing pad. A model of the linkage system could be parameterized by the lengths of the links and optimized. This might enable to perform optimizations which include a model for the fluid film.

For approaches utilizing topology optimization in the future the addition of stress constraints in the formulation should be considered. Improved distribution of the stresses is expected to improve the maximal vertical loads that can be handled by the structures.

BIBLIOGRAPHY

- [1] *What's stopping even bigger Wind Turbines? Blade speed and flexing? More likely manufacturing and installation capacity*, (2023).
- [2] H. M. Slot, E. R. M. Gelinck, C. Rentrop, and E. van der Heide, *Leading edge erosion of coated wind turbine blades: Review of coating life models*, *Renewable Energy* **80**, 837 (2015).
- [3] N. F. B. Diepeveen, *On the Application of Fluid Power Transmission in Offshore Wind Turbines*, (2013).
- [4] *DOT - How it works*, .
- [5] P. Amoroso, R. a. J. van Ostayen, and F. Perassi, *Rolling-Sliding Performance of Radial and Offset Roller Followers in Hydraulic Drivetrains for Large Scale Applications: A Comparative Study*, *Machines* **11** (2023), 10.3390/machines11060604.
- [6] J. P. A. Nijssen, *Compliant Full Film Lubricated Bearings: Concept Design & Development*, (2022), 10.4233/uuid:b0a6cb46-5b3d-47a5-9cbc-3db7cdd42a4a.
- [7] A. van Beek, *Advanced Engineering Design*, 6th ed. (Delft University of Technology).
- [8] V. van Parijs, J. Nijssen, and R. van Ostayen, *Whiffletree based supports for self-adjustable hydrostatic bearings*, *Advances in Mechanical Engineering* **13**, 16878140211055573 (2021), publisher: SAGE Publications.
- [9] J. P. A. Nijssen and R. A. J. van Ostayen, *Compliant Hydrostatic Bearings Utilizing Functionally Graded Materials*, *Journal of Tribology* **142** (2020), 10.1115/1.4047299.
- [10] *Mechanism (engineering)*, (2022), page Version ID: 1075641952.
- [11] *About Compliant Mechanisms*, .
- [12] H. M. J. Soemers, *Design principles for precision mechanisms* (2011).
- [13] *3 Parallel & tangential folded leaf springs*, .
- [14] S. Cai, W. Zhou, H. Wei, and M. Zhu, *Topology Optimization Design of Multi-Input-Multi-Output Compliant Mechanisms with Hinge-Free Characteristic and Totally Decoupled Kinematics*, *Applied Sciences* **13**, 4627 (2023), number: 7 Publisher: Multidisciplinary Digital Publishing Institute.
- [15] O. Sigmund, *On the Design of Compliant Mechanisms Using Topology Optimization*, *Mechanics of Structures and Machines* **25**, 493 (1997), publisher: Taylor & Francis _eprint: <https://doi.org/10.1080/08905459708945415>.
- [16] O. Sigmund and K. Maute, *Topology optimization approaches: A comparative review*, *Structural and Multidisciplinary Optimization* **48**, 1031 (2013).
- [17] M. P. Bendsoe, *Optimal shape design as a material distribution problem*, *Structural optimization* **1**, 193 (1989).
- [18] G. I. N. Rozvany, M. Zhou, and T. Birker, *Generalized shape optimization without homogenization*, *Structural Optimization* **4**, 250 (1992).
- [19] O. Sigmund, *Morphology-based black and white filters for topology optimization*, *Structural and Multidisciplinary Optimization* **33**, 401 (2007).

- [20] B. Zhu, X. Zhang, H. Zhang, J. Liang, H. Zang, H. Li, and R. Wang, *Design of compliant mechanisms using continuum topology optimization: A review*, [Mechanism and Machine Theory](#) **143**, 103622 (2020).
- [21] L. Cao, A. Dolovich, and W. J. Zhang, *On understanding of design problem formulation for compliant mechanisms through topology optimization*, [Mechanical Sciences](#) **4**, 357 (2013), publisher: Copernicus GmbH.
- [22] G. I. N. Rozvany, *A critical review of established methods of structural topology optimization*, [Structural and Multidisciplinary Optimization](#) **37**, 217 (2009).
- [23] A. Diaz and O. Sigmund, *Checkerboard patterns in layout optimization*, [Structural Optimization](#) **10**, 40 (1995).
- [24] O. Sigmund, *A 99 line topology optimization code written in Matlab*, [Structural and Multidisciplinary Optimization](#) **21**, 120 (2001).
- [25] K. Svanberg, *The method of moving asymptotes—a new method for structural optimization*, [International Journal for Numerical Methods in Engineering](#) **24**, 359 (1987), _eprint: <https://onlinelibrary.wiley.com/doi/pdf/10.1002/nme.1620240207>.
- [26] N. H. Kim, T. Dong, D. Weinberg, and J. Dalidd, *Generalized Optimality Criteria Method for Topology Optimization*, [Applied Sciences](#) **11**, 3175 (2021), number: 7 Publisher: Multidisciplinary Digital Publishing Institute.
- [27] J. P. A. Nijssen, A. Kempenaar, and N. Diepeveen, *Development of an interface between a plunger and an eccentric running track for a low-speed seawater pump*, [Fluid Power Networks](#) **1** (2018), 10.18154/RWTH-2018-224521, publisher: IFK.
- [28] S. Koppen, M. Langelaar, and F. van Keulen, *A simple and versatile topology optimization formulation for flexure synthesis*, [Mechanism and Machine Theory](#) **172**, 104743 (2022).
- [29] S. Koppen, *Topology optimization of compliant mechanisms with multiple degrees of freedom*, (2022), 10.4233/uuid:21994a92-e365-4679-b6ac-11a2b70572b7, publisher: Delft University of Technology.
- [30] W. Maas, *The topology optimization of a compliant variable-camber morphing wing*, (2021).
- [31] J. D. Cook, *Soft maximum for convex optimization*, (2010).
- [32] T. E. Bruns and D. A. Tortorelli, *Topology optimization of non-linear elastic structures and compliant mechanisms*, [Computer Methods in Applied Mechanics and Engineering](#) **190**, 3443 (2001).
- [33] O. Sigmund, *Manufacturing tolerant topology optimization*, [Acta Mechanica Sinica](#) **25**, 227 (2009).
- [34] F. Wang, B. S. Lazarov, and O. Sigmund, *On projection methods, convergence and robust formulations in topology optimization*, [Structural and Multidisciplinary Optimization](#) **43**, 767 (2011).
- [35] E. Andreassen, A. Clausen, M. Schevenels, B. S. Lazarov, and O. Sigmund, *Efficient topology optimization in MATLAB using 88 lines of code*, [Structural and Multidisciplinary Optimization](#) **43**, 1 (2011).
- [36] *Stanyl® TW363, PA46-I - DSM Engineering Materials - Plastics Finder*, .
- [37] *Titanium grade 19: eigenschappen*, (2020).
- [38] *Meshing for Contact Analysis*, .

A SENSITIVITY ANALYSES

The discretized system can be partitioned as shown in Equation 4.1.

$$\begin{bmatrix} \mathbf{K}_{ff} & \mathbf{K}_{fp} \\ \mathbf{K}_{pf} & \mathbf{K}_{pp} \end{bmatrix} \begin{bmatrix} \mathbf{u}_f \\ \mathbf{u}_p \end{bmatrix} = \begin{bmatrix} \mathbf{f}_f \\ \mathbf{f}_p \end{bmatrix} \quad (\text{A.1})$$

where:

\mathbf{f}_f = applied forces

\mathbf{f}_p = reaction forces

\mathbf{u}_f = displacements of free nodes

\mathbf{u}_p = prescribed displacements

This can also be expressed as the two equations given below:

$$\mathbf{u}_f(\mathbf{x}) = \mathbf{K}_{ff}(\mathbf{x})^{-1} (\mathbf{f}_f - \mathbf{K}_{fp}(\mathbf{x}) \mathbf{u}_p) \quad (\text{A.2})$$

$$\mathbf{f}_p(\mathbf{x}) = \mathbf{K}_{pf}(\mathbf{x}) \mathbf{u}_f(\mathbf{x}) + \mathbf{K}_{pp}(\mathbf{x}) \mathbf{u}_p \quad (\text{A.3})$$

The derivative of an inverse matrix will be used several times in the analysis and is derived below:

$$\begin{aligned} 0 &= \frac{d\mathbf{I}}{d\mathbf{x}} = \frac{d\mathbf{K}\mathbf{K}^{-1}}{d\mathbf{x}} = \frac{d\mathbf{K}}{d\mathbf{x}} \mathbf{K}^{-1} + \mathbf{K} \frac{d\mathbf{K}^{-1}}{d\mathbf{x}} \\ \mathbf{K} \frac{d\mathbf{K}^{-1}}{d\mathbf{x}} &= -\frac{d\mathbf{K}}{d\mathbf{x}} \mathbf{K}^{-1} \\ \mathbf{K}^{-1} \mathbf{K} \frac{d\mathbf{K}^{-1}}{d\mathbf{x}} &= -\mathbf{K}^{-1} \frac{d\mathbf{K}}{d\mathbf{x}} \mathbf{K}^{-1} \\ \frac{d\mathbf{K}^{-1}}{d\mathbf{x}} &= -\mathbf{K}^{-1} \frac{d\mathbf{K}}{d\mathbf{x}} \mathbf{K}^{-1} \end{aligned} \quad (\text{A.4})$$

A.1. SENSITIVITIES OF STRAIN ENERGY TERMS

A.1.1. PURE APPLIED FORCES

In the load cases with pure applied forces we have $\mathbf{u}_p = \mathbf{0}$. The strain energy is given by:

$$SE^f(\mathbf{x}) = \frac{1}{2} \mathbf{u}_f^T(\mathbf{x}) \mathbf{f}_f \quad (\text{A.5})$$

Equation A.2 can be simplified to:

$$\mathbf{u}_f(\mathbf{x}) = \mathbf{K}_{ff}(\mathbf{x})^{-1} \mathbf{f}_f \quad (\text{A.6})$$

Calculation of the sensitivities for $\mathbf{u}_f(\mathbf{x})$ yields:

$$\frac{d\mathbf{u}_f}{d\mathbf{x}} = \frac{d\mathbf{K}_{ff}^{-1}}{d\mathbf{x}} \mathbf{f}_f = -\mathbf{K}_{ff}^{-1} \frac{d\mathbf{K}_{ff}}{d\mathbf{x}} \mathbf{K}_{ff}^{-1} \mathbf{f}_f \quad (\text{A.7})$$

Utilizing Equation A.7 the sensitivities of $SE^f(\mathbf{x})$ can be expressed as:

$$\frac{dSE^f}{d\mathbf{x}} = \frac{1}{2} \frac{d\mathbf{u}_f^T}{d\mathbf{x}} \mathbf{f}_f = -\frac{1}{2} \mathbf{f}_f^T \mathbf{K}_{ff}^{-1} \frac{d\mathbf{K}_{ff}}{d\mathbf{x}} \mathbf{K}_{ff}^{-1} \mathbf{f}_f = -\frac{1}{2} \mathbf{u}_f^T \frac{d\mathbf{K}_{ff}}{d\mathbf{x}} \mathbf{u}_f \quad (\text{A.8})$$

Using the fact that $\mathbf{u}_p = \mathbf{0}$ Equation A.8 can also be given as:

$$\frac{dSE^f}{d\mathbf{x}} = -\frac{1}{2} \mathbf{u}^T \frac{d\mathbf{K}}{d\mathbf{x}} \mathbf{u} \quad (\text{A.9})$$

A.1.2. PURE PRESCRIBED DISPLACEMENTS

In the load cases with pure prescribed displacements we have $\mathbf{f}_f = \mathbf{0}$. The strain energy is given by:

$$SE^p(\mathbf{x}) = \frac{1}{2} \mathbf{u}_p^T \mathbf{f}_p(\mathbf{x}) \quad (\text{A.10})$$

Equation A.2 can be simplified to:

$$\mathbf{u}_f(\mathbf{x}) = -\mathbf{K}_{ff}(\mathbf{x})^{-1} \mathbf{K}_{fp}(\mathbf{x}) \mathbf{u}_p \quad (\text{A.11})$$

or alternatively:

$$-\mathbf{K}_{ff}(\mathbf{x}) \mathbf{u}_f(\mathbf{x}) = \mathbf{K}_{fp}(\mathbf{x}) \mathbf{u}_p \quad (\text{A.12})$$

Insertion of Equation A.11 into Equation A.3 gives:

$$\mathbf{f}_p(\mathbf{x}) = \left(\mathbf{K}_{pp}(\mathbf{x}) - \mathbf{K}_{pf}(\mathbf{x}) \mathbf{K}_{ff}(\mathbf{x})^{-1} \mathbf{K}_{fp}(\mathbf{x}) \right) \mathbf{u}_p \quad (\text{A.13})$$

Calculation of the sensitivities for $\mathbf{f}_p(\mathbf{x})$ Equation A.13 yields:

$$\frac{d\mathbf{f}_p}{d\mathbf{x}} = \left(\frac{d\mathbf{K}_{pp}}{d\mathbf{x}} - \frac{d\mathbf{K}_{pf}}{d\mathbf{x}} \mathbf{K}_{ff}^{-1} \mathbf{K}_{fp} + \mathbf{K}_{pf} \mathbf{K}_{ff}^{-1} \frac{d\mathbf{K}_{ff}}{d\mathbf{x}} \mathbf{K}_{ff}^{-1} \mathbf{K}_{fp} - \mathbf{K}_{pf} \mathbf{K}_{ff}^{-1} \frac{d\mathbf{K}_{fp}}{d\mathbf{x}} \right) \mathbf{u}_p \quad (\text{A.14})$$

Equation A.14 is used to come up with the sensitivities for $SE^p(\mathbf{x})$ as given in Equation A.10:

$$\frac{dSE^p}{d\mathbf{x}} = \frac{1}{2} \mathbf{u}_p^T \left(\frac{d\mathbf{K}_{pp}}{d\mathbf{x}} - \frac{d\mathbf{K}_{pf}}{d\mathbf{x}} \mathbf{K}_{ff}^{-1} \mathbf{K}_{fp} + \mathbf{K}_{pf} \mathbf{K}_{ff}^{-1} \frac{d\mathbf{K}_{ff}}{d\mathbf{x}} \mathbf{K}_{ff}^{-1} \mathbf{K}_{fp} - \mathbf{K}_{pf} \mathbf{K}_{ff}^{-1} \frac{d\mathbf{K}_{fp}}{d\mathbf{x}} \right) \mathbf{u}_p \quad (\text{A.15})$$

which can be simplified with help of Equation A.11 and the fact that $-\mathbf{u}_f(\mathbf{x})^T = \mathbf{u}_p^T \mathbf{K}_{pf}(\mathbf{x}) \mathbf{K}_{ff}(\mathbf{x})^{-1}$:

$$\frac{dSE^p}{d\mathbf{x}} = \frac{1}{2} \left(\mathbf{u}_p^T \frac{d\mathbf{K}_{pp}}{d\mathbf{x}} \mathbf{u}_p + \mathbf{u}_p^T \frac{d\mathbf{K}_{pf}}{d\mathbf{x}} \mathbf{u}_f + \mathbf{u}_f^T \frac{d\mathbf{K}_{ff}}{d\mathbf{x}} \mathbf{u}_f + \mathbf{u}_f^T \frac{d\mathbf{K}_{fp}}{d\mathbf{x}} \mathbf{u}_p \right) \quad (\text{A.16})$$

and can be expressed more elegantly as:

$$\frac{dSE^p}{d\mathbf{x}} = \frac{1}{2} \begin{bmatrix} \mathbf{u}_f^T & \mathbf{u}_p^T \end{bmatrix} \begin{bmatrix} \frac{d\mathbf{K}_{ff}}{d\mathbf{x}} & \frac{d\mathbf{K}_{fp}}{d\mathbf{x}} \\ \frac{d\mathbf{K}_{pf}}{d\mathbf{x}} & \frac{d\mathbf{K}_{pp}}{d\mathbf{x}} \end{bmatrix} \begin{bmatrix} \mathbf{u}_f \\ \mathbf{u}_p \end{bmatrix} \quad (\text{A.17})$$

A.2. SENSITIVITIES OF REACTION FORCES

Because of the fact that $\mathbf{u}_p = \mathbf{0}$ for the case where the reaction forces need to be determined Equation A.2 can be simplified as follows:

$$\mathbf{u}_f = \mathbf{K}_{ff}^{-1} \mathbf{f}_f \quad (\text{A.18})$$

The reaction forces are given in Equation A.3 can also be simplified using $\mathbf{u}_p = \mathbf{0}$ again which gives:

$$\mathbf{f}_p = \mathbf{K}_{pf} \mathbf{u}_f \quad (\text{A.19})$$

The sensitivity of the reaction force with respect to the design variables can be written as follows (chain rule applied):

$$\frac{d\mathbf{f}_p}{d\mathbf{x}} = \frac{d\mathbf{K}_{pf}}{d\mathbf{x}} \mathbf{u}_f + \mathbf{K}_{pf} \frac{d\mathbf{u}_f}{d\mathbf{x}} \quad (\text{A.20})$$

In order to determine $\frac{d\mathbf{u}_f}{dx_j}$ we can make use of Equation A.18 which yields:

$$\frac{d\mathbf{u}_f}{d\mathbf{x}} = \frac{d\mathbf{K}_{ff}^{-1}}{d\mathbf{x}} \mathbf{f}_f + \mathbf{K}_{ff}^{-1} \frac{d\mathbf{f}_f}{d\mathbf{x}} \quad (\text{A.21})$$

Simplification of Equation A.21 (using the derivative of an inverse matrix property derived in Equation A.4) yields:

$$\frac{d\mathbf{u}_f}{d\mathbf{x}} = -\mathbf{K}_{ff}^{-1} \frac{d\mathbf{K}_{ff}}{d\mathbf{x}} \mathbf{K}_{ff}^{-1} \mathbf{f}_f = -\mathbf{K}_{ff}^{-1} \frac{d\mathbf{K}_{ff}}{d\mathbf{x}} \mathbf{u}_f \quad (\text{A.22})$$

Inserting Equation A.22 into Equation A.20 yields:

$$\frac{d\mathbf{f}_p}{d\mathbf{x}} = \frac{d\mathbf{K}_{pf}}{d\mathbf{x}} \mathbf{u}_f - \mathbf{K}_{pf} \mathbf{K}_{ff}^{-1} \frac{d\mathbf{K}_{ff}}{d\mathbf{x}} \mathbf{u}_f \quad (\text{A.23})$$

If we use a response $g(\mathbf{f}_p)$ which directly depends on the reaction forces \mathbf{f}_p and indirectly on the design variables \mathbf{x} the sensitivity of the response can be given as follows:

$$\frac{dg}{d\mathbf{x}} = \frac{dg}{d\mathbf{f}_p} \frac{d\mathbf{f}_p}{d\mathbf{x}} = \frac{dg}{d\mathbf{f}_p} \frac{d\mathbf{K}_{pf}}{d\mathbf{x}} \mathbf{u}_f - \frac{dg}{d\mathbf{f}_p} \mathbf{K}_{pf} \mathbf{K}_{ff}^{-1} \frac{d\mathbf{K}_{ff}}{d\mathbf{x}} \mathbf{u}_f \quad (\text{A.24})$$

We can also write this as:

$$\frac{dg}{d\mathbf{x}} = \frac{dg}{d\mathbf{f}_p} \frac{d\mathbf{K}_{pf}}{d\mathbf{x}} \mathbf{u}_f - \boldsymbol{\lambda}_f^T \frac{d\mathbf{K}_{ff}}{d\mathbf{x}} \mathbf{u}_f \quad (\text{A.25})$$

where:

$$\boldsymbol{\lambda}_f^T = \frac{dg}{d\mathbf{f}_p} \mathbf{K}_{pf} \mathbf{K}_{ff}^{-1} \quad (\text{A.26})$$

For efficient implementation of these sensitivities in MATLAB based on the 88-line TO code [35] it can be useful to rewrite the above expression. Using the fact that $\mathbf{u}_p = \mathbf{0}$ we can represent the result as follows:

$$\frac{dg}{d\mathbf{x}} = \begin{bmatrix} -\boldsymbol{\lambda}_f^T & \frac{dg}{d\mathbf{f}_p} \end{bmatrix} \begin{bmatrix} \frac{d\mathbf{K}_{ff}}{d\mathbf{x}} & \frac{d\mathbf{K}_{fp}}{d\mathbf{x}} \\ \frac{d\mathbf{K}_{pf}}{d\mathbf{x}} & \frac{d\mathbf{K}_{pp}}{d\mathbf{x}} \end{bmatrix} \begin{bmatrix} \mathbf{u}_f \\ \mathbf{u}_p \end{bmatrix} = \begin{bmatrix} -\boldsymbol{\lambda}_f^T & \frac{dg}{d\mathbf{f}_p} \end{bmatrix} \frac{d\mathbf{K}}{d\mathbf{x}} \mathbf{u} \quad (\text{A.27})$$

B ADDITIONAL INFO ON OPTIMIZATIONS

B.1. TYPICAL ITERATION TIMES

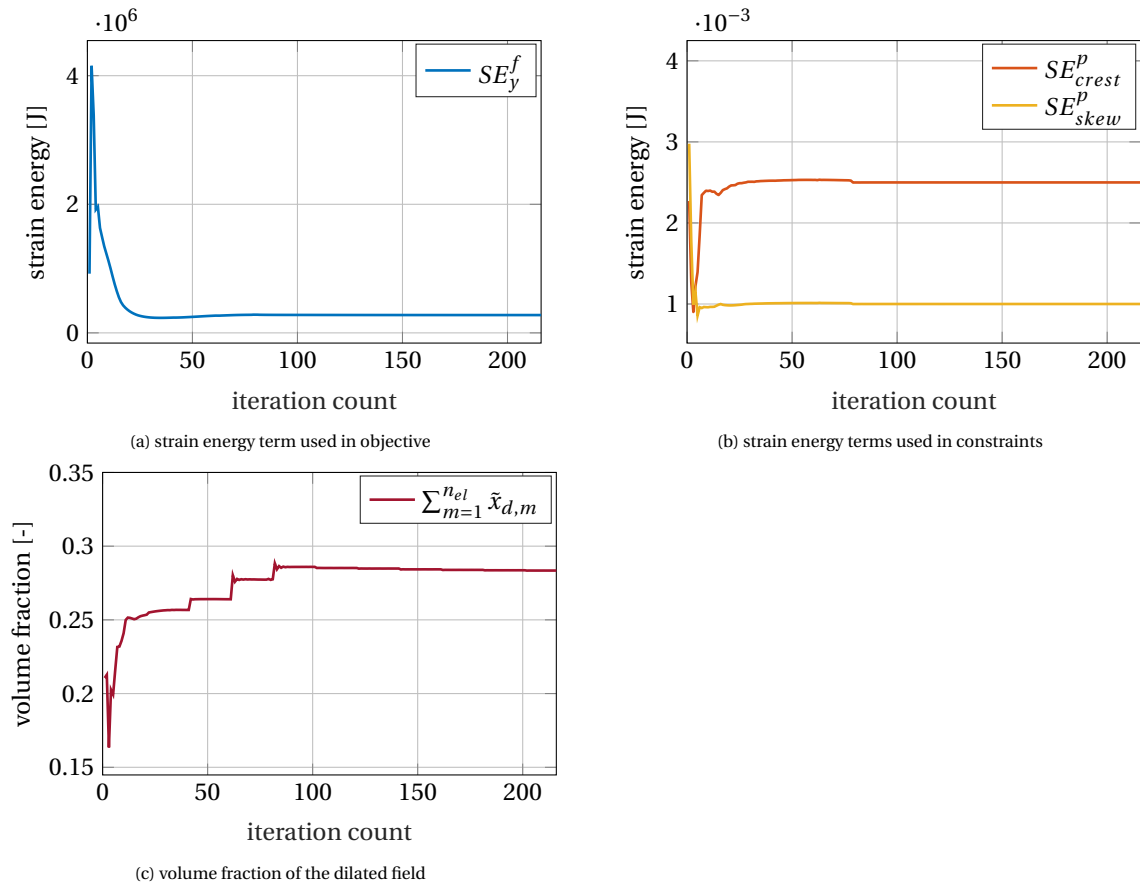
Below we provide the typical time per iteration for the different problem setups. The optimizations were performed on a HP ZBook Studio G3 laptop with an Intel(R) Core(TM) i7-6700HQ CPU (2.60 GHz). Note that the result as well as the reaction profile were also plotted after each iteration which affects the performance.

Table B.1: Typical run times

problem setup	typical run time per iteration
'standard' optimizations without requirement on reaction profile Table 5.5	$\approx 0.6 - 0.7$ seconds
optimizations with pressure profile matching penalty utilizing the distributed force load case Table 5.8	$\approx 5 - 6$ seconds
optimizations with pressure profile matching penalty utilizing the prescribed displacement load case Table 5.9	≈ 15 seconds

B.2. CONVERGENCE HISTORY

In the following figure the convergence history of the separate terms used in the objective and constraints for design \mathbf{E}_{std} is provided.

Figure B.1: Convergence histories for design \mathbf{E}_{std}

C ADDITIONAL INFORMATION ON THE COMSOL MODELS

C.1. CONVERTING IMAGE FILES INTO A GEOMETRY

In the main text it was mentioned that the 'Image to curve' add on is used to convert the black and white pictures of the TO results into a geometry in COMSOL. Figure C.1 shows a screenshot of the settings for the add-on. Care was taken to ensure that the size of the imported images (in terms of pixels) was constant for all of the evaluated designs. The parameter 'Image width' was kept at 0.226 m and 'Filter' set to 'Gaussian' for all of the evaluated designs. The parameter 'Contour threshold' was kept at 0.3 if possible but had to be increased up to 0.4 for some designs in order to avoid too thin members or unconnected regions. For the parameter 'Curve tolerance' mostly a value of $5e-4$ was used but for some designs this was increased up to $15e-4$. Increasing this parameter leads to smoother curves and thus larger deviation from the original image. Note that adjustments of this parameter are not visible in the preview for the contour lines. The geometry has to be created in order to see its effects. The remaining parameters were left unchanged.

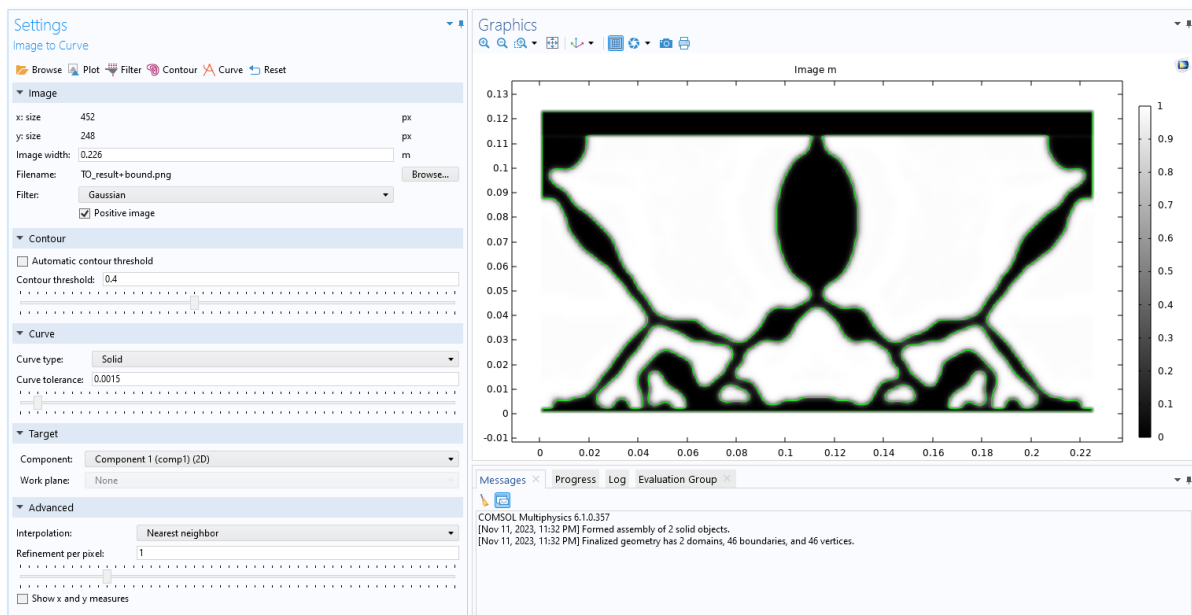
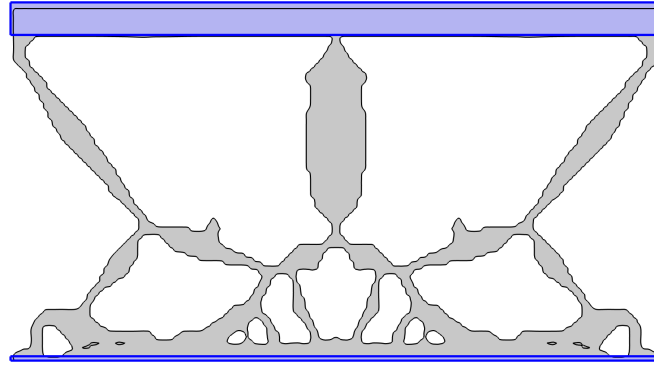


Figure C.1: Settings of the 'Image to curve' add-on for design F_{std}

C.2. CREATING SEPARATE BOUNDARIES FOR THE BOUNDARY CONDITIONS

The geometry that is obtained with "Image to curve" causes the boundary at the top and bottom of the design to get curved. To get perfectly straight separate boundaries again (in order to apply boundary conditions in COMSOL), two rectangular geometries are created, one on top of the non-design region for the lower boundary and one at the region of the fixation at the top. This is illustrated in the figure below.

Figure C.2: Additional geometries created for design $E_{r,f}$

C.3. MESH SIZES IN THE EVALUATION MODELS

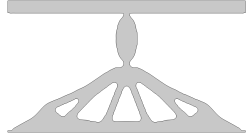

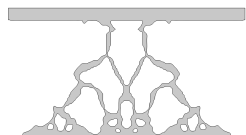
Table C.1: Mesh sizes of the designs for contact studies. A physics based triangular mesh with 'normal' element size was utilized. Note that this is without the elements for the counter surface. The number of nodes at the bottom of the bearing pad is also provided.

Design	# of triangular elements	# of nodes at bearing pad
E_{std}	34419	181
$E_{r,f}$	55764	165
F_{std}	10667	186
F_x	16474	158
$F_{pad,d}$	33004	227
H_{std}	20567	192
H_x	25246	138
K	51562	127

D ADDITIONAL DATA FROM EVALUATIONS

D.1. MAX α STUDY

Table D.1: Maximum amplitude for different TO results based on the skew and crest deformation case shown in [Figure 6.4](#)

TO Result	max α skew [mm]	max α crest [mm]
 design for $SE_{skew,max}^p = 1.0 * 10^{-3}$ from Table 5.4	24.6	35.0
 design for $SE_{crest,max}^p = 2.5 * 10^{-3}$ from Table 5.4	4.0	60.0
 design for K from Table 5.13	11.5	24.1

D.2. DEFORMED CONFIGURATIONS FROM CONTACT STUDIES

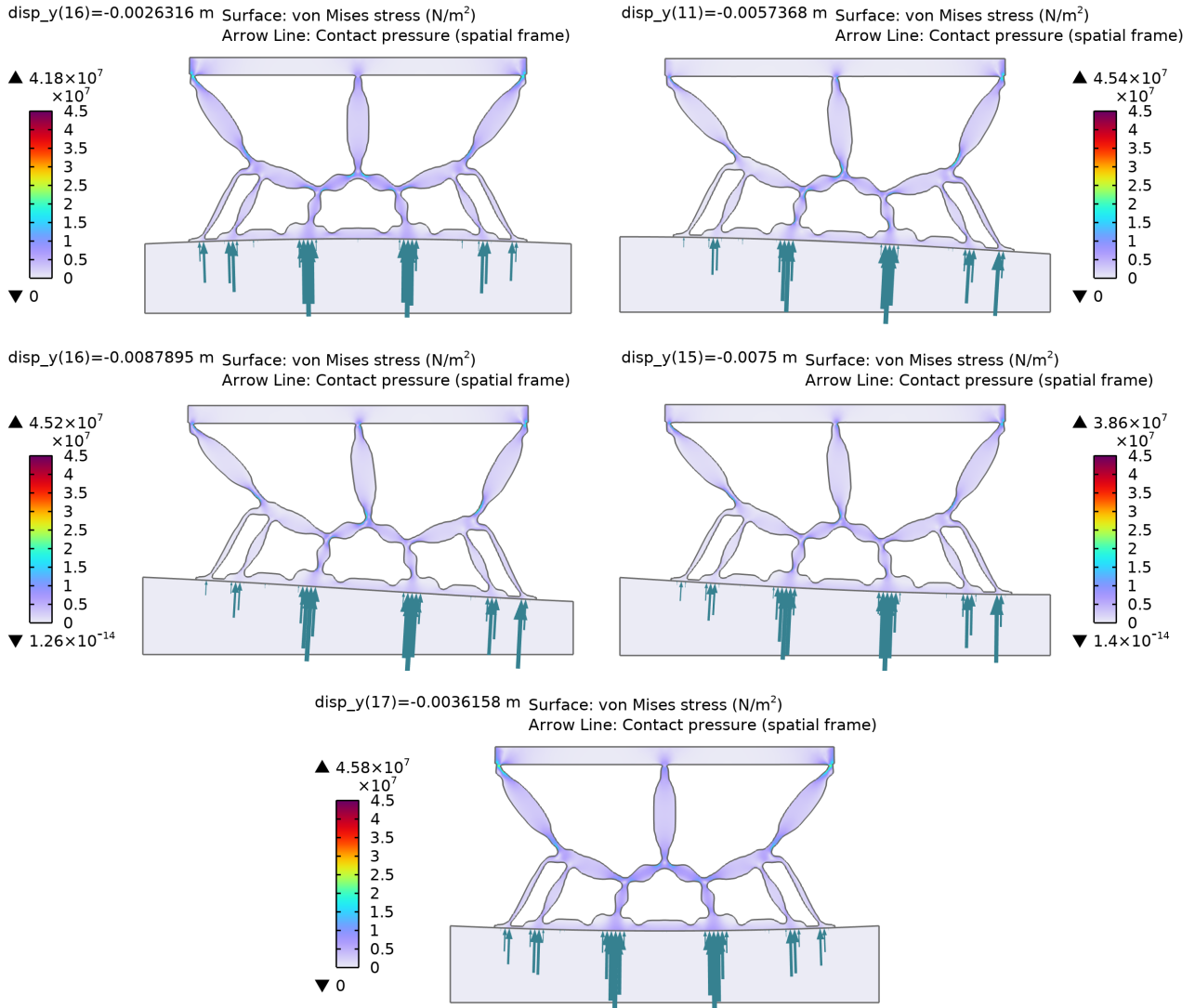


Figure D.1: Unscaled deformed configuration (from the study step closest to the maximum load) together with von Mises stress ⁶ for design E_{std} at all evaluated positions above the camring for the performed contact study. The size of the blue arrows is proportional to the contact pressure. However, not the same scaling is used between different positions.

⁶Note that the σ_{max} provided in these plots is obtained with a different interpolation of the stresses than for the stop criterion during the optimizations and the determination of the maximum load.

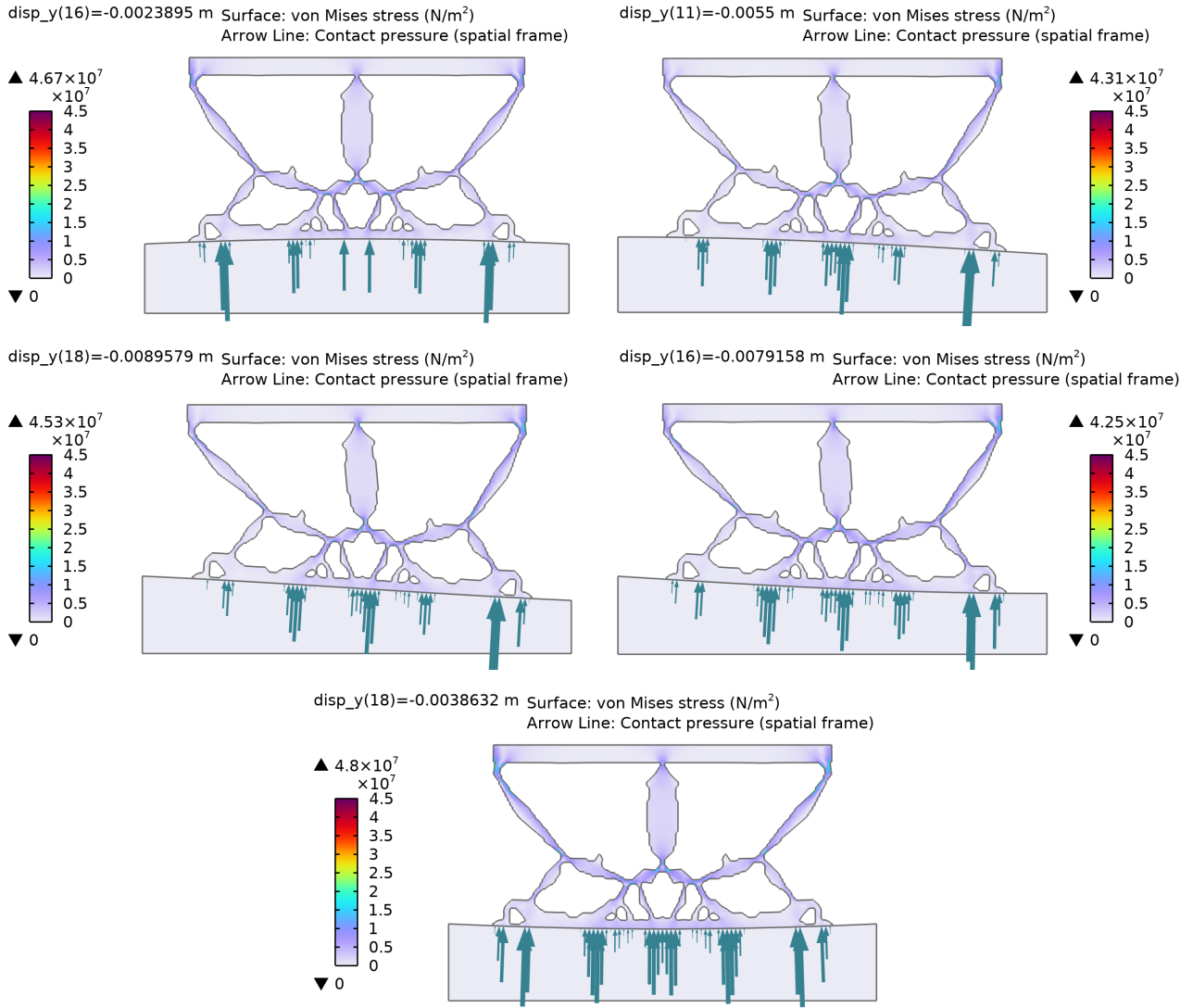


Figure D.2: Unscaled deformed configuration (from the study step closest to the maximum load) together with von Mises stress ⁶ for design $E_{r,f}$ at all evaluated positions above the camring for the performed contact study. The size of the blue arrows is proportional to the contact pressure. However, not the same scaling is used between different positions.

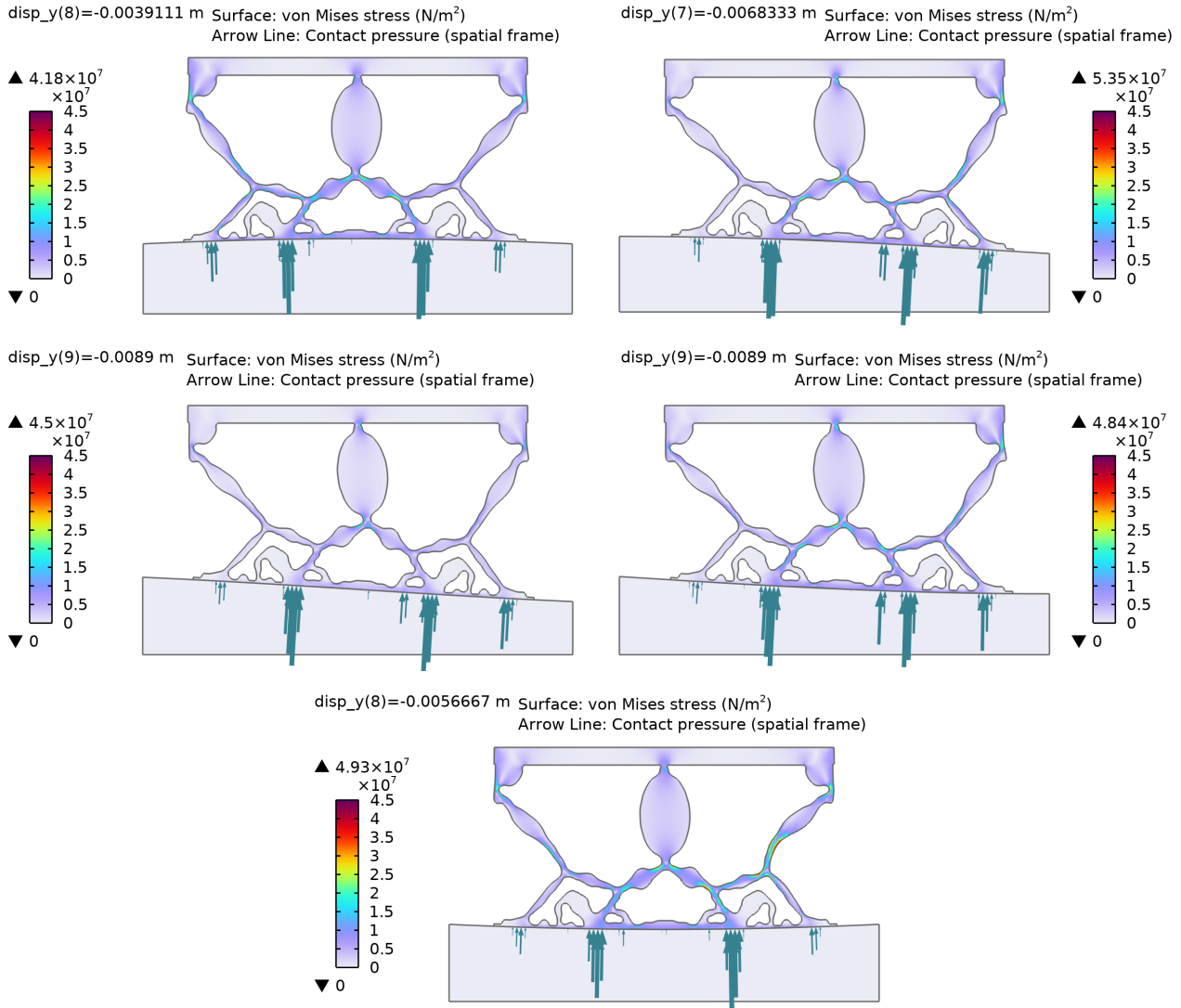


Figure D.3: Unscaled deformed configuration (from the study step closest to the maximum load) together with von Mises stress⁶ for design F_{std} at all evaluated positions above the camring for the performed contact study. The size of the blue arrows is proportional to the contact pressure. However, not the same scaling is used between different positions.

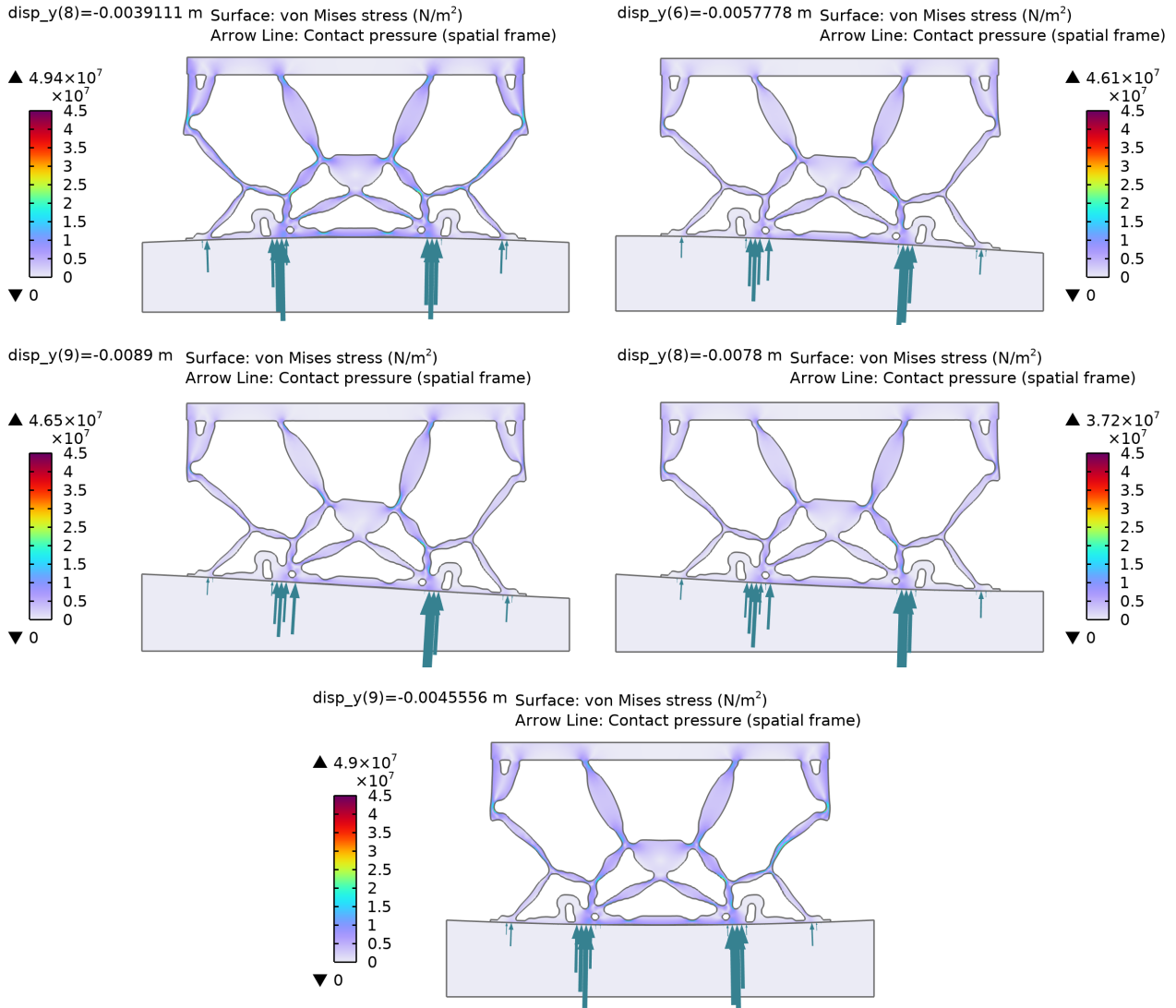


Figure D.4: Unscaled deformed configuration (from the study step closest to the maximum load) together with von Mises stress⁶ for design F_x at all evaluated positions above the camring for the performed contact study. The size of the blue arrows is proportional to the contact pressure. However, not the same scaling is used between different positions.

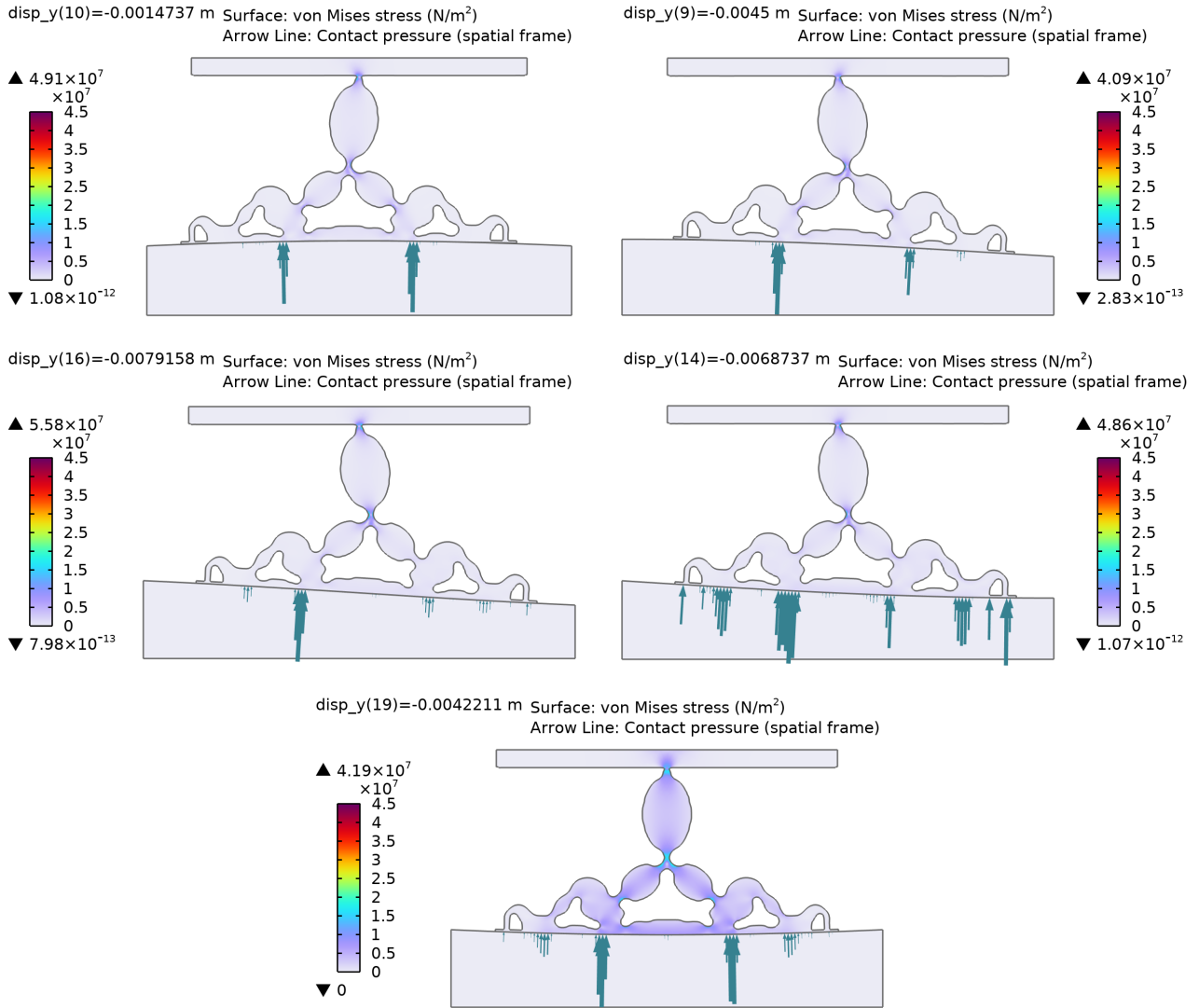


Figure D.5: Unscaled deformed configuration (from the study step closest to the maximum load) together with von Mises stress⁶ for design H_{std} at all evaluated positions above the camring for the performed contact study. The size of the blue arrows is proportional to the contact pressure. However, not the same scaling is used between different positions.

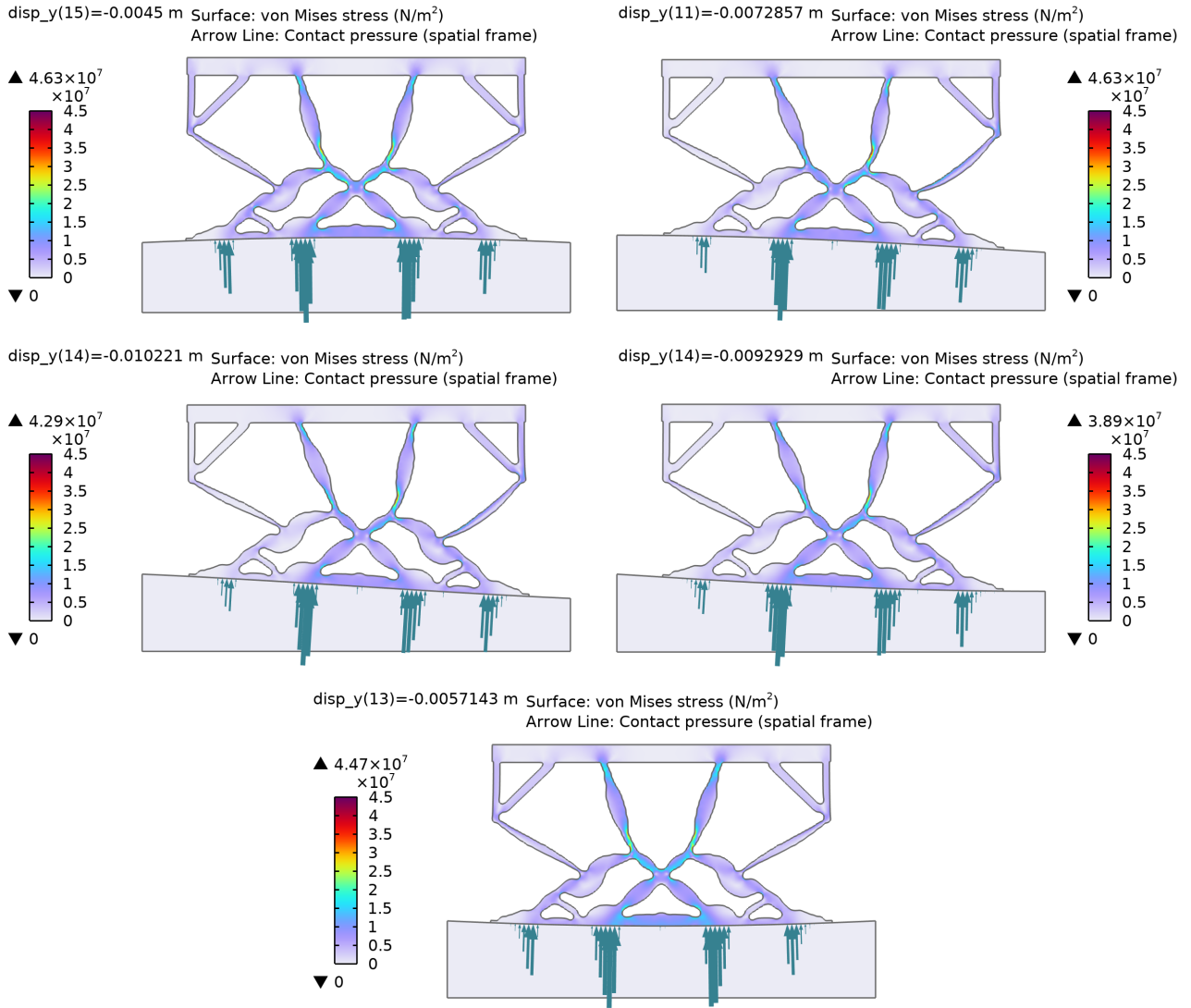


Figure D.6: Unscaled deformed configuration (from the study step closest to the maximum load) together with von Mises stress⁶ for design H_x at all evaluated positions above the camring for the performed contact study. The size of the blue arrows is proportional to the contact pressure. However, not the same scaling is used between different positions.

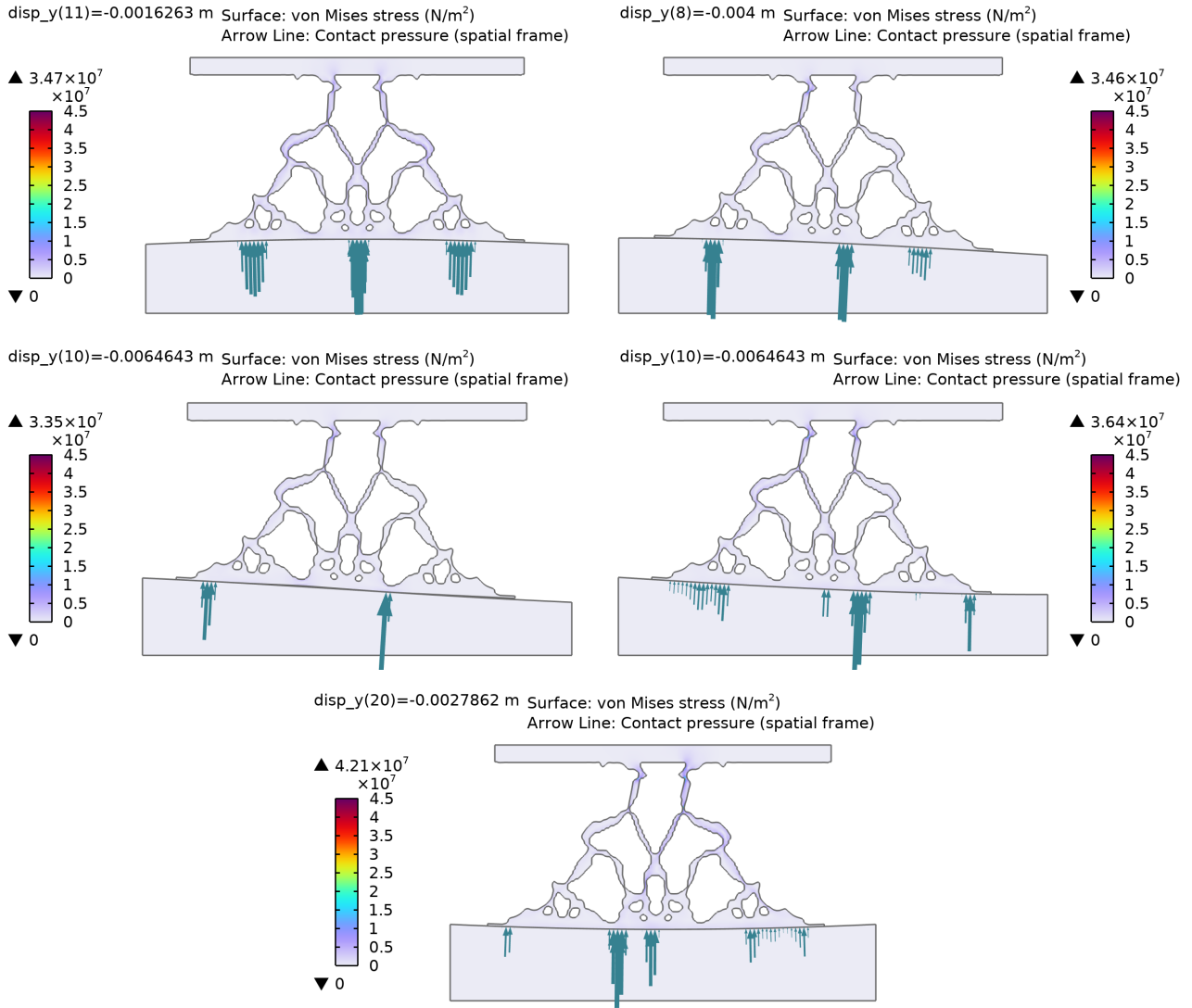


Figure D.7: Unscaled deformed configuration (from the study step closest to the maximum load) together with von Mises stress⁶ for design K at all evaluated positions above the camring for the performed contact study. The size of the blue arrows is proportional to the contact pressure. However, not the same scaling is used between different positions.

D.3. STIFFNESS PLOTS

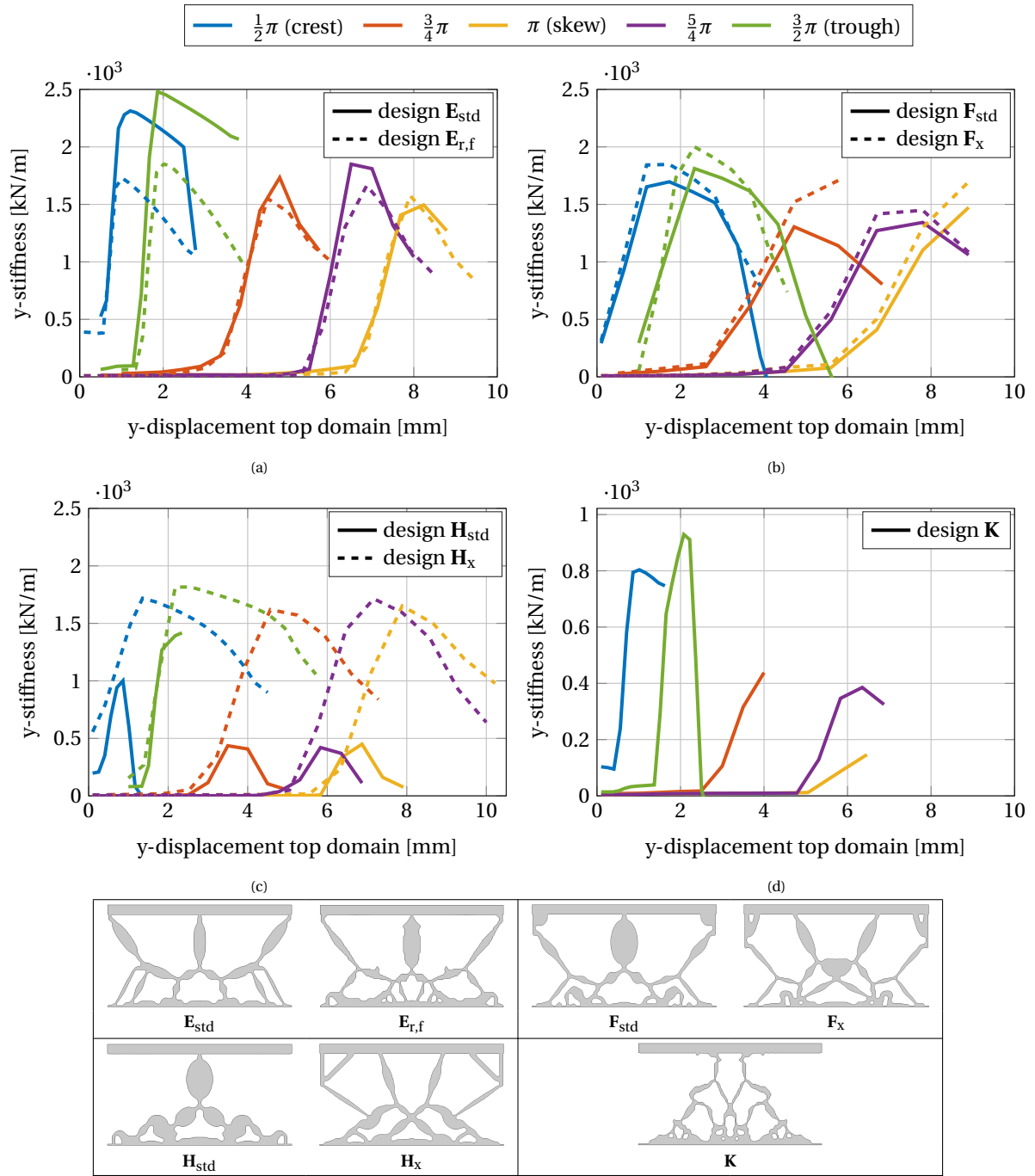


Figure D.8: y-stiffness of the structures based on the reaction force plots versus the absolute prescribed y-displacement of the top domain

D.4. LOAD AT YIELD + LOAD AT 90 % CONTACTTable D.2: Loads marked on reaction force plots [Figure 6.9](#)

Design	shift _x	load at yield [kN]	load at 90 % contact [kN]
E_{std}	$\frac{1}{2}\pi$ (crest)	4.30	0.85
	$\frac{3}{4}\pi$	2.56	0.81
	π (skew)	1.94	0.66
	$\frac{5}{4}\pi$	2.91	0.14
	$\frac{3}{2}\pi$ (trough)	4.81	0.02
E_{r,f}	$\frac{1}{2}\pi$ (crest)	2.73	1.18
	$\frac{3}{4}\pi$	2.59	1.03
	π (skew)	2.62	0.35
	$\frac{5}{4}\pi$	2.81	0.06
	$\frac{3}{2}\pi$ (trough)	3.44	0.06
F_{std}	$\frac{1}{2}\pi$ (crest)	4.94	1.01
	$\frac{3}{4}\pi$	3.14	1.38
	π (skew)	2.20	0.96
	$\frac{5}{4}\pi$	3.44	0.98
	$\frac{3}{2}\pi$ (trough)	5.52	0.03
F_x	$\frac{1}{2}\pi$ (crest)	4.76	1.06
	$\frac{3}{4}\pi$	3.36	1.58
	π (skew)	3.05	1.25
	$\frac{5}{4}\pi$	3.65	1.16
	$\frac{3}{2}\pi$ (trough)	4.95	0.03
H_{std}	$\frac{1}{2}\pi$ (crest)	0.63	n/a
	$\frac{3}{4}\pi$	0.53	n/a
	π (skew)	0.50	n/a
	$\frac{5}{4}\pi$	0.53	0.00
	$\frac{3}{2}\pi$ (trough)	3.50	0.06
H_x	$\frac{1}{2}\pi$ (crest)	5.72	2.66
	$\frac{3}{4}\pi$	4.84	3.49
	π (skew)	4.64	0.39
	$\frac{5}{4}\pi$	5.29	0.01
	$\frac{3}{2}\pi$ (trough)	6.38	0.00
K	$\frac{1}{2}\pi$ (crest)	0.73	n/a
	$\frac{3}{4}\pi$	0.18	n/a
	π (skew)	0.13	n/a
	$\frac{5}{4}\pi$	0.50	n/a
	$\frac{3}{2}\pi$ (trough)	0.72	n/a